AN OPTICAL STUDY

OF

TURBULENCE WITHIN

FIRE PLUMES

A thesis submitted for the degree of

Doctor of Philosophy

of the University of London

by

WINSTON WEN-YOUNG WONG, ARCS M.Sc., DIC

Department of Chemical Engineering
and Chemical Technology,
IMPERIAL COLLEGE,
Prince Consort Road,
London, S.W.7

Feb. 1976

DEDICATION

This thesis is dedicated to my parents,

Mr. & Mrs. Y.C. Wong.

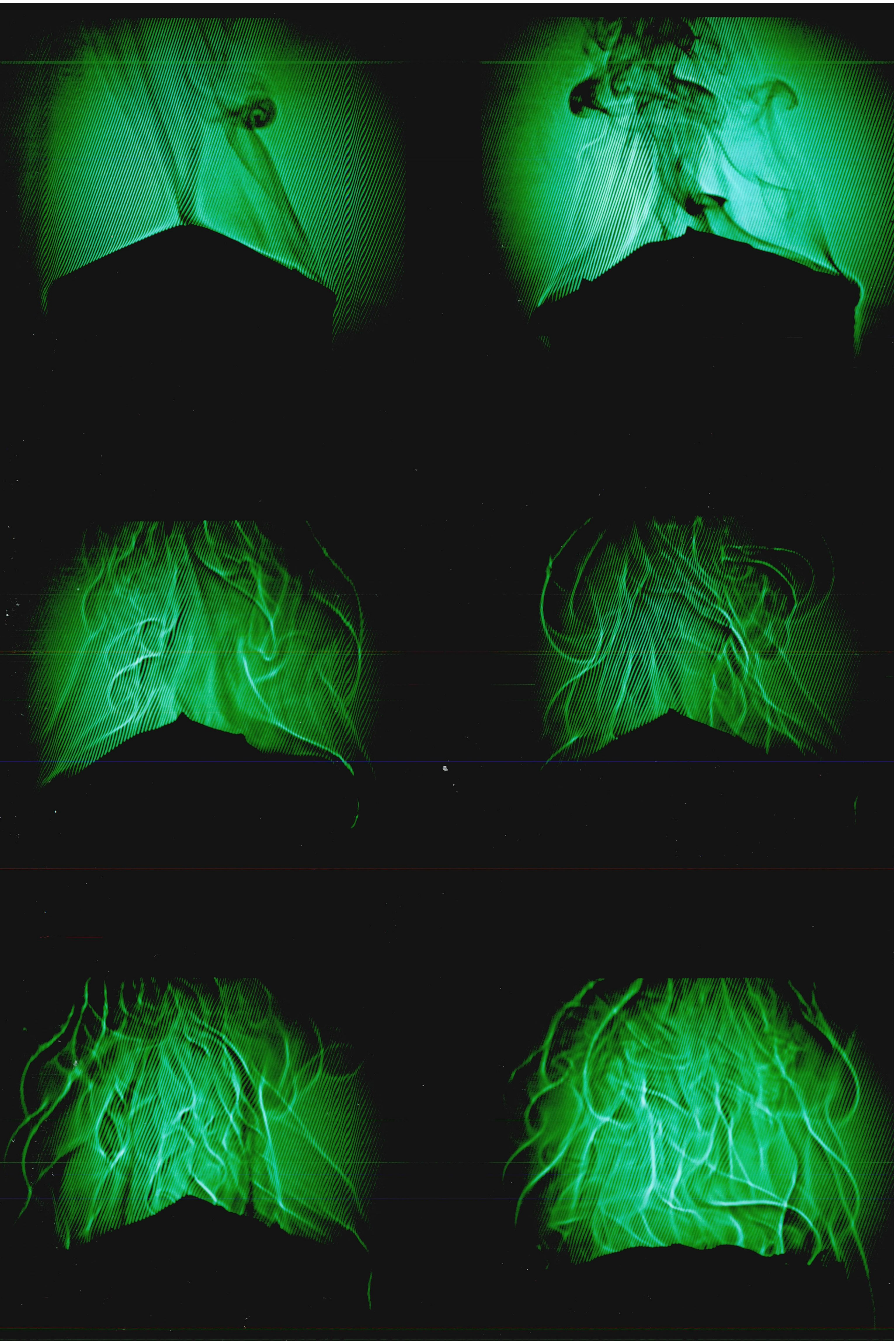

COVER PLATE

Sequential Large-Area Interferograms showing

the Combustion Process of a Model House

ABSTRACT

The initial objective of the research on fire plumes was to study the turbulence responsible for the characteristic flicker frequency for a laser-based detection device. In the course of this work, a number of new optical diagonostic techniques were developed.

A large area differental interferometer, powered by a 4-watt argon ion laser is designed to display large test areas usually encountered ib fire research (coverage of field up to 50m.in diameter can be achieved for continuous viewing). Deflection of the fringes, which is proportional to the temperature gradient can be ascertained across the entire test space by a reconstruction method using diffracted light. Using multiple exposures, this method also provides a technique fo r simultaneous mapping of velocity fields within fire plumes.

A technique using polarization measurements is devised to determine whether soot particles form elongated agglomerates in flames. This is found to occur and is important because elongation affects extinction of polarized light significantly.

A method based upon 'Doppler Velocimetry' is developed for the direct measurement of normal propagation velocities of phase objects. It is shown that this method is applicable to measuring burning velocities whether the flame is stationary, moving or fluctuating.

Using interrupted shadow interferometry and cinematography, turbulent velocity distributions and intensity of turbulence within fire plumes are measured. Results of these measurements above liquid pool fires of various sizes are presented together with the effect on them of a horizontal ceiling.

ACKNOWLEDGEMENTS

I wish to express my sincere gratitude to Professor F.J.Weinberg for introducing me to the exciting field of the optics of flames, for his constant encouragement and stimulating supervision. Thanks are also due to Dr. A.R.Jones who has shown much interest in my work and made many helpful suggestions.

I also like to thank Mr. L.Moulder for his valuable photographic contributions, and to my wife, Anita for drawing many of the diagrams and for her enduring effort in typing the maniscript.

Finally I should like to thank the Joint Fire Research Organization for financial support by way of a research bursary throughout the course of this research.

CONTENTS

CHAPTER 1

INTRODUCTION

Ever since the dawn of civilization, mankind has suffered from hazards associated with uncontrolled fires. Until the present century, almost the entire understanding and control over fire was empirical. During the past fifty years, and at an ever-increasing rate, the advancement of science, mathematical analysis and the computer have made it possible to arrive at a more quantitative understanding of the numerous (often complex) fire phenomena. Unfortunately, however, development in technology is resulting in increasing fire risks. The reason for this situation is, for example, the rapidly growing use of energy sources of all kinds and the widespread application of new materials with new and partly unknown properties (e.g. plastics of all kinds). The trend towards higher and higher value concetration in business or manufacturing areas inevitably increases the financial loss due to an outbreak of hostile fire.

It is because each developing fire must be detected in one way or another before it can be extinguished, and that the weakest link in many fire protection systems tends to be detection, that the development of an efficient fire detector, which will enable the rapid detection of fire while the fire is sufficiently small to be controlled, is of paramount importance. Various systems of lase beam fire detectors (1,2) seem to have very promising prospect. If such detectors are to be practical, then they must discriminate reliable (within an acceptable risk) between the presence and the absence of a fire (3). During 1968, JFRO carried out a survey of false alarms from fire detection systems (4) which indicated that the ratio of false alarms to fires was greater than 10 : 1.

The initial objective of the present research was to study flow and turbulence in fire plumes in order particularly to characteries the flicker frequency by which laser-based detection devices distinguish between causes of random fluctuations and fires. Such devices utilize the schlieren effect due to the passage of interfaces separating hot and cold gas and this defines the relationship between flicker and the size, frequency, and convective velocity of turbulence eddies.

The main advances described in this thesis are concerned with improvements in instrumentation and with the development of new diagnostic techniques involving turbulence, velocity and temperature measurements.

An 'interrupted shadow interferometric' technique was developed and was shown to be capable of fullfiling the original aim of measuring flicker frequency as well as yielding information concerning the variation with height of average turbule velocities and turbulence intensities within fire plumes.

The change in intensity as a laser beam passes through fire plumes containing particulates was investigated as this might affect the performance of a laser-fire detector. An optical technique was devised to measure the extinction of a laser beam as a function of polarisation in a flame with a distinct flow gradient. The results indicate that soot particles do form elongated agglomerates in flames.

Another advance in optical instrumentation that is described was the design and performance of a 'Doppler Velocimeter' which is capable of measuring orthogonal velocity components directly when each part of a moving phase object, such as a flame, is displayed as an equi-spaced fringe pattern parallel to its local refractive index contours. A schlieren system with a special aperture which produces this type of interference is devised for the purpose. When the reactants are in flow, in the case of a flame, direct measurement of burning velocities is made possible by allowing the interference pattern due to a small particle to interact with that of the front. The method is thus applicable whether the flame (or other propagating front) is stationery, moving or fluctuating. It was shown that this method is also suitable to the study of turbulent flows. The method has been tested on moving diffraction gratings, particles and flames stabilized on a burner and propagating in a tube.

The main distinction between fire research and other branches of combustion in which the study of refractive index fields has proved so useful (e.g. see ref. 5 to 7) is the large area of the test space involved, which cannot be scaled down without modifying the phenomena under study. The difficulty does not lie in the power required to transluminate large working space - a 4 W argon ion laser allows coverage of a field 50 m. in diameter at exposure times of the order of 10^{-2} second, given a large enough screen. What is absolutely limiting, however, is the maximum available size of optical components such as lenses and mirrors, which effectively makes it impossible to focus the transluminating beam between the test object and the first receptor.

A new method has been developed to measure temperature distributions around two-dimensional test objects (e.g. walls exposed to radiation from fires) using a large area interferometer (see Chapter 3). The fundamental difficulty is associated with the size of the test space. In order to obtain a focused image at a sufficiently short exposure time, a camera has to be used to photograph a pattern on the screen. Now a wide fringe spacing, which would give the appearance of a normal interferogram on the final image, would not resolve fine detail in the test space, whereas the fine fringes required to reveal such detail would not be resolved on the final record. The method developed uses the principle of reconstructing a double exposure hologram - or a Moiré pattern between interferograms in the presence and absence of the test space. It differs from conventional holography in that the "reference beam" also traverses the test space and is only infinitesimally separated from the "test beam". In this manner, fringes of iso-deflection contours can be obtained over enormous areas and with unprecedented sensitivity. As regards the latter, it has been calculated that a temperature gradient of 5×10^{-3} degree C per cm. would give rise to one complete fringe for an object 1 m in length by photographing primary fringes on a screen of spacing such that they would just be resolved in the image, using an emulsion capable of separating 6000 lines per mm..

CHAPTER 2

DIRECT OPTICAL EVIDENCE FOR THE PRESENCE OF SOOTY AGGLOMERATES IN FLAMES

2.1 Introduction

A laser beam on passing through fire plumes containing particulates will suffer reduction in intensity due to absorption and scattering. This loss is a function of the shape, size and concentration of the particles. As a laser beam passes through the soot zone of a luminous flame , scattering is negligible, since such particles are absorbing and very small compared to the wavelength.

It is possible that the soot particles are non-spherical, either individually or as a result of agglomeration. In fact, electron micrographs of soot samples collected from flames often indicate agglomerated soot particles, but it is not possible to determine to what extent this is due to the sampling process. Evidence that elongated particles are actually present in flames was provided by Dalzell, Williams and Hottel (8) using light scattering methods, but their analysis was based on Rayleigh - Debye theory which is not strictly applicable to soot.

Jones (9) estimated the possible effects of particle agglomeration on the emissivity of sooty flames, and has concluded that chain formation may significantly increase absorptivity for the same quantity of soot.

The amount of light collected at a laser fire detector may therefore vary significantly as to whether soot particles are agglomerated in flames. In this chaper, an optical method is described, which provides direct optical evidence that soot particles do form agglomerates in flames.

Cerf and Scheraga (10) have shown that elongated particles are not necessarily randomly aligned in a moving fluid. In particular, for particles with a maximum dimension not greater than 1 μm in a shear flow the torque due to the gradient in drag force would be compensated by Brownian motion collisions. The particles then have a tendency to be aligned in the flow.

The optical properties of such a system would be a function of polarization. This effect has been observed in a number of situations and is known as streaming birefringence (11). Emission from such a cloud of particles would also be partially polarized.

Extinction measurements for a 'slot' burner are presented and the technique of measuring the extinction of a laser beam as a function of polarization in a flame with distinct flow gradient is described. These experiments show that the intensity of a laser beam will be greatly reduced due to absorption by any soot particles and that the measured intensity at the fire detector may depend upon the polarizational state of the laser employed in the presence of soot particles.

2.2 Extinction by Particles

This section discusses the phenomenon of light extinction by particles. In particular, it will be seen that in comparion with spherical particles of equal volume, the extinction is significantly greater for elongated particles.

2.2a Basic Concepts

The scattered intensity at a point (r, θ, ϕ) may be written in the form (12)

$$I_{sca} = I_o / k^2 r^2 \, F(\theta, \phi) \qquad 2.2a.1$$

$F(\theta, \phi)$ is the dimensionless scattering function, which depends on direction but not distance. It also depends on the orientation of the particle with respect to the incident wave, the particle size parameter $(x = 2\pi a/\lambda)$, the refractive index and on the state of polarization of the incident wave. If a detector subtends a solid angle $d\Omega$ at the particle, the total power scattered over a sphere of radius r is

$$P_{sca} = (I_o/k^2) \int_{4\pi} F(\theta, \phi) \, d\Omega \qquad 2.2a.2$$

The scattering cross-section C_{sca} is defined as

$$C_{sca} = P_{sca}/I_o = (1/k^2) \int_{4\pi} F(\theta, \phi) \, d\Omega \qquad 2.2a.3$$

A cross-section for absorption C_{abs} may be defined similarly. The extinction cross-section is given by

$$C_{ext} = C_{sca} + C_{abs} \qquad 2.2a.4$$

The scattering and absorption efficiency factors are defined as

$$Q_{sca} = P_{sca}/P_{inc} = C_{sca}/A \qquad 2.2a.5$$

$$Q_{abs} = P_{abs}/P_{inc} = C_{abs}/A \qquad 2.2a.6$$

Where A is the cross-sectional area of the scatterer.

For particles where $x = 2\pi a/\lambda \lesssim 25$, wave optics must be used. The solution for spheres is given by G.Mie (13) For large particles geometrical optics may be used though diffraction has to be included. For very small particles ($x << 1$), and our primary concern is soot particles, Rayleigh theory is appropriate. The results are $Q_{sca} \propto x^4$; $Q_{abs} \propto x$ (14). It follows that if $C_{abs} \neq 0$, $C_{abs} >> C_{sca}$. Therefore in transmission through a cloud of soot particles, the extinction:

$$E = 1 - \exp(-K_e L) \qquad 2.2.a7$$

may be written as :

$$E = 1 - \exp(-K_{abs} L) = \alpha_\lambda = \varepsilon_\lambda \qquad 2.2a.8$$

The absorption coefficient K_{abs} is given by :

$$K_{abs} = \int_\xi N(\xi)\, C_{abs}(\xi)\, d\xi \qquad 2.2a.9$$

There being $N(\xi)\, d\xi$ particles per unit volume for variation of the parameter ξ between ξ and $\xi + d\xi$.

2.2b <u>Effects of Agglomeration</u>

Separate soot particles may agglomerate into a larger spherial-like particle or coalesce into an elongated particle. A test of the difference due to elongation is to compare K_{abs} due to spheres and elongated particles. A simple shape which may be applied to elongated particles is the prolate spheroid, for which the scattering theory is known in Rayleigh's approximation (11).

The absorption corss-section for randomly oriented prolate spheroids is:

$$C_{abs} = (-2\pi V/3\lambda)\ \mathrm{Im}\{ (m^2-1)\left(\frac{1}{L_1(m^2-1)+1} + \frac{2}{L_2(m^2-1)+1}\right) \}$$

2.2b.1

where :

$$L_1 = (1-e^2)/e^2 \ \{ (1/2e) \ln (1+e/1-e) - 1 \}$$

2.2b.2

$$L_2 = (1-L_1) / 2 \qquad 2.2b.3$$

Taking constant wavelength and refractive index equation 2.2a.9 may be written :

$$K_{abs} = N \iint_{Ve} C_{abs}(V,e)P_1(V)P_2(e)dVde \qquad 2.2b.4$$

where P(x) is the normalized distribution function of x. Since from 2.2b.1 we may write C_{abs} in the form:

$$C_{abs} = V\ f(e) \qquad 2.2b.5$$

K_{abs} may be written:

$$K_{abs} = N \int_V VP_1(V)dV \int_e f(e)P_2(e)de \qquad 2.2b.6$$

or

$$K_{abs} = N\bar{V} \int_e f(e)P_2(e)de \qquad 2.2b.7$$

In the case of spherical particles, the absorption coefficient is :

$$K_{abs}(\text{spheres}) = N\bar{V}\ \{ -(6\pi/\lambda)\ \text{Im}\ (m^2-1/m^2+2) \}$$
$$= N\bar{V}\ f(0) \qquad 2.2b.8$$

$N\bar{V}$ must be a constant since it is just the total volume of all the particles in the system. Therefore, if separate spheres coalesced into a larger sphere K_{abs} would be unchanged. The effect of elongation may be written :

$$\bar{R} = \frac{K_{abs}(\text{prolate spheroids})}{K_{abs}(\text{spheres})} = (1/f(0)) \int_e f(e)P(e)de$$

$$= \int_e R(e)P(e)de \qquad 2.2b.9$$

where

$$R(e) = f(e) \; / \; f(0) \qquad 2.2b.10$$

Jones (9) has done some calculations based on the data of Medalia and Heckman (14). His result is shown in Figure 2.1, which is a plot of ln(R-1) against ln E (E = Anisometry -1) for various refractive indices within the range $E \lesssim 3$. Doubling the elongation would increase R-1 by a factor of three to four. Therefore, agglomeration into chains will increase emissivity for the same quantity of soot. If also follows that light attenuation will be greater in the presence of chain-agglomerates.

2.3 Passage of Polarized Light Through Particulate Clouds

In this section we shall outline the basic theoretical and physical concepts behind the design of our optical experiment to determine whether sooty agglomerates are present in flames. It will be shown that the intensity of the emergent beam through a system of particles will be different for linearly horizontally and vertically polarized particles which are partially aligned.

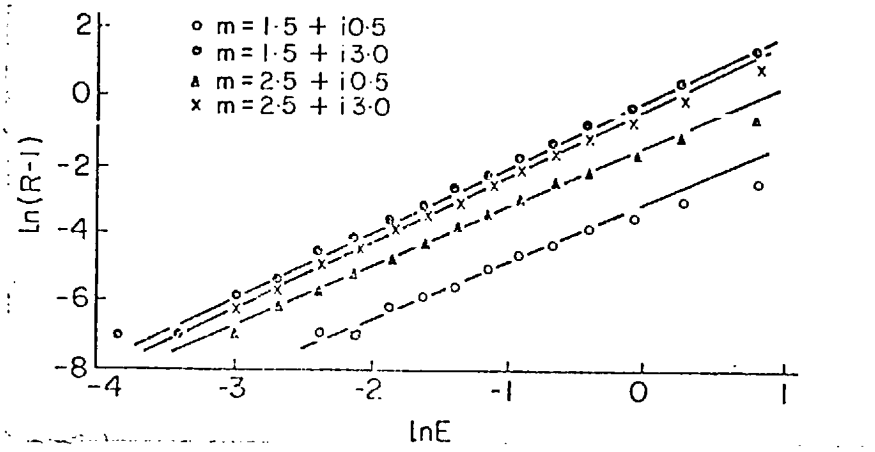

Figure 2.1 Increase in absorption against elongation

2.3a Stokes Representation of States of Polarization

Consider an electromagnetic wave propagating along the z-axis with the $\underline{E}$ and $\underline{H}$ vectors vibrating harmonically in the xy-plane. Because $\underline{E}$ and $\underline{H}$ are perpendicular to each other, it is only necessary to discuss the behaviour of $\underline{E}$ which will define the direction of polarization. When there is no attenuation in the medium, the two Cartesian components are given by:

$$E_x = a_x \exp\{\ i(\omega t - kz + \delta_1)\ \}$$
$$E_y = a_y \exp\{\ i(\omega t - kz + \delta_2)\ \} \qquad 2.3a.1$$

For natural light, the phase angles δ_1 and δ_2 vary randomly with respect to each other but for polarized light (e.g. laser light), the phase difference $\delta = \delta_2 - \delta_1$ is fixed.

The Stokes representation of states of polarization (Stokes Vector) consists of a set of four quantities that describe the intensity and polarization of a beam of light (15).

The four parameters have the dimensions of intensity, they comprise a column vector :

$$\begin{bmatrix} I \\ M \\ C \\ S \end{bmatrix} = \begin{bmatrix} \langle a_x^2 + a_y^2 \rangle \\ \langle a_x^2 - a_y^2 \rangle \\ \langle 2a_x a_y \cos\delta \rangle \\ \langle 2a_x a_y \sin\delta \rangle \end{bmatrix} \qquad 2.3a,2$$

For a light beam with horizontal linear polarization, equation 2.3a.2 reduces to :

$$\begin{bmatrix} I \\ M \\ C \\ S \end{bmatrix} = \begin{bmatrix} 1 \\ 1 \\ 0 \\ 0 \end{bmatrix} \qquad 2.3a.3$$

The corresponding Stokes vector for a vertically linear polarized light is :

$$\begin{bmatrix} I \\ M \\ C \\ S \end{bmatrix} = \begin{bmatrix} 1 \\ -1 \\ 0 \\ 0 \end{bmatrix} \qquad 2.3a.4$$

The essential property of the Stokes parameter is their additivity in the superposition of two independent beams of light. Thus additivity corresponds to the absence of any interference.

When a beam of light passes through some optical arrangement, the intensity and the state of polarization of the incident beam. If two independent incident beams are superposed the new emergent beam will be, if the process is linear, the superposition without interference of the two emergent beams corresponding to the separate incident beams (this is so in our case since light scattered from clouds of particles randomly aligned are incoherent). Consequently, in such a linear process, from the additivity properties of the Stokes' parameters, the parameters I', M', C', S' which define the polarization of the emergent beam must be homogeneous linear functions of the parameters I,M, C,S corresponding to the incident beam; the sixteen coefficients of these linear functions will completely characterize the corresponding optical phenomenon. Therefore, we may write:

$$\begin{bmatrix} I' \\ M' \\ C' \\ S' \end{bmatrix} \quad \begin{bmatrix} m_{11} & m_{12} & m_{13} & m_{14} \\ m_{21} & m_{22} & m_{23} & m_{24} \\ m_{31} & m_{32} & m_{33} & m_{34} \\ m_{41} & m_{42} & m_{43} & m_{44} \end{bmatrix} \quad \begin{bmatrix} I \\ M \\ C \\ S \end{bmatrix} \qquad 2.3a.5$$

2.3b <u>The Case of Incident Beams With Linear Polarization in Horizontal and Vertical Directions</u>

For the purpose of our experiment, we are interested in incident beams with linear polarization either horizontal or vertical. Under these conditions only the four coefficients m_{11}, m_{12}, m_{21} and m_{22} are involved. Therefore for horizontally polarized incident light, equation 2.3a.5 reduces to:

$$\begin{bmatrix} I'_h \\ M'_h \end{bmatrix} = \begin{bmatrix} m_{11} & m_{12} \\ m_{21} & m_{22} \end{bmatrix} \begin{bmatrix} 1 \\ 1 \end{bmatrix} = \begin{bmatrix} m_{11}+m_{12} \\ m_{21}+m_{22} \end{bmatrix} \qquad 2.3b.1$$

Similarly, for vertically polarized light we have:

$$\begin{bmatrix} I'_v \\ M'_v \end{bmatrix} = \begin{bmatrix} m_{11}-m_{12} \\ m_{21}-m_{22} \end{bmatrix} \qquad 2.3b.2$$

Here the subscripts h and v stands for incident light linearly polarized in horizontal and vertical directions respectively.

2.3c Intensity of Scattered Light

In section 2.2a, it was pointed out that when a beam of light passes through a cloud of particles, the extinction is in general due to both absorption and scattering. Here we shall discuss the effects of particle shape and orientation on the intensity of scattered light.

Using a general law of reciprocity due to Lord Rayleigh (16), Krishnan (17) has shown that in general, for a system consisting of a large number of particles, irrespective of their size, shape and structure, randomly oriented in space:

$$m_{12,s} = m_{21,s} \qquad 2.3c.1$$

(the subscript s is used for the case of scattering)
In particular, for spherical scattering particles of any dimension:

$$m_{12,s} = m_{21,s} = 0 \qquad 2.3c.2$$

Therefore, from equations 2.3b.1 and 2.3b.2 it follows that when incident beams of equal intensity but with different states of polarization (linearly horizontal and vertical) interact with a cloud of spherical particles (irrespective of their sizes), the intensities of the scattered beams I'_{hs} and I'_{vs} are equal.

In the case of elongated particles, however, Krishnan (18) has demonstrated that :

$$m_{12,s} = m_{21,s} \neq 0 \qquad 2.3c.3$$

and that the optical anisotropy increases with the degree of orientation of the elongated particles, hence a correspondingly greater value of these coefficients.

2.3d Basic Considerations of the Experiment

The transmitted power, P_{trans}, may be written :

$$P_{trans} = P_{inc} - P_{abs} - P_{sca} \qquad 2.3d.1$$

When the incident beams described by $\begin{bmatrix}1\\1\end{bmatrix}$ and $\begin{bmatrix}1\\-1\end{bmatrix}$ pass through particulate clouds, from the previous discussions, the implications are :

1. The intensity of the beams will be reduced.
2. The extinction is greater the longer the path length (2.2a.7), hence a long 'slot' burner is used for extinction measurements.
3. If the cloud consists only of spherical particles, the transmitted powers of both incident beams will be the same.
4. For randomly aligned elongated particles, P_{sca}, is independent of polarization.
5. When the elongated particles are aligned, then both P_{abs} and P_{sca} will differ.

As indicated earlier (section 2.2a) soot particles are absorbing and very small compared to the wavelength so that absorption predominates. Therefore, in order to detect any differential in the transmitted powers, an arrangement is required to align the soot particles.

Cerf and Scheraga (10) have shown that non-spherical or anisometric particles and molecules will be partially oriented if they are in a flow system or if they are subject to electric or magnetic fields. The production of birefringence in this manner is referred to as the Kerr effect, the Cotton-Mouton effect, or the Maxwell effect, depending upon whether the applied field is electric, magnetic, or hydrodynamic, respectively.

Figure 2.2 illustrates the Maxwell effect, where the torque produced by the velocity gradient is exerted on a rod. The effect of the torque is to make the rod rotate. This torque will be opposed by the Brownian motion collisions and the degree of orientation will be proportional to the velocity gradient.

2.4 Experimental Procedures

The experiment was divided into two parts. In part 1, a long slot burner was used for extinction measurements. The objective of part 2 was to determine whether sooty agglomerates exist in flames.

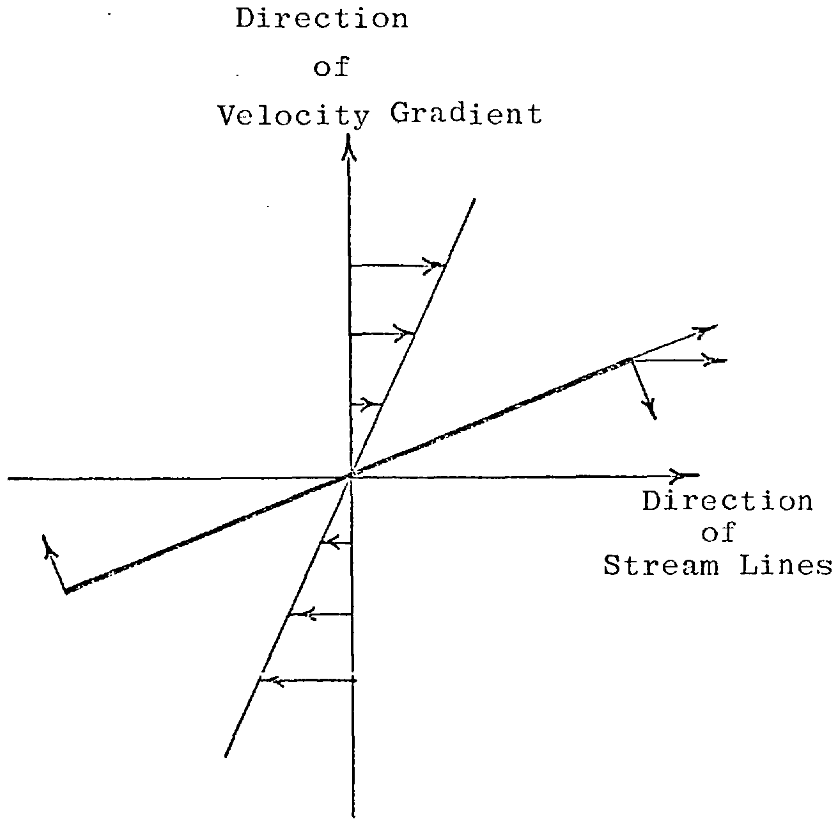

Figure 2.2. Illustration of the Maxwell effect

2.4a Extinction Measurements

The experimental setup is as shown in Figure 2.3. A Scientifica and Cook Electronics B 18/3 8 m W dc uniphase helium-neon gas laser was used. The laser beam was chopped at 12 Hz., and a reference signal was provided by an independent light source (a quartz-iodine lamp) and photocell at the chopper. This signal together with the output from the photomultiplier was fed into a phase sensitive detector (PSD). The output from the PSD in turn was displayed on an oscilloscope or chart recorder.

The photomultiplier was calibrated using a set of neutral density filters with transmittances varying between 0.29 and 0.72. It was established that:

$$T_{corr} = 0.69\ T_{rec} + 0.31 \qquad 2.4a.1$$

where T_{corr} and T_{rec} were the true and recorded transmittances respectively.

The burner was a 10 cm. slot in a quartz tube. With the help of rasching rings a uniform flame was obtained along the slot. The fuel used was propane.

For a given flow rate, the concentration of soot particles varies with position in the flame. The height in the flame was varied directly by mounting the burner on a lab jack.

In order to reduce the background from the flame, a Kodak Wratten filter No.72B was mounted in front of the

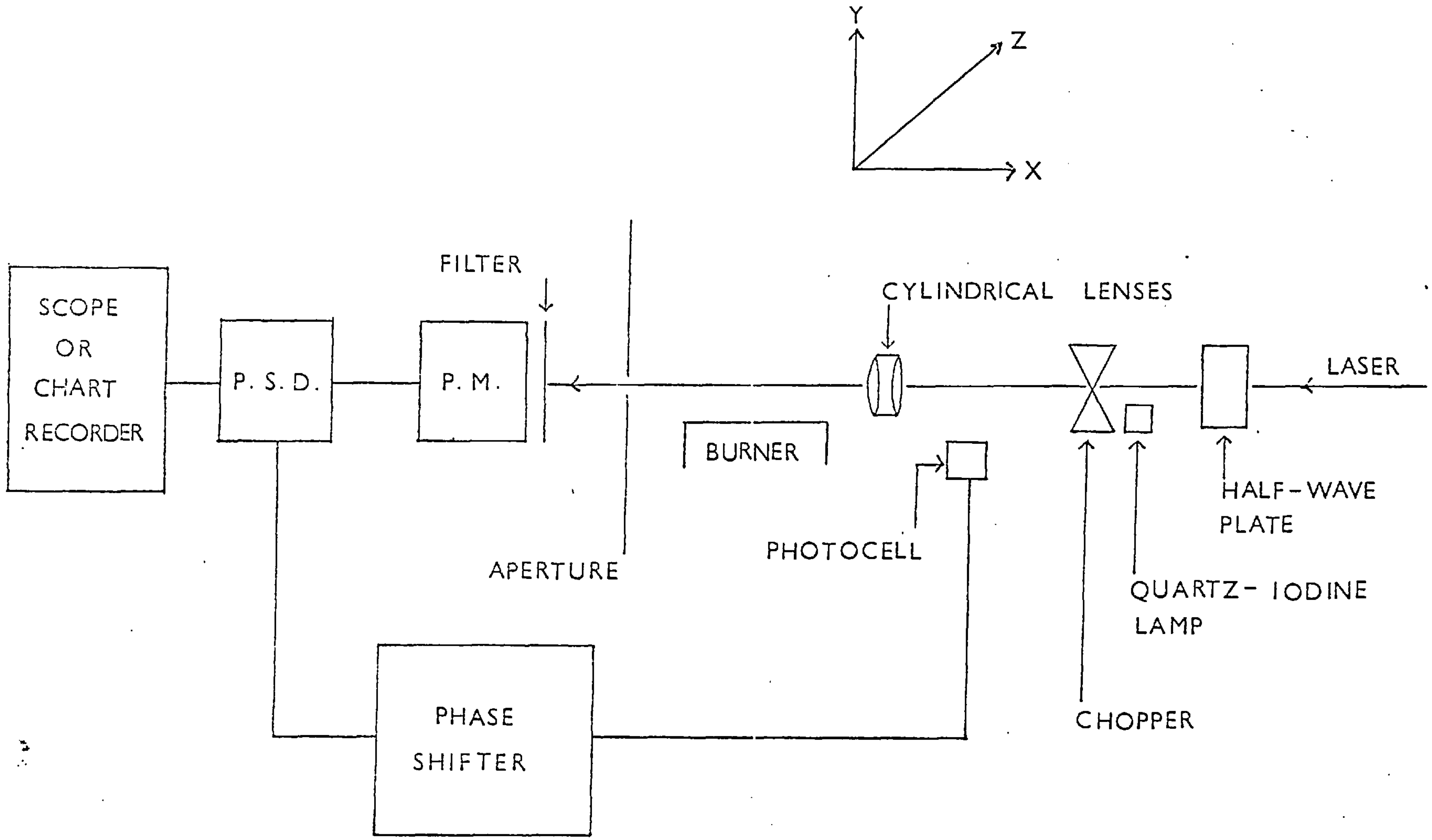

Figure 2.3 The experimental setup for extinction measurements

photomultiplier.

The flame was easily perturbed by draughts in the laboratory. Therefore, an enclosure with chimney was built around the burner which stabilized the flame considerably,

Due to schlieren effects the laser beam oscillates about the z-axis (Figure 2.3) when the flame is perturbed by ambient conditions. This is akin to the principle used for detection but here it is a problem because it would lead to greater changes in received intensity than those due to extinction. An arrangement such that when the beam passed straight through the flame a minimum was recorded, was found to be satisfactory to counter this effect except that an absolute minimum was difficult to establish. Therefore, sets of readings were taken and the mean extinction calculated. A considerable improvement in accuracy was obtained when the laser beam was first expanded by a set of cylindrical lenses into a narrow line along the z-direction. The effective focal length of the lenses was just wide enough to encompass sideways fluctuations of the flame. The slit in front of the photomultiplier was as wide as the beam, which was sufficient for any deflections due to schlieren effects to be included in the total light collected.

A further difficulty was encountered due to variations in the laser intensity. Two approaches were taken to counter this problem. Firstly, a set of readings were taken with the flame off before and after readings were taken with the flame on. This procedure was repeated for different beam heights. The second method was to use a beam splitter and monitor the reflected beam separately.

The propane flow rate was varied between 3.00 and 4.20 ml s^{-1}. At each fuel flow rate extinction measurements were made for several flame heights. The result is shown in Figure 2.4. Two conclusions may be drawn:

1. For a given flow rate, there is one burner height at which the extinction is a maximum.
2. The height of the burner at which maximum extinction occurs increases approximately linearly with the fuel flow rate (Figure 2.5).

2.4b <u>Polarizational Measurements</u>

The experimental setup was essentially the same as that depicted in Figure 2.3. The light from the laser was plane polarized along the y-direction. The direction of polarization was varied between P=0 (original state of polarization) and P=90 by means of a half-wave plate.

A flow gradient was achieved by the use of a Wolfhard-Parker burner (Figure 2.6) in which air passed through one side at a flow rate of 0.48 ls^{-1} while the rate of fuel flow through the other side was varied.

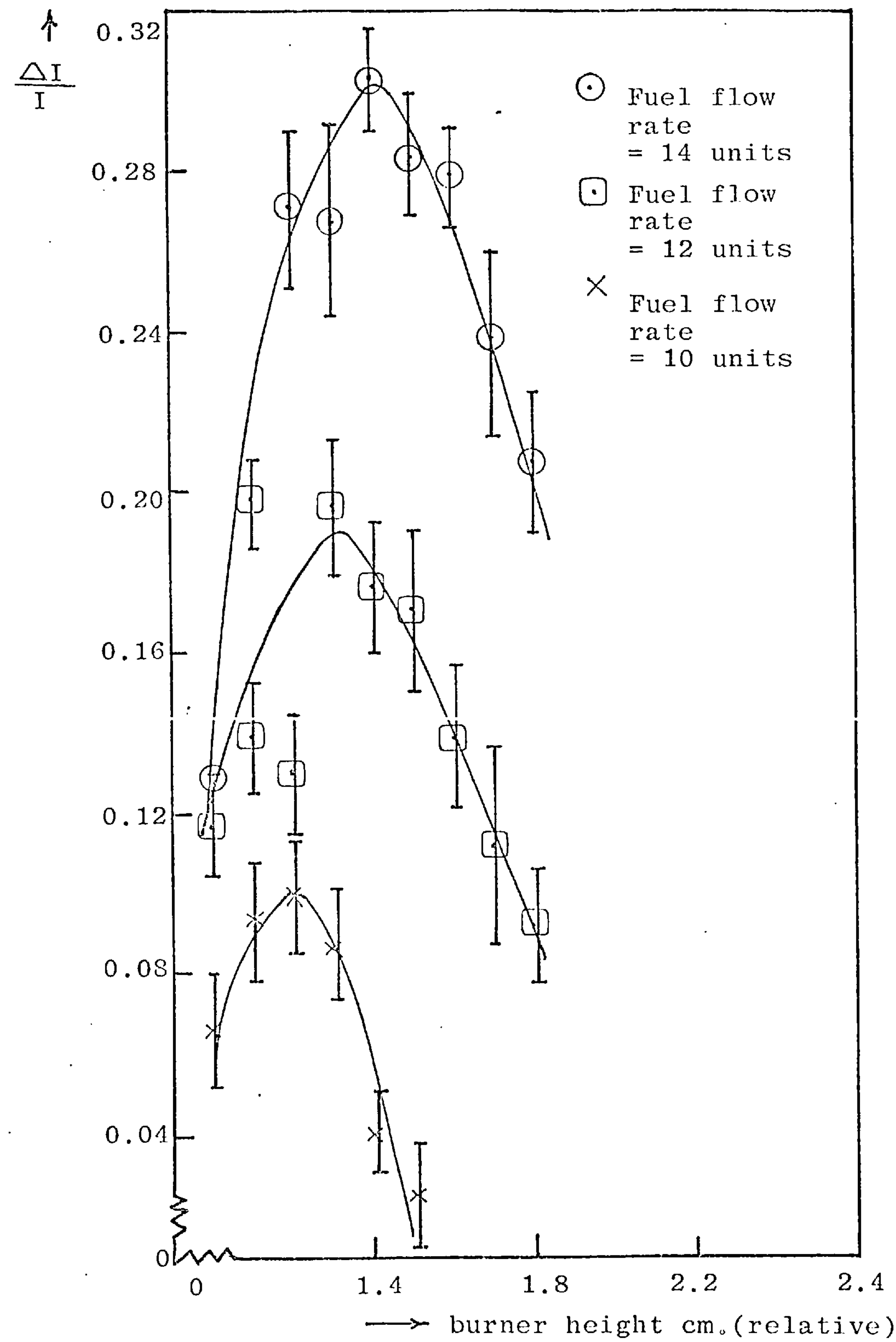

Figure 2.4 Plot of $\frac{\Delta I}{I}$ versus height from burner

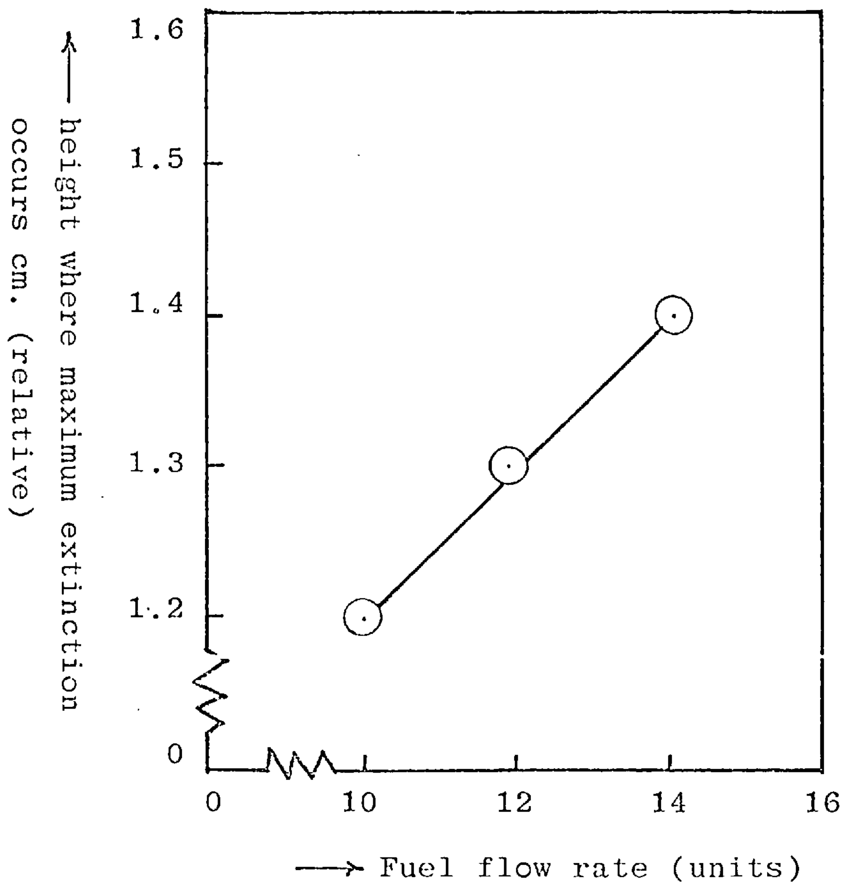

Figure 2.5 Variation of height where maximum extinction occurs with fuel flow rate

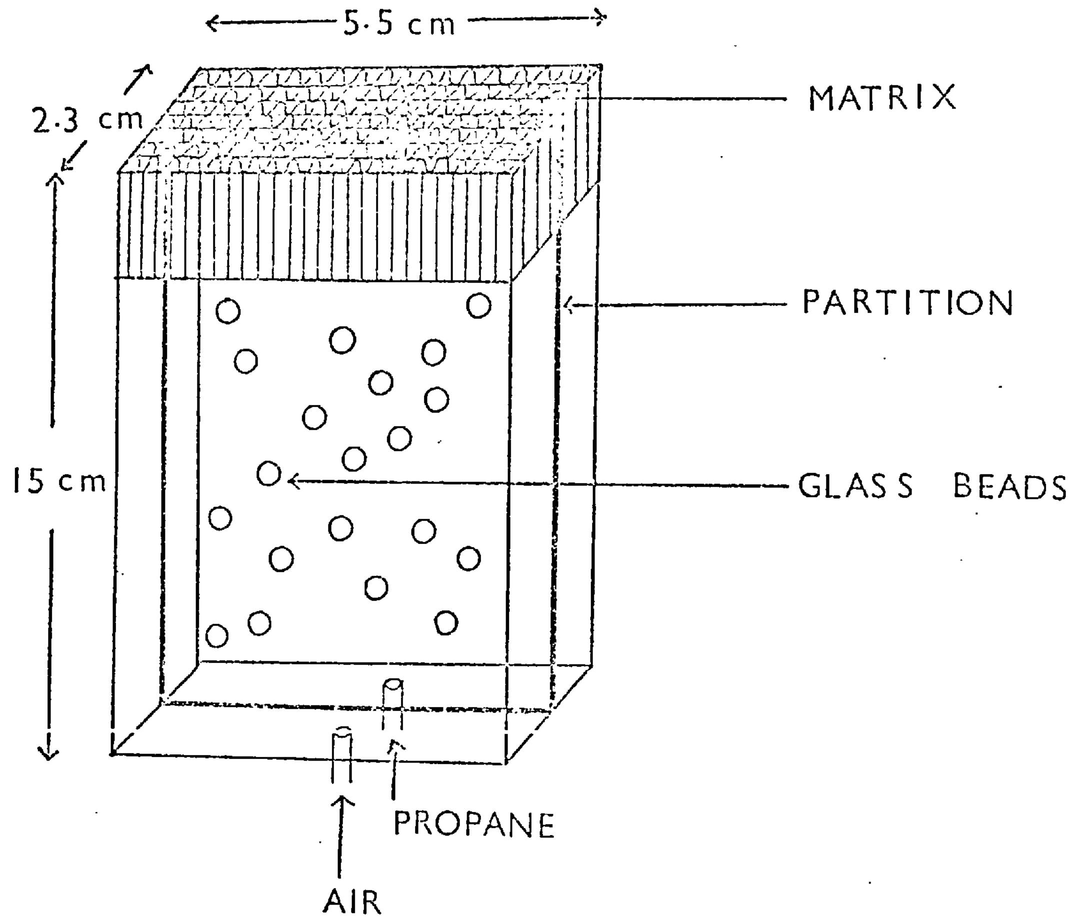

Figure 2.6 Wolfhard-Parker burner

The fuel used throughout these experiments was propane

The propane flow rate was varied between 1.85 and 5.15 ml s^{-1}. At each fuel flow rate extinction measurements were made for both polarizational states P=0 and P=90. These sets of experiments were repeated several times. Finally soot samples were taken for the fuel flow rates of 1.85, 3.00 and 5.15 ml s^{-1}. They were obtained by passing an electron microscope grid attached to a microscope slide through the flame at the same height as the laser beam. The samples were then photographed by electron microscope. Typical pictures are shown in Figures 2.7 , 2.8 and 2.9.

We define :

$$r = \left(\frac{I_{trans,o}}{I_{ref,o}} \right) / \left(\frac{I_{trans,90}}{I_{ref,90}} \right) \qquad 2.4b.1$$

where $I_{trans,o}$ and $I_{trans,90}$ are the transmitted intensities at polarization P=0 and 90 respectively. $I_{ref,0}$ and $I_{ref,90}$ are the reference intensities (i.e. in the absence of a flame). Therefore, if there is no birefringence r=1.

The main experimental results are presented in Figure 2.10, which shows a relationship between r and fuel flow rate.

The validity of the results was checked by repeating the experiment using a glass plate and a neutral density filter of comparable extinction to the

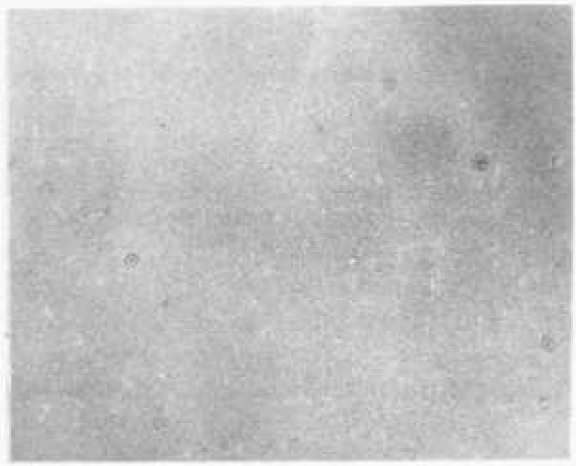

Figure 2.7 Electron micrograph of soot particles collected from flame.

Magnification X 100,000
Air flow rate = 480 ml s^{-1}
Fuel flow rate = 1.85 ml s^{-1}

Figure 2.8 Electron micrograph of soot particles collected from flame.

Magnification X 100,000
Air flow rate = 480 ml s^{-1}
Fuel flow rate = 3.00 ml s^{-1}

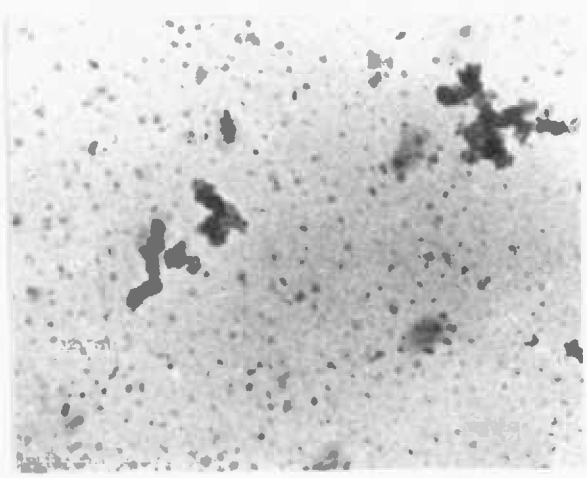

Figure 2.9 Electron micrograph of soot particles collected from flame.

Magification X 100,000
Air flow rate = 480 ml s^{-1}
Fuel flow rate = 5.15 ml s^{-1}

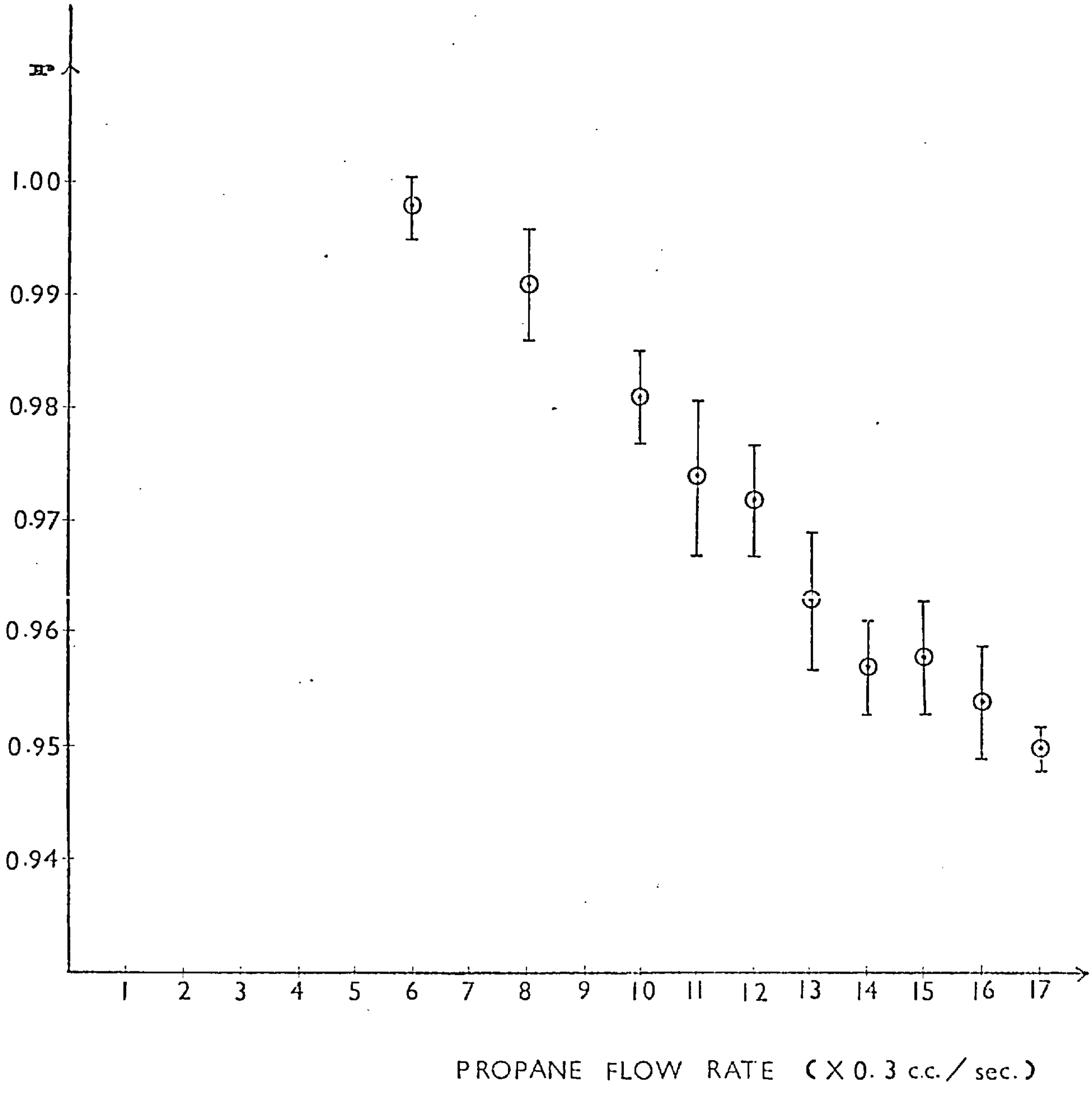

Figure 2.10 Plot of r versus fuel flow rate

flame. For a glass plate of 91% transmission the value of r was 0.995 ± 0.005 and for a neutral density filter of 80% transmission r=1.008 ± 0.005.

2.5 Conclusions

Theoretically, it has been shown that light absorption due to a cloud of particles will be significantly greater in the presence of agglomeration. The pictures shown in Figures 2.7, 2.8 and 2.9 are not exact representations of the soot structures in the flame. Nevertheless, they correlate with the experimental results shown in Figure 2.10. Figure 2.7 shows the soot particles as small virtually monodispersed spheres and the value of r is unity. As the fuel flow rate is increased and more soot formation takes place the particle size increases and more structure is seen. At the highest flow rate used we see in Figure 2.9 that much of the soot is agglomerated into chains up to about 2000 Å in length, and that the value of r is 0.950 ±0.004. It is concluded that this experiment strongly indicates that soot particles do form elongated agglomerates in flames. Since depending upon the degree of alignment, emissivity also depends on polarization. Therefore, the measured intensity at a fire detector may depend upon the polarizational state of the laser employed.

CHAPTER 3

A LASER DIFFERENTIAL INTERFEROMETER FOR FIRE RESEARCH

3.1 Introduction

As a method of rendering the refractive index- and bence temperature and / or composition- changes associated with combustion phenomena visible, optical methods possess many distinct advantages over other measurement methods in combustion research. First, the measurements do not disturb the temperature field since in most cases the energy absorbed by the medium is small compared to energy release by combustion. There is also practically no inertia errors in optical methods so that rapidly changing processes can be accurately followed. This advantage is additional to the possibility of recording the entire temperature field on a single photograph or, in the case of rapidly changing refractive index field, in a series of cine records. The information usually obtained from point-by-point measurements is instead deduced from evaluations of the photographs. These measurements are frequently of greater sensitivity than those using other methods, for example, the measurements of temperature fields using thermocouples.

However, in using focused optical records, the physical dimensions of the object under study are limited by the available sizes of conventional optical elements such as mirrors and lenses. This is a problem in fire research, since in this case, the objects of interest generally exceed a foot in diameter. Creeden et.al.(19) have devised a large area laser interferometer based on differential interferometry which allows a field coverage of 10 m. in diameter using a 50 mW laser. This method is extended by using a 4-watt argon ion laser, which would cover a field of 50 m. in diameter for continuous viewing. In addition, a large-deflection shadowgram can be superposed on the interference pattern by making the object to receptor distance large, and the fringe distortion can be used to analyse the light distributions in the shadow. The fringe displacement, Δy, is:

$$\Delta y = \xi \int (\mathrm{grad}\ n/n)\, dx \qquad 3.11$$

For very 'large' test object, e.g.the burning of full scale models, however, a problem arises in resolving the fringe structure on the photographic record. Increase the fringe spacing would result in the loss of detail in the test space. There is clearly a limitation to the practical sizes of photographic anlargement.

A technique based on the formation of Moiré fringes between double exposures was therefore devised which caters for both visualization and for detailed quantitative analysis of the refractive index field.

Using this method both the infinite and finite fringe differential interferogram can be obtained. The infinite fringes display contours of constant deflexion while the fringe displacement in finite fringe differential interferometry is proportional to the deflexion in the direction of shear. Both types of fringe patterns may be visualized either by the superposition of the specimen interferogram (interferogram taken in the presence of the test object) with the reference interferogram (taken in the absence of the phase object). The resulting pattern may be viewed against a diffuse light background, or in the case of parent fringes too fine to resolve by a method of reconstruction by diffracted light.(20)

Differential interferometry and particularly the large area laser differential interferometer will be discussed in the next section. Derivation of the fringe displacement and the Moiré fringe technique, together with experimental tests will be presented in the other sections of this chapter.

3.2 Principle of Differential Interferometry and Its Relevance to Fire Research

With the advent of laser light sources, interferometers are generally no longer more difficult to set up then either shadow or schlieren techniques. Nevertheless, with the magnitudes of temperature gradients often encountered in combustion, for example, flames at atmosphere pressure, conventional interferometry, in which the fringes give contours of constant optical path may be inferior to methods which yield the optical path gradient directly (21). Deflection mapping, which fulfils this purpose is unfortunately not satisfactory when applied to fire research.

The reason is that for sufficient sensitivity, the value of ξ (about 2m.) required would usually be such as to render any record by such shadow casting illegible due to diffraction. This problem is overcome using differential interferometry in which the shift of initially straight fringes is proportional to the optical path gradient because, in this case, the effect of diffraction is no longer present.

3.2a <u>Differential interferometry</u>

Considere a plane wave front; after passage through a refractive index field, it will be deformed. The structure of such a wave front can be made visible by interference methods, in which phase differences between the deformed wave front and the reference wave result in intensity changes. The crucial difference between conventional and differential interferometry is in the form of the reference wave front. In conventional interferometry, the reference wave does not pass through the test object. In the case of a plane reference wave front, the contour lines are the intersection of parallel equidistant plane surfaces with the distorted wave front. In differential interferometry, however, the reference wave front is not a plane wave front, but the same deformed wave front with a lateral displacement, since both beams pass through the test object with a lateral displacement before they interfere. If the lateral displacement is very small (infinitesimal shear) the interference pattern is a measure of the gradient of the deformed wave front.

Consider an aberration-free two beam interferometer. The phase difference between the two interfering beams due to the phase object is :

$$\Delta\phi = \phi_m - \phi_r \qquad 3.2a.1$$

In conventional interferometry, referring to Cartesian coordinates:

$$\Delta\phi = 2\pi/\lambda_0 \; \{ \int_{ray} n_p(x,y,z)dx - \int_{ray} n_r dx \}$$

$$= 2\pi/\lambda \int_{ray} \{ n_p(x,y,z) - n_r \} \; dx \qquad 3.2a.2$$

whereas in differential interferometry:

$$\Delta\phi = 2\pi/\lambda_0 \; \{ \int_{ray} n_p(x.y.z)dx$$

$$- \int_{ray} n_p(x.y-y_s, z-z_s)dx \}$$

$$3.2a.3$$

where y_s and z_s represent the shear of the beams along the y and z directions in the object plane. When these shears are very small in comparison with the dimensions of the phase object (for the large area interferometer, the shear at the beam splitter is 1 mm. for a fringe spacing of 1 mm. at a screen 2 m. away from the beam splitter), then using Taylor's expansion and neglecting second and higher order terms, equation 3.2a.3 may be written:

$$\Delta\phi = 2\pi/\lambda_o \int_{ray} \{y_s(\partial n_p/\partial y)+z_s(\partial n_p / \partial z)\}dx \qquad 3.2a.4$$

It follows that the fringe displacement is proportional to the gradient of the object refractive index field.

3.2b A Large-Area Laser Differential Interferometer

Wave front shearing was achieved by using the front and rear reflections from a back surfaced mirror. In Figure 3.1a (ox', oy' oz') is the laboratory frame of reference and (ox , oy , oz) is the coordinate system with reference to the beam splitter S. The incident and reflected beams lie along the z-x plane as depicted in Figure 3.1b. The shear is, at the beam splitter is :

$$s = 2e(n_g^2 - \cos^2\gamma)^{\frac{1}{2}} \qquad 3.2b.1$$

The optical system of the large-area differential interferometer is shown schematically in Figure 3.2. The light source was a Spectra-Physics 4-watt argon ion laser. L_1 is a X10 microscope objective which focused the beam

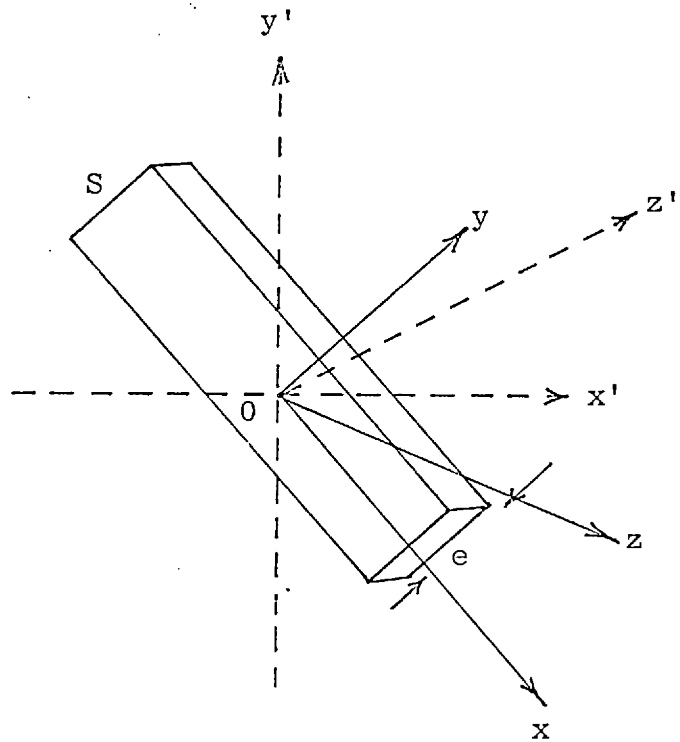

Figure 3.1a

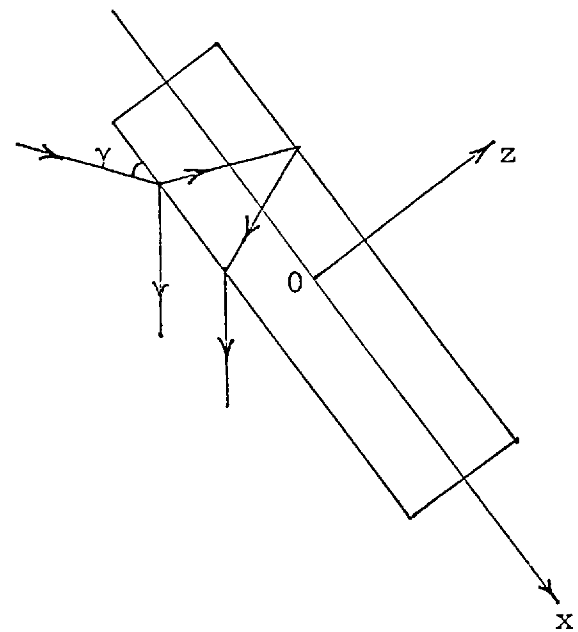

Figure 3.1b

Figure 3.1a & b   Coordinate system of the beam splitter S

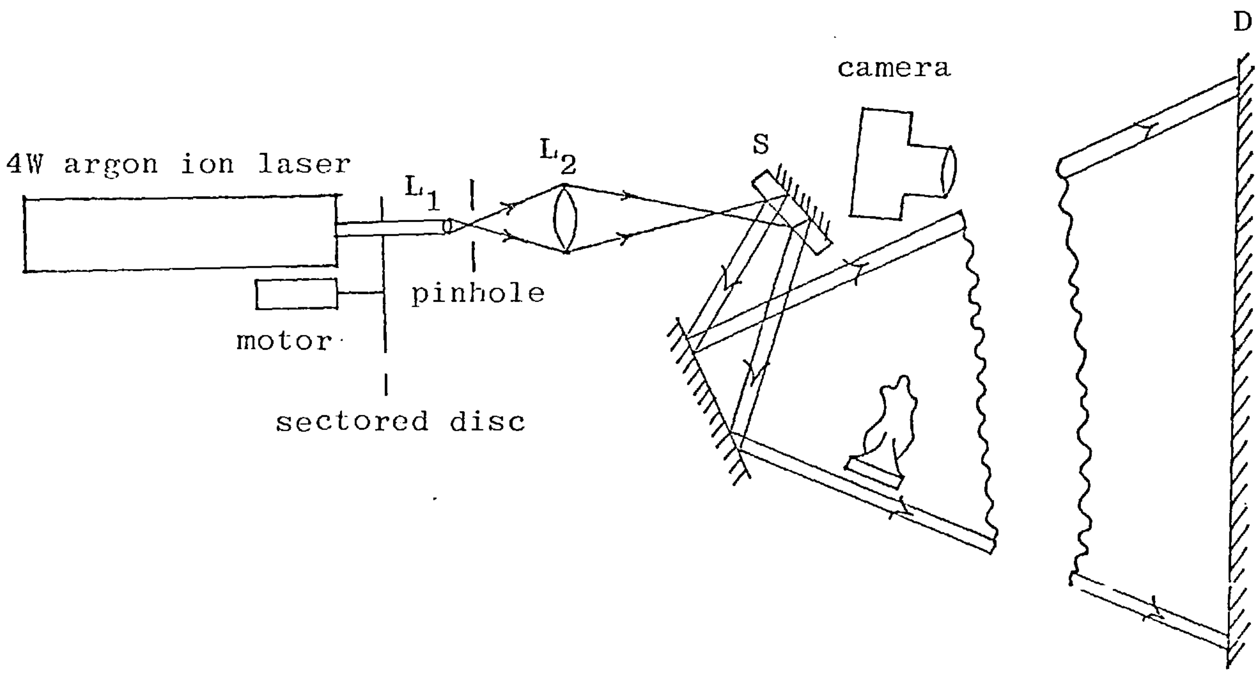

Figure 3.2 Schematic diagram of the large area differential interferometer

onto a pinhole filter. The focal length of the lens L_2 was chosen according to the required beam divergence. The back-silvered mirror S was used at an oblique incidence to ensure approximately equal illumination in the two beams and hence a good legibility. By placing it close to the focal point of L_2, two wave fronts diverging spherically from the two principal point reflections are produced (the sectored disc was not used here, its function will be discribed in the next chapter). The shear s_t at the test space is (Figure 3.3):

$$s_t = \xi \ s/\eta = \{ \ 2e(n_g^2-\cos^2\gamma \ )^{\frac{1}{2}}\xi\} /\eta \qquad 3.2b.2$$

and the fringe spacing q is:

$$q = \lambda\eta/s = (\lambda\eta)/2e(n_g^2-\cos^2\gamma)^{\frac{1}{2}} \qquad 3.2b.3$$

Thus q can be varied by altering the angle γ , the refractive index n_g of the beam splitter or, for larger variations, its thickness. The test object was placed in front of the screen D at a distance determines by the sensitivity required. The screen was either a piece of tracing paper attached to an open door-way, in which case the photographic records were taken from the room on its reverse side, or a piece of white cardboard photographed from the front. With the screen diameter at 0.8 m. and the laser power set

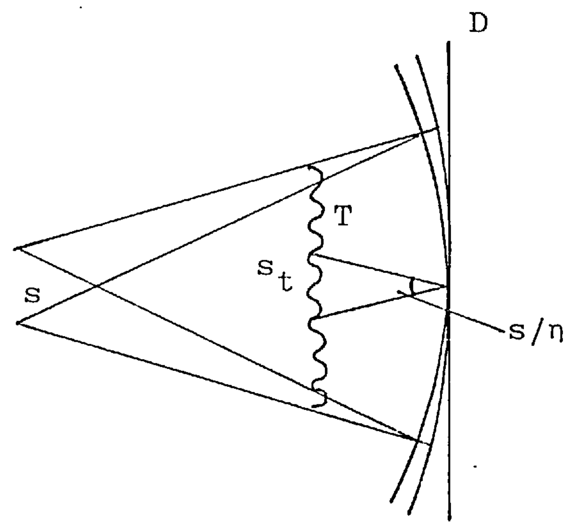

Figure 3.3 Diagram showing the shear between two spherical wave front

at 800 mW, an exposure of 1/1000 sec. was sufficient with the particular size of pinhole employed. The maximum area is proportional to the power available. For a light source emitting at 5550 Å, the luminous efficiency is approximately 660 lumens/watt. The laser was operating at a wave length of 5145 Å and at this wave length the relative sensitivity of the eye is about 0.7 and the luminous efficiency of the laser was thus roughly 450 lumens/watt. Therefore, the maximum luminous flux that the laser can emit is 1800 lumens. Assuming that for continuous viewing, one lux of illumination is required, then with the laser full on at 4 watts one should be able to produce an usable field of about 50 m. in diameter. Figure 3.4a is a photograph of the fringe pattern where the fringe spacing is 4 mm.. Figure 3.4b shows the shifts in the fringes due to an electric bar heater parallel to the beam. The deduction of integrated optical path (and hence appropriate mean temperature) follows from equation 3.2a.4. In the case of fire research, however, some of the more specific ooptical criteria used in flame research (21), appear useful. These concern, for example, the precise location of the first onset of temperature rise, and the deduction of the maximum temperature, neither of which requires an unidimensional distribution. The former is based on locating the temperature of maximum refractive index gradient by drawing tangents parallel to the undistorted fringe direction to locate the maximum displacement. The latter is based on measuring the area occluded between the distorted fringe and its undistorted original position-

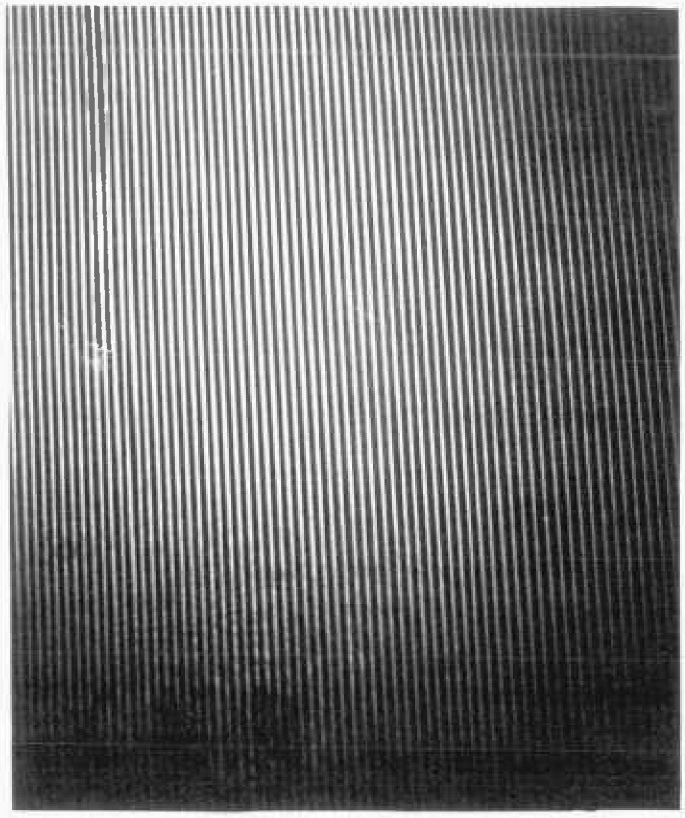

Figure 3.4a Fringe pattern obtained using the optical system shown in Figure 3.2

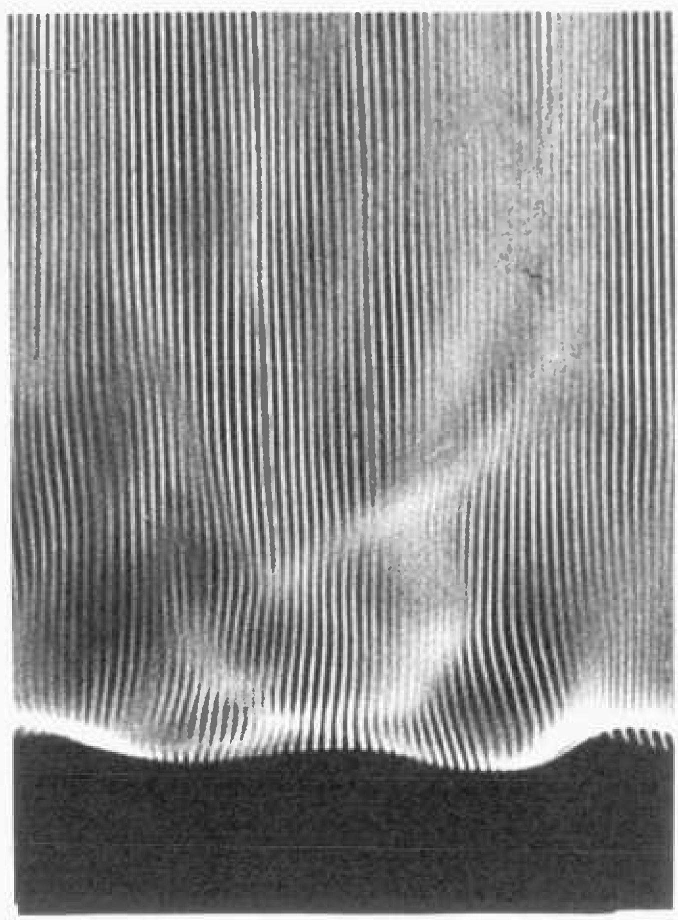

Figure 3.4b Shifts in the fringe pattern due to an electric bar heater

a simple form of intergration of the differential record which can be used to deduce the final state without knowing the flame shape (21) for reasonably gradual curvatures. All these become possible because of exact correspondence between fringe distortion and that of a hypothetical grid shadow (section 3.3).

3.3 Fringe Displacement, Moiré Fringes and Reconstruction by Diffracted Light

3.3a Fringe Displacement and Deflection Mapping

Figure 3.5 illustrates the formation of the distorted shadow G, consisting of parallel slits, following deflection of light by the test object T. For gases, the refractive index $n_p \simeq 1$ and the displacement Δy in the y direction (vertical on the diagram) from the unperturbed shadow position is :

$$\Delta y = \xi \, \theta = \xi \int_{ray} (\partial n_p / \partial y) \, dx \qquad 3.3a.1$$

The backgroung to this derivation is fully discussed by Weinberg (21), along with the effective sensitivity of the method (taking into account the inevitable magnification) and the limitation imposed by diffraction.

For the differential interferometer, consider deflection in the y direction only, we have:

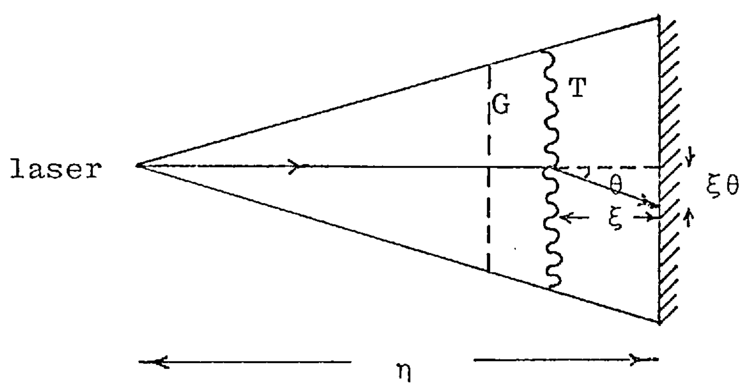

Figure 3.5 Formation of a grid shadow.

$$\Delta\ y = (q/2\pi)\Delta\phi \qquad 3{\circ}3a{\circ}2$$

Using equations 3.2a.4 and 3₀2b.3, then:

$$\Delta\ y = (\eta y_s\ /s) \int (\partial n_p / \partial y)\ dx \qquad 3{\circ}3a.3$$

From equation 3.2b.2, equation 3₀3a.3 becomes:

$$\Delta y = \xi \int (\partial n_p / \partial y)\ dx \qquad 3{\circ}3a.4$$

The identity of equations 3₀3a.1 and 3.3a₀4 shows that for the interferometer, except for the absence of diffraction problems, each fringe behaves precisely like the shadow of a slit placed ahead of the test space. For this reason also, temperature can be deduced for moderately curved flames, without knowledge of their precise shape, in terms of the area enclosed between the distorted fringe and the unperturbed shape.

3.3b <u>The Moiré Fringe Technique</u>

The inter-fringe spacing, f, between two successive Moiré fringes formed by the superposition of two similar gratings depends upon the angle between their rulings and the pitch, p, of the gratings. Thus f can be made very much larger than p and similarly the magnitude of any deformation inherent in the specimen grating may be correspondingly magnified by superposing onto it a reference grating and observing the resulting Moiré fringe pattern. This is very useful since in conjunction with the large area interferometer, it provided the basis of a technique for the measurement of the refractive index gradient distributions across a very large test space. The specimen grating in this case was a photographic plate exposed at a sufficiently short time interval to 'freeze' the fringe displacements and the camera was positioned at a distance so that the image of the whole large area interferogram would be contained in a single plate. The reference grating was an identical photographic plate exposed under the same conditions in the absence of the test space.

In order to test the method, the test object used was a model house with one wall exposed to radiation from an electric fire, simulating radiation from another burning building. Figure 3.6a is a large area interferogram of the system and Figures 3.6a & b are magnified photographs (14X) showing respectively the fringe deflections along the wall and around a corner of the model house. By adjusting the two 'gratings' we can obtain either the infinite or the finite fringe condition. The infinite fringe interferogram results when the two plates are oriented parallel to one another and when there is point to point correspondence within the test space. This is

(a)

(b)

(c)

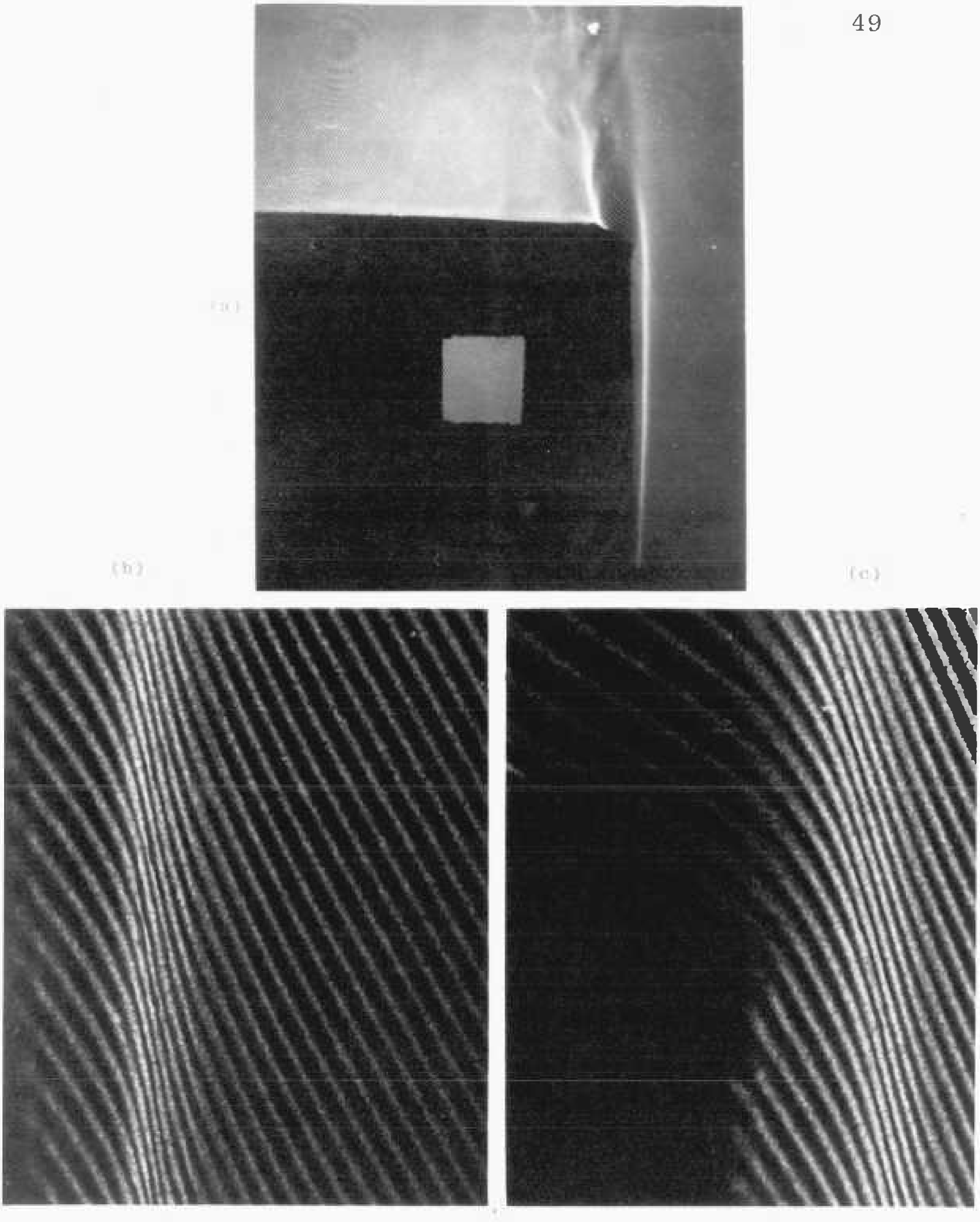

Figure 3.6 a Large area interferogram of the heated wall.

Figure 3.6 b & c Magnified photographs (14x) of selected areas of the interferogram shown in Fig. 3.6 a depicting fringe deflections.

shown in Figure 3.7a. Yet another method for obtaining the infinite fringe interferogram is the double exposure/ single plate technique. An exposure is taken of the large area interferogram with the phase object in the test space, without moving the photographic plate, the plate is again exposed in the absence of the test object. The infinite fringe interferogram is obtined after reconstruction using the optical system shown in Figure 3.7b. The plate may be illuminated with a wave front of the same curvature as the reference wave front used during the original recording and the reconstruction is formed in the image plane along one of the diffraction orders. An example of the reconstruction is shown in Figure 3.7c, the test object in this case being a candle flame. It is important to note that the method of reconstruction by diffracted light may be used for any carrier fringe frequency. However, useful observation of Moiré fringe patterns by the superposition of the specimen and reference gratings is only possible when the carrier fringe frequency is coarse enough to be resolved by eye.

The infinite fringes are fringes of iso-deflection contours and using very fine fringes followed by such reconstruction fine detail can be resolved over enormous areas. The sensitivity of the method may be estimated. For an object of 1 m. in length placed parallel to the leight beam and assuming that the test object is placed 3 m. away from the screen, using a photographic emulsion capable of separating 6000 lines per mm.(maximum resolution) and the camera in a position such that on record, the

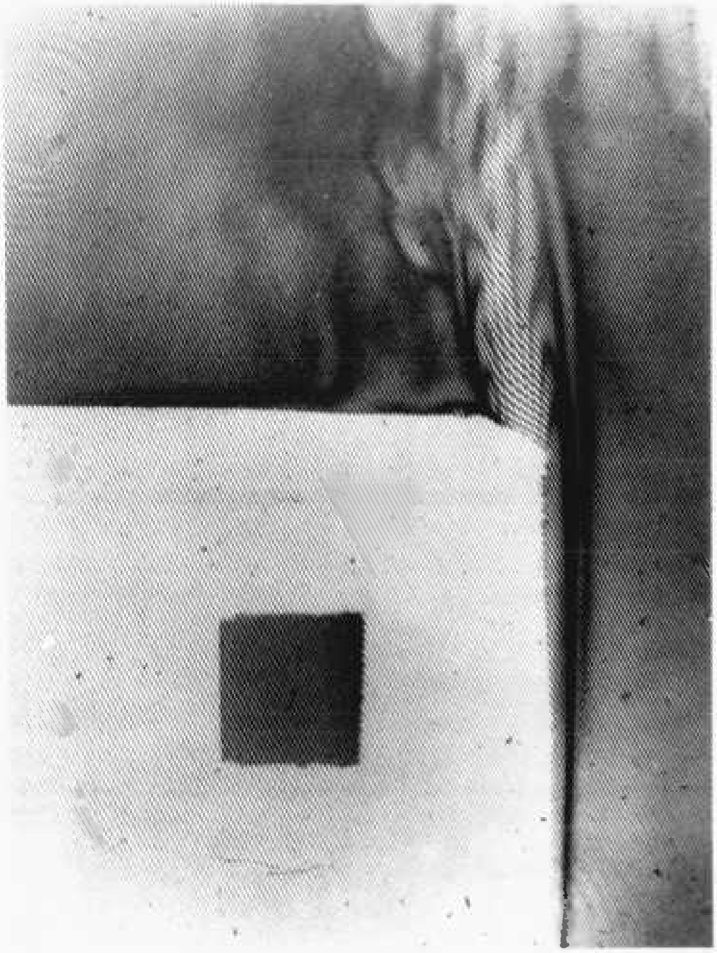

Figure 3.7 a Moiré fringe pattern of the heated wall, showing the infinite fringe condition.

Figure 3.7 c Reconstruction of a candle flame.

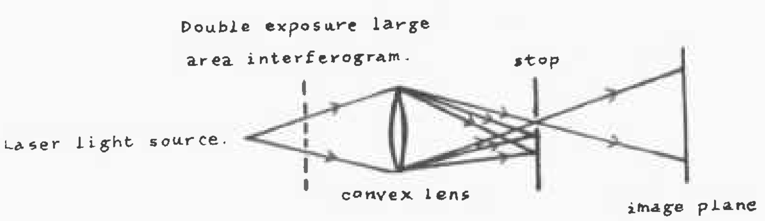

Figure 3.7 b Optical system for reconstruction.

magnification is 1/10:

$$(dn/dy) \times 100 \times 300 = q = 1/6000$$

But

$$dn/dy = d\delta/dy = (\delta_o T_o/T^2)\ dT/dy$$

Therefore:

$$dT/dy = (T^2/\delta_o T_o)\ 1/1.8 \times 10^8$$

$$\simeq T / \delta_o \times 1.8 \times 10^8$$

and

$$(dT/dy)_{min} = (3 \times 10^2) / (3 \times 10^{-4} \times 1.8 \times 10^8)$$

$$\simeq 5 \times 10^{-3}\ ^\circ C \text{ per cm.}$$

Thus it is possible to obtain one complete fringe for a temperature gradient of 0.05 $^\circ$C per cm.

The finite fringe interferogram can be obtained simply by rotating the two 'gratings' with respect to each other. Such a finite fringe pattern of the heated wall is shown in Figure 3.8. The refractive index gradient distribution, the wall temperature distribution and the corresponding approximate isotherms deduced are shown in Figures 3.9a,b and c respectively.

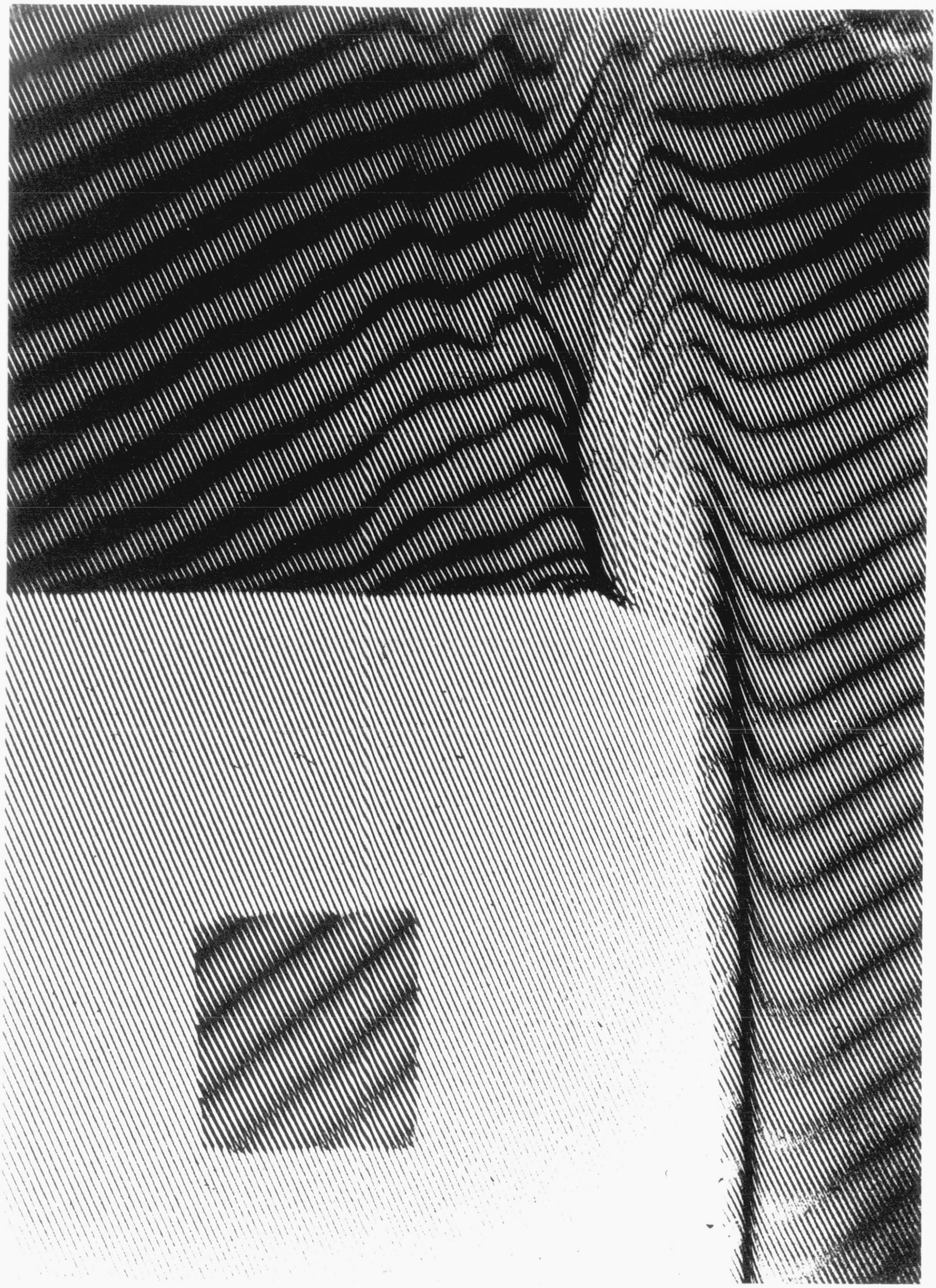

Figure 3.8 Moiré fringe pattern of the heated wall, showing a finite fringe condition.

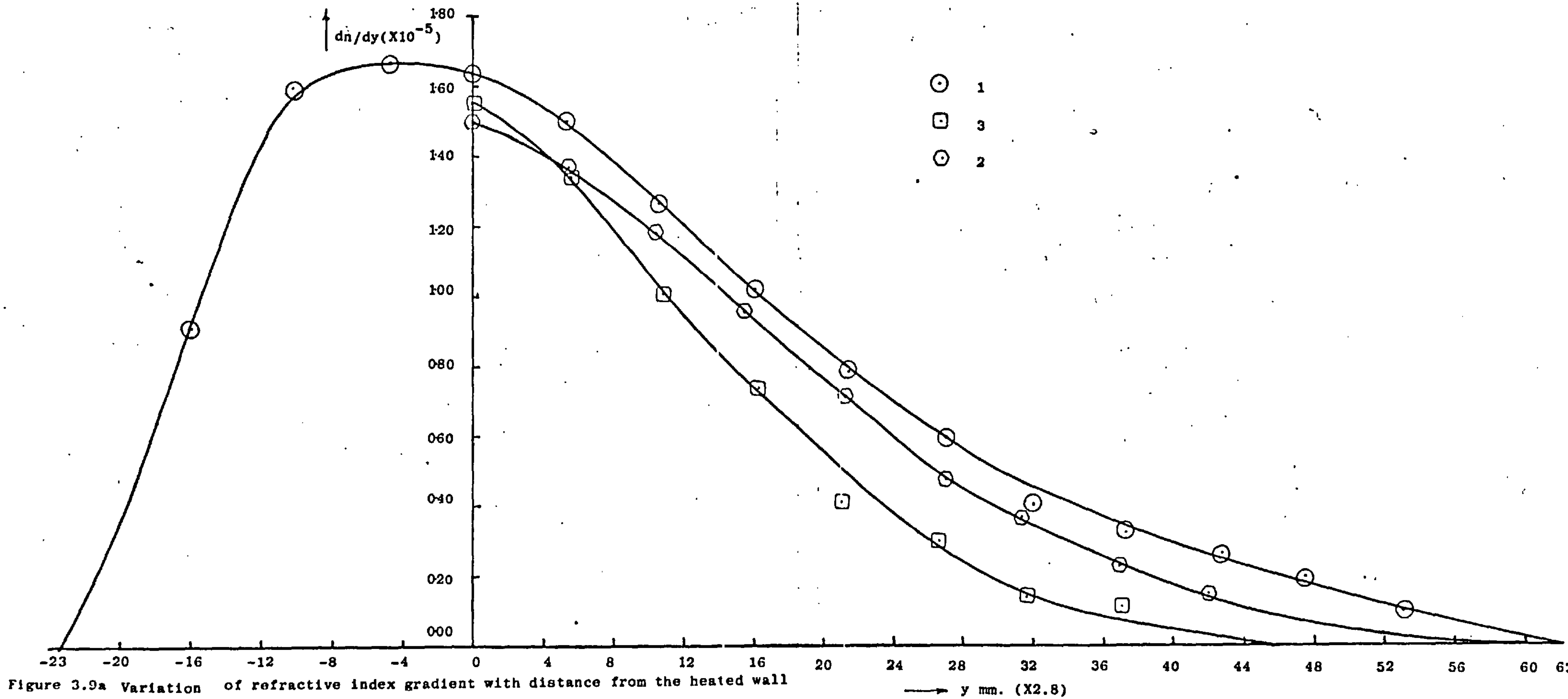

Figure 3.9a Variation of refractive index gradient with distance from the heated wall

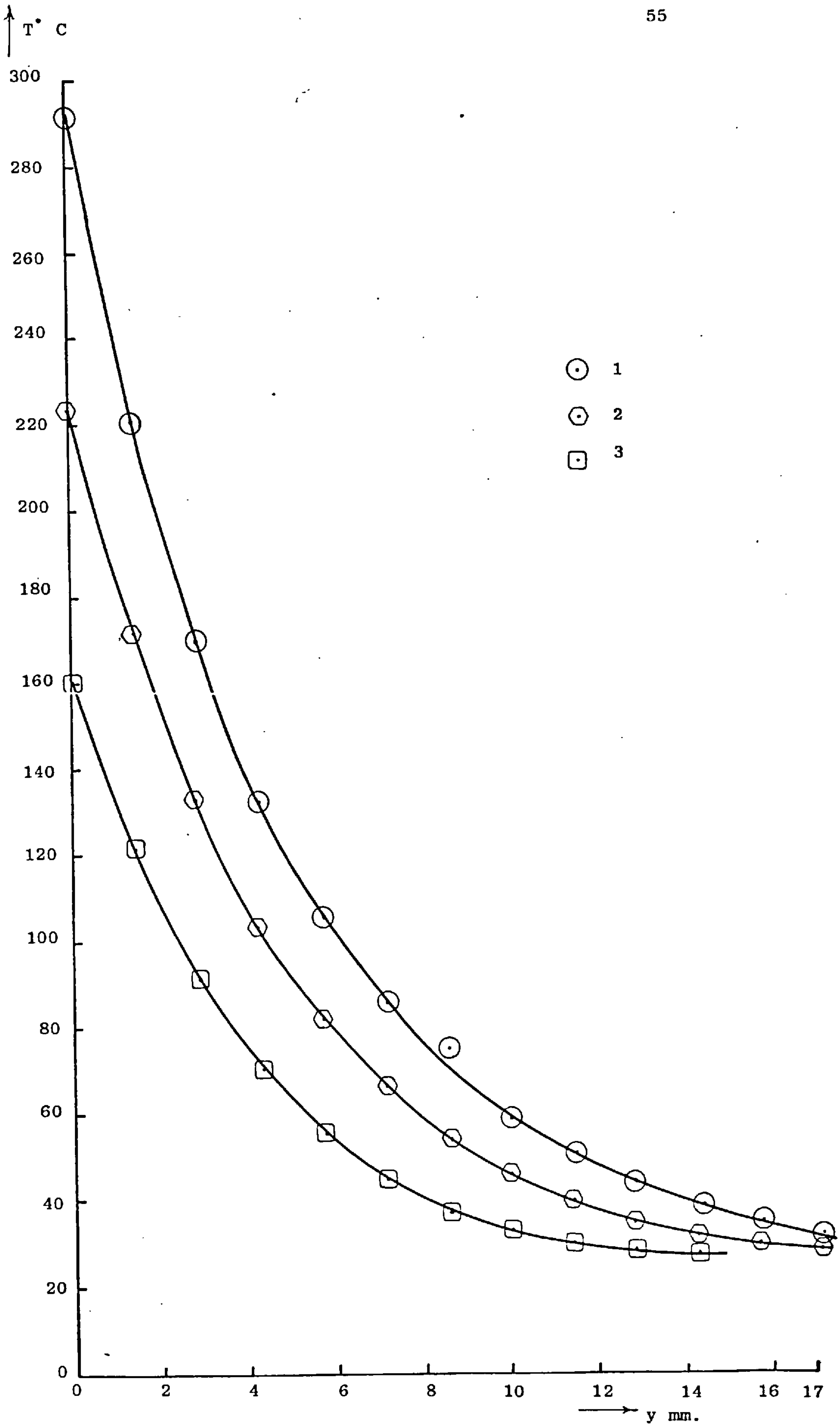

Figure 3.9b Variation of temperature with distance from the heated wall

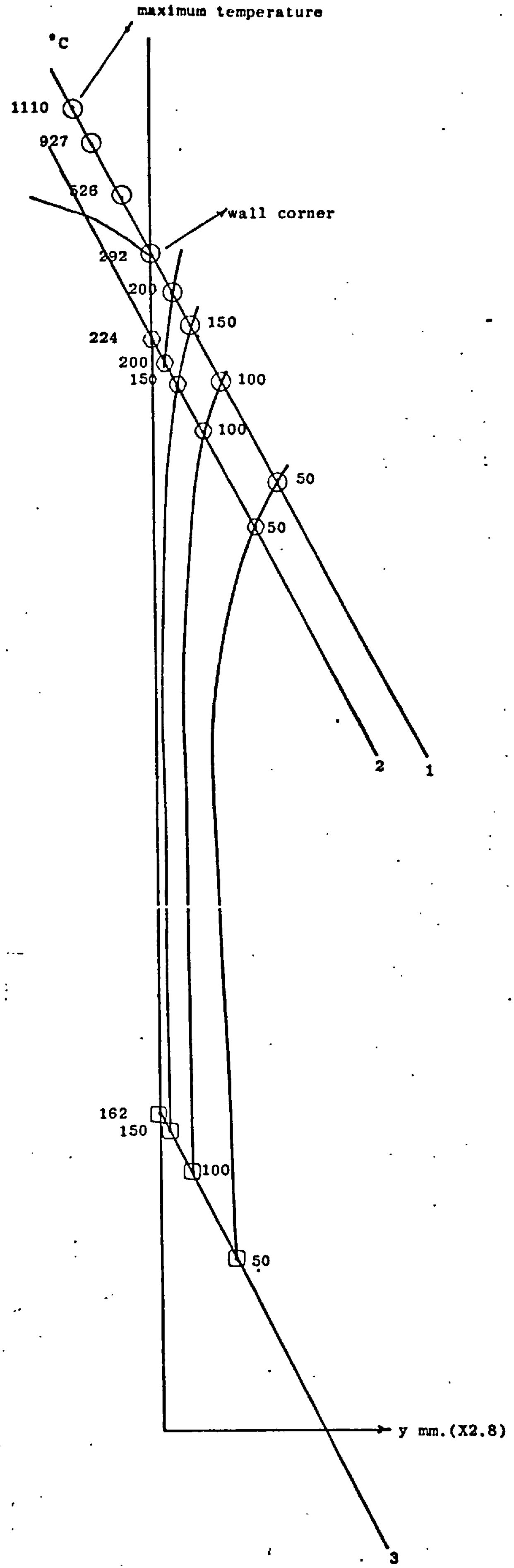

Figure 3.9c Deduced approximate isotherms around the heated wall.(scale 2.8X)

Using a plane glass slab instead of a back surfaced mirror as the beam splitter, a further development of the method is proposed (Figure 3.10). Fringe patterns 1 and 2 are identical sets of fringes and their intensities can be made to match by placing a variable neutral density filter between the path of one of the beams. When these two sets of fringes are brought together, a Moiré fringe pattern is formed directly on the screen (provided the separation between the fringes is large enough to be resolved) and by adjusting their orientation with respect to each other, both infinite and finite fringes may be obtained, Thus changes in either the iso-deflection contours or a finite fringe pattern as a large test object undergoes the process of combustion can be directly visualized or cine records may be taken for further analytical or demonstration purposes (This is evidently only possible for coarse fringes, otherwise one would still have to reconstruct).

3.4 Conclusions

A large area interferometer using as the light source, a 4-watt argon ion laser has been shown to be particularly useful in fire research since its usable field coverage could be as large as 50 m. in diameter for continuous viewing. The fringe displacement was demonstrated to be directly proportional to the optical path gradient. Furthermore, the system is simple to set up and it was shown that the fringe spacing may be

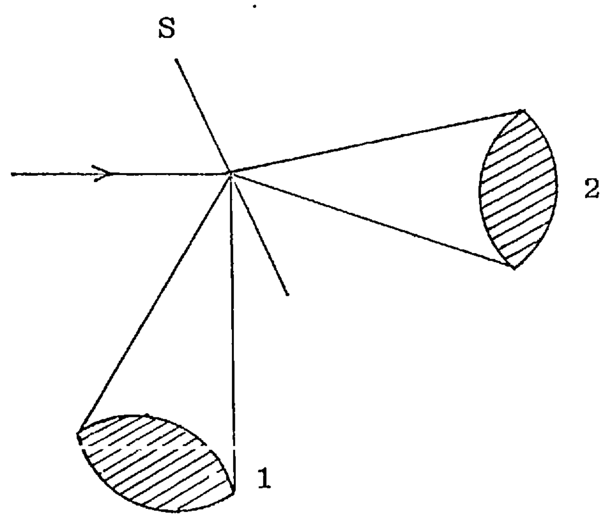

Figure 3.10 Formation of two idential sets of fringes 1 & 2 using a glass slab S as the beam splitter.

easily varied from relatively coarse fringes for visualization to fine fringes for detailed analysis of the refractive index gradient distribution of the test object by altering the angle of the back surfaced mirror, its refractive index and / or by using mirrors of different thicknesses.

The usefulness of the interferometer was further extended by a new method based on the formation of Moiré pattern between interferograms in the presence and absence of the test object. It was demonstrated that using this technique, both infinite and finite fringes can be obtained over very large areas with a sensitivity depending upon the length of the test object that is parallel to the light beam, the fringe spacing and the distance of the test object from the screen. It was shown that the minimum measurable temperature gradient can be very small indeed.

CHAPTER 4

LASER OPTICAL METHODS FOR THE MEASUREMENT OF VELOCITIES OF PHASE OBJECTS

4.1 Introduction

Velocity is one of the most important physical parameters in the understanding of combustion systems. For example, in evaluating and improving the performance of laser fire detectors, it is essential to know the velocity distributions of turbules within fire plumes. A knowledge of velocity is also an absolute necessity in the study of laminar and turbulent gas flows, the propagation of flame fronts, detonation fronts and shock fronts.

Therefore, it is of little wonder that a great deal of effort in combustion research has been directed towards devising and improving methods of velocity measurements. The various techniques that exist for making such measurements all require the simultaneous recording of both distance and time intervals. Methods such as cine or streak schlieren photography, timing between ionization probes a known distance apart and repetitive illumination of particles suspended in a gas are well-known techniques. A method was devised by Schwar and Weinberg (22,23,24) in which they applied schlieren interferometry to Doppler-shifted laser light for velocity measurements on moving media with density gradients. Their method has the great merit of non-interference and simplicity. It also has the advantage of not requiring any other optical components than are necessary in a conventional schlieren system.

Normal propagation velocity plays a particularly significant part in combustion, since flames in premixed gases, detonations and various other phenomena propagate at a constant velocity in a direction perpendicular to the local orientation of their fronts. Those which travel at a speed less than that of sound - and our primary concern is with burning velocities - tend to induce motion ahead, in the medium into which they are propagating, even in the absence of a deliberately induced flow field. This in turn, affects their geometry. Thus the shape of a flame propagating into a container filled with a mixture of reactants is determined by the gas flow ahead of it induced by the expansion of products, even though each element of the front propagates at the burning velocity orthogonal to the local isotherm surfaces. In the case of flames stabilized on burners, the shape is, of course, determined by the incident velocity distribution in such a way that its local component perpendicular to the flame front just balances the burning velocity.

Various surveys have been made of experimental techniques for the measurement of burning velocity (25,26,27). From these reviews, it is seen that all the existing methods require some measure of flame shape (angle subtended with local flow vector,area,etc.) in addition to one of velocity (of flow, flame, or both). In this work, a novel method based on the equivalence of "Doppler Velocimetry" and fringe anemometry is proposed in which this orthogonal component is measured directly whether the phase object is stationary, moving or fluctuating.

The theory of the method of measuring the velocity of any moving object by applying schlieren- interferometry to Doppler-shifted light is given together with a formal proof that the observed beat frequency may be interpreted as the motion of interference fringes across the front of a photodetector. A special "schlieren blind" is described which was constructed in such a way that each part of a moving phase object, such as a flame, is displayed as a fringe pattern parallel to its local refractive index contours.

The Doppler principle was first formulated by C.J.Doppler (28) during the course of developing a theory to explain the colour of the light coming from moving stars in 1842. The Doppler effect can be applied to measure velocities by the direct measurement of the shift in wavelength of light emitted by the moving body itself (29) or that scattered from an external source (30). Assuming that conventional spectroscopic techniques are capable of resolving spectral shifts in the visible down to about 0.005 Å (31), then the minimum velocity that can be measured in this way is about 30 ms^{-1}. The minute change in frequency caused by slower moving bodies - this include all burning velocities - can be measured by observing the beat frequency, ν_b , which results when the Doppler-shifted wave is made to interfere with a reference wave. The advent of lasers has provided the high intensity, monochromatic light sources necessary to permit ready application to numerous laboratory configurations with spatial resolution of less than one cubic millimetre (32). Since frequency meters covering a very wide range of values are available, velocity measurements can be performed for flow speeds lying between fractions of a millimetre per second and large supersonic velocities.

Various optical arrangements have been demonstrated for measuring the velocity of individual particles suspended in a gas or liquid (33,34,35, 36). In these attempts, scattering by the particles was utilized, at the focus of a strongly convergent beam. The method used by Schwar and Weinberg (23) has the advantage that the system selects rays that have been deflected through particular angles, so that it is possible to measure the individual velocity of any phenomenon which will reflect, refract, or diffract a laser beam. The method proposed here also incorporates a schlieren interferometer, the schlieren blind being designed in such a way that rays, deflected through a particular solid angle are selected and it is demonstrated that this method can be applied to measure the normal velocities of both moving solid and phase objects directly.

The laser Doppler velocimeter has also been used to study turbulent flows. This involved the measurement of the root-mean-square value of the fluctuating velocity component. Goldstein and Hagen (37) measured the probability function for the turbulent velocity distribution in a duct flow of water containing polystyrene particles. Pike et.al. (38) obtained satisfactory agreement with hot-wire-anemometer data for the value of turbulence intensity in turbulent pipe flows of CO_2 in a plot involving the Reynolds' number as correlation parameter. The advantages of the Doppler technique over that of hot-wire anemometry are that of far superior spatial resolution and versatility.

Therefore, for the purpose of studying turbulence within fire plumes, the laser Doppler velocimeter can be used . However, spatial resolution is not important in this case due to the large size of the turbules. With reference to the large area laser differential interferometer described in Chapter 3, we may superimpose a large - deflection shadowgram on the interference pattern by making the object to receptor distance large, and the fringe distortion can be used to analyse the light distributions in the shadow. Therefore, by using interrupted shadow interferometry, we have a shadow record of the fire plume and the velocities of the hot turbules may be determined from multiple exposures taken at fixed time interval. The fundamentals of measuring the mean velocity and turbulence intensity using the proposed method to the study of fire plumes is described. However, the main body of these results will be presented in the next chaper.

4.2 Theory of Doppler Velocimetry

When a beam of light is deflected by a moving object, there will be a frequency shift of the light. This is the basic principle underlying Doppler velocimetry. Here, a general expression relating the beat frequency to the direction of the incident light, the velocity of the object and the direction of observation is derived. Its application under various experimental arrangements is explained. Finally a formal proof of its equivalence with a moving interferogram is given.

4.2a Beat Note Between Differentially Frequency - Shifted Light Beams

Since velicities of interest in combustion are generally very small compared to the velocity of light. A non-relativistic treatment is given here.

In Figure 4.1, consider an object, which can be a scatterer or a phase object, moving with velocity $\underline{v}$ ($|\underline{v}| << c$). Monochromatic radiation of wavelength λ_i and speed c, emanating from a nonmoving source in the direction defined by the unit vector $\hat{\underline{k}}_i$ illuminates the

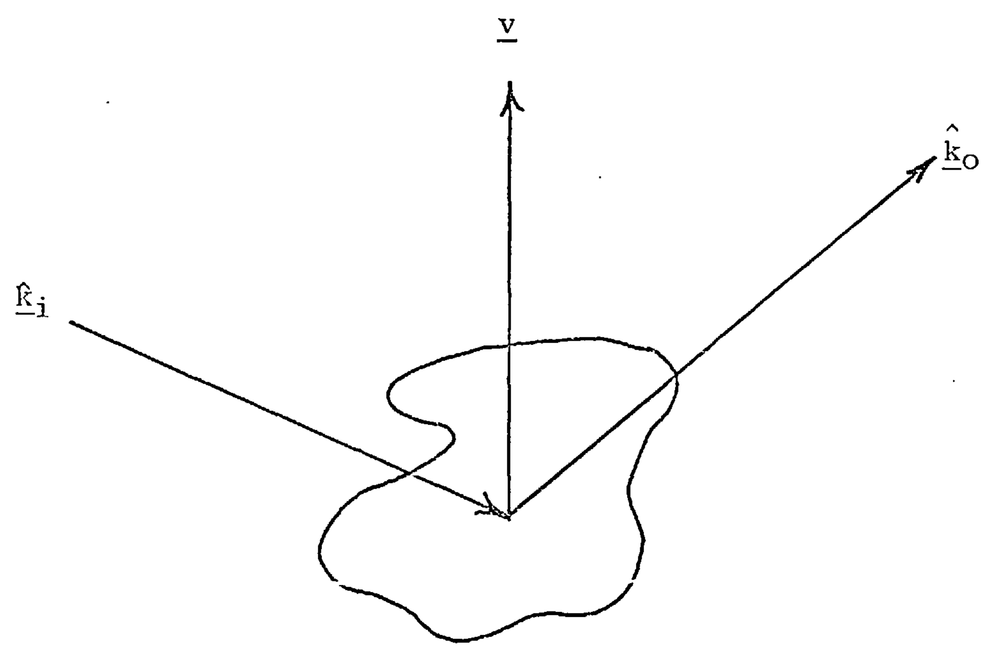

Figure 4.1 Diagram defining incident, observation and velocity vectors

object.

When $| \underline{v} | = 0$, the number of wave fronts passing the object per unit time is c / λ_i. However, for non-zero values of $| \underline{v} |$, the apparent frequency to the object is :

$$\nu_a = (c - \underline{v} \cdot \hat{\underline{k}}_i) / \lambda_i \qquad 4.2a.1$$

Consider now a fixed observer toward which the moving object is emitting radiation in the direction defined by the unit vector $\hat{\underline{k}}_o$. After the emission of one wave front, the object moves toward that wave front with the speed $\underline{v} \cdot \hat{\underline{k}}_o$. Thus, when the next wave front is emitted after a time interval given by $1/\nu_a$, the first wave front is a distance of $(c \; \underline{v} \cdot \hat{\underline{k}}_o)/\nu_a$ away from the object. Thus, to a fixed obsever, the apparent wavelength of the emitted radiation is:

$$\lambda_o = (c - \underline{v} \cdot \hat{\underline{k}}_o) / \nu_a \qquad 4.2a.2$$

and the frequency of the emitted radiation is :

$$\nu_o = c/\lambda_o = c/\lambda_i \left\{ \frac{1-(\underline{v} \cdot \hat{\underline{k}}_i/c)}{1-(\underline{v} \cdot \hat{\underline{k}}_o/c)} \right\}$$

4.2a.3

The beat frequency ν_b is:

$$\nu_b = \nu_o - \nu_i$$

or

$$\nu_b = 1/\lambda_i \left\{ \frac{\underline{v}.(\hat{\underline{k}}_o - \hat{\underline{k}}_i)}{1-(\underline{v}.\hat{\underline{k}}_o/c)} \right\} \qquad 4.2a.4$$

Since$|\ \underline{v}\ | << 1$, we have:

$$\nu_b = 1/\lambda_i \{ \ \underline{v}.(\hat{\underline{k}}_o - \hat{\underline{k}}_i\ ) \} \qquad 4.2a.5$$

which is the general Doppler beat frequency equation. Combinations of $\hat{\underline{k}}_o$, $\hat{\underline{k}}_i$ and the direction of $\underline{v}$ can be selected to suit different experimental requirements.

4.2b <u>Some Applications of the General Doppler Beat Frequency Equation</u>

The first utilization of the Doppler velocimeter was that by Yeh and Cummins (33). They made a dilute colloidal suspension of polystyrene spheres in water and measured the velocity of the individual particles. Figure 4.2 shows the experimental arrangement, here $\underline{v}$ is chosen to be in the direction of $\hat{\underline{k}}_i$. Application of equation 4.2a.5 to the scattering geometry gives:

$$\nu_b = 1/\lambda_i \ \{\ v(-2\sin\frac{\theta}{2}) \cos(\pi/2- \ \theta/2)\ \}$$

or

$$\nu_b = -\ 2v\sin^2\frac{\theta}{2}\ \ /\ \lambda_i \qquad 2.2b.1$$

Goldstein and Kreid used a different optical system to

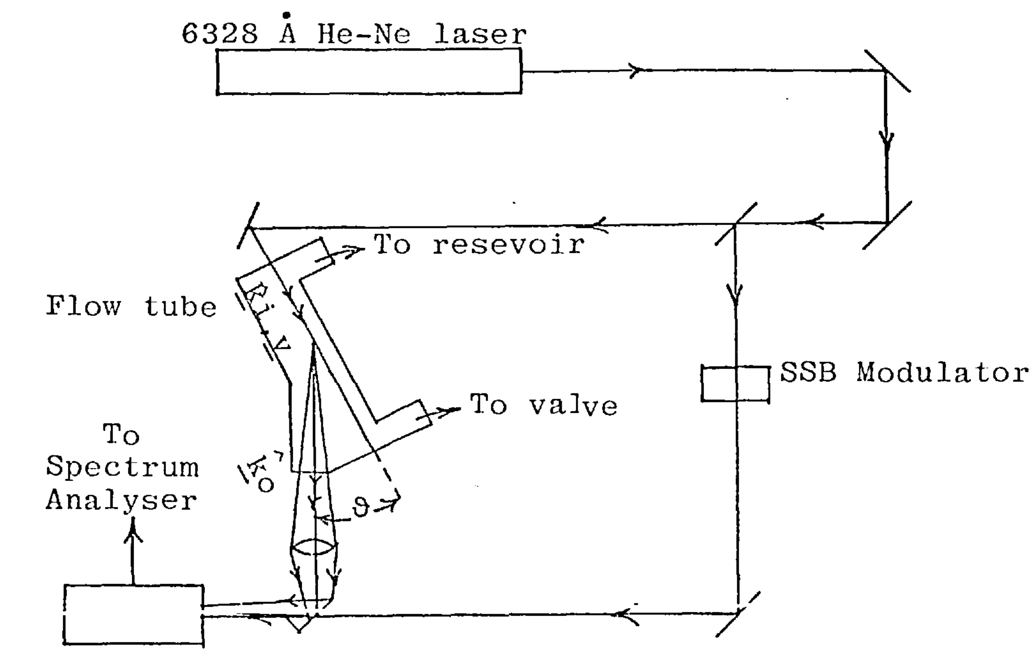

Figure 4.2 Experimental arrangement used by Yeh and Cummins for measuring velocity of particles

measure velocity in a laminar flow field. Their apparatus is shown in Figure 4.3. It was arranged so that the incident beam and the reference beam make equal angles with the plane normal to the tube axis. Referring to Figure 4.4, from equation 4.2a.5 :

$$\nu_b = 1/\lambda_i\{ \underline{v}.(2\sin\theta\ ) \hat{\underline{n}}\ \}$$

where $\hat{\underline{n}}$ is a unit vector in the direction of $\hat{\underline{k}}_o - \hat{\underline{k}}_i$

or

$$\nu_b = 1/\lambda_i\{ v\hat{\underline{n}}.(2\sin\theta\ ) \hat{\underline{n}} = 2\sin\theta\ v/\ \lambda_i\} \quad 4.2b.2$$

In both of these methods, alignment is difficult, since to ensure that the scattered beam and the unshifted reference beam do interfere, they must be mutually parallel and coincident when they strike the photodetector. This alignment problem also exists in most other systems (34,39,40). However, alignment is simple in the method proposed by Schwar and Weinberg (23), because the angle of deflection may be precisely defined using a parallel beam schlieren systerm in which the schlieren blind has a suitably positioned selective aperture. Figure 4.5 is a schematic diagram of their experimental arrangement.

From Figure 4.6 and equation 4.2a.5:

$$\nu_b = (v/\lambda_i)\ (-2\sin\tfrac{\theta}{2}\ )\ \cos\ \tfrac{\theta}{2}$$

or

$$\nu_b = -(v/\lambda_i)\ \sin\theta \quad 4.2b.3$$

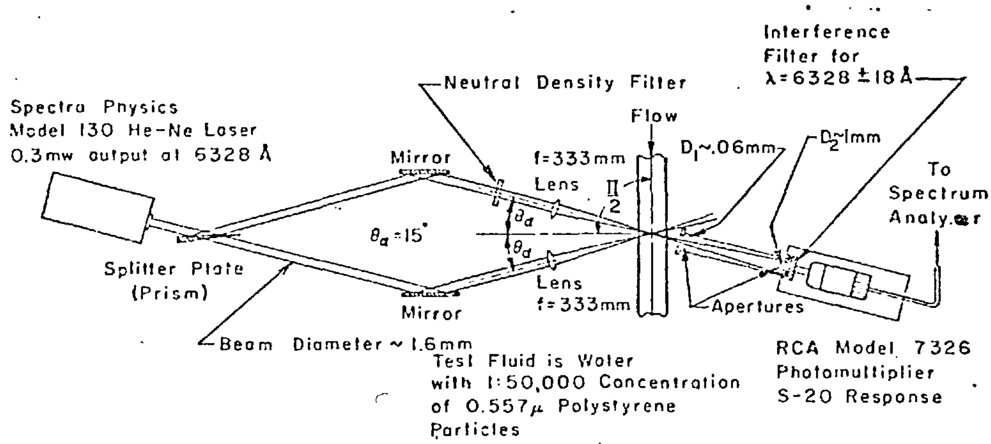

Figure 4.3 Optical system used by Goldostein and Kreid for measuring velocity in a laminar flow field (from Goldstein and Kreid, Journal of Applied Mechanics, December 1967 P.815)

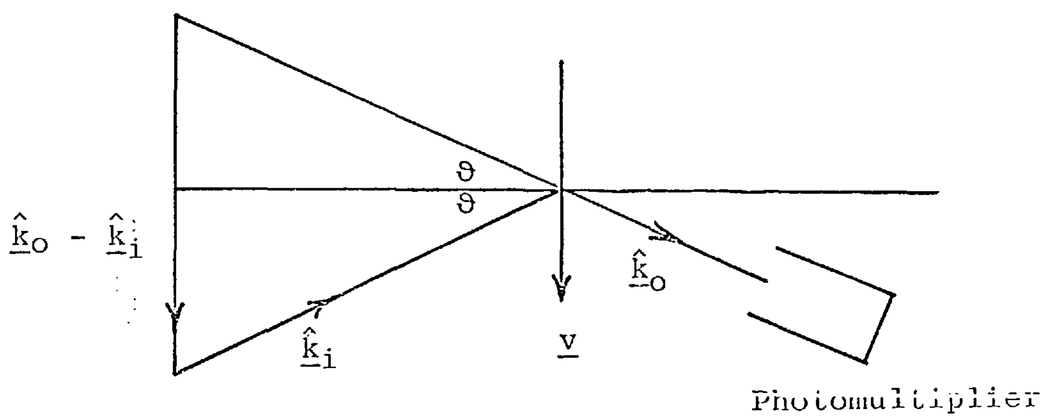

Figure 4.4 Vector diagram of the experimental setup shown in Figure 4.3

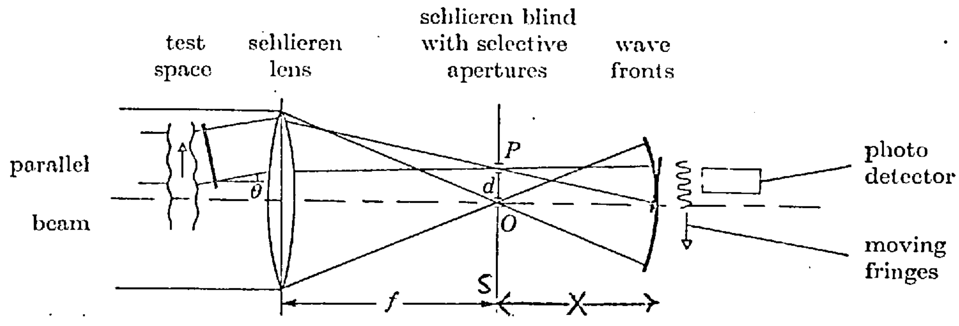

Figure 4.5 Optical arrangement used by Schwar and Weinberg for measuring velocities of phase and solid objects.

O, Optic axis; f. focal length of schlieren lens;

X, effective viewing distance from S;

ϑ, angle of deflexion.

(from Schwar and Weinberg PRSA 1969 P.470)

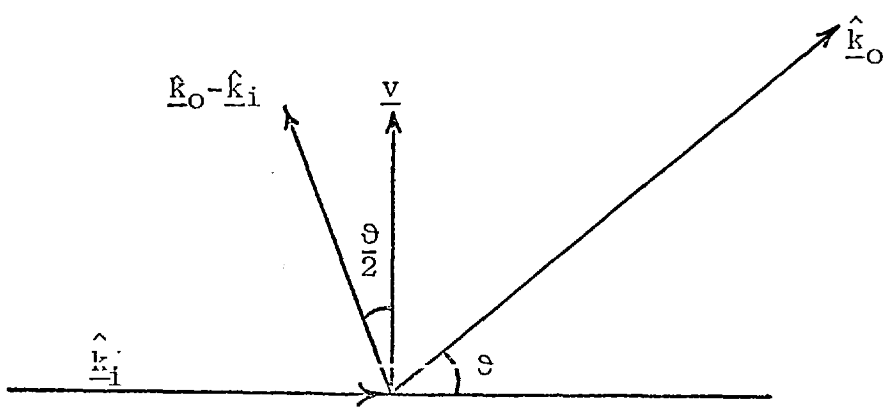

Figure 4.6 Vector diagram of the experimental setup shown in Figure 4.5

In this system, θ is small but can easily be defined accurately. Thus:

$$\nu_b = -v\theta / \lambda_i \qquad 4.2b.4$$

From equation 4.2a.5, it is clear that the recording of the Doppler shift ν_b, yields a certain component of the velocity only. The direction of this component depends on the choice of the angle between $\hat{\underline{k}}_i$ and $\hat{\underline{k}}_o$ and the direction of $\underline{v}$. In the arrangement used by Schwar and Weinberg, one measures the velocity component in the direction of the observer. In the proposed arrangement, the setup is similar to that depicted in Figure 4.5, however, the schlieren stop is designed such that it transmits rays of zero deflection and those at an angle θ in the direction perpendicular to any element of a flame front. It will be shown that this gives the local normal component velocity directly. Equation 4.2b.4 still applies in this case.

In the presence of turbulence, the instantaneous velocity v at any point may be represented by the sum of its mean value $\langle v \rangle$ and instantaneous deviation v' from the mean:

$$v = \langle v \rangle + v' \qquad 4.2b.5$$

From equation 4.2a.5, the beat frequency associated with the mean motion is :

$$< \nu_b > = (1/\lambda_i) <v> \ \hat{\underline{1}} \circ (\hat{\underline{k}}_o - \hat{\underline{k}}_i) \qquad 4.2b.6$$

$\hat{\underline{1}}$ is a unit vector in the direction of the velocity.
The beat frequency measured is :

$$\nu_b = <\nu_b> + \Delta\nu_b = (1/\lambda_i)(<v> + v') \ \hat{\underline{1}} \circ (\hat{\underline{k}}_o - \hat{\underline{k}}_i) \qquad 4.2b.7$$

and the standard deviation $<\Delta\nu_b^2>^{\frac{1}{2}}$ is given by:

$$<\Delta\nu_b^2>^{\frac{1}{2}} = \frac{<v'^2>^{\frac{1}{2}}}{\lambda_i} \hat{\underline{1}} . (\hat{\underline{k}}_o - \hat{\underline{k}}_i) \qquad 4.2b.8$$

It follows that the turbulence intensity :

$$\frac{<v'>^{\frac{1}{2}}}{<v>} = \frac{< \Delta\nu_b^2 >^{\frac{1}{2}}}{<\nu_b>} \qquad 4.2b.9$$

For the system shown in Figure 4.5, for example, the standard deviation of the beat note is given by:

$$<\Delta\nu_b^2 >^{\frac{1}{2}} = - \frac{< v'^2>^{\frac{1}{2}}}{\lambda_i} \sin\theta \qquad 4.2b.10$$

Here, θ is defined by the schlieren aperture, λ_i is known, therefore, measurement of $< \Delta\nu_b^2 >^{\frac{1}{2}}$ yields the r.m.s. deviation from the mean velocity, which is a measure of the velocity fluctuation.

4.2c Equivalence of Moving Interferogram and the Doppler Effect

In Figure 4.5, consider the case when the phase object is stationary. The interfering system is just that of the Young's modified double slit experiment. Therefore, the separation of the adjacent bright fringes is :

$$\lambda_f = X\lambda_i \;/\; d\cos\theta \qquad 4.2c.1$$

where X is the distance of the schlieren blind from the photodetector. Consider a monochromatic light source, the resulting amplitude A at the aperture of the photodetector is equal to the sum of the amplitudes originating from the two apectures P and O, i.e. :

$$A = A_1 e^{i(2\pi\nu_1 t+\phi_1)} + A_2 e^{i(2\pi\nu_2 t+\phi_2)} \qquad 4.2c.2$$

The instantaneous intensity at the detector is given by AA*, hence:

$$I = A_1^2 + A_2^2 + 2A_1A_2\cos\{\, 2\pi(\nu_1-\nu_2)t+(\phi_1-\phi_2)$$

$$4.2c.3$$

In Young's experiment, ν_1 equals ν_2 , however, when the phase object is moving, ν_2 differs from ν_1 by the Doppler frequency shift associated with the motion and the beat frequency ν_b is :

$$\nu_b = \nu_1 - \nu_2 \qquad 4.2c.4$$

From equation 4.2c.3, it is seen that the intensity I goes through a maximum whenever:

$$\cos\{\, 2\pi(\nu_1-\nu_2)t+(\phi_1-\phi_2)\,\} = 1 \qquad 4.2c.5$$

When the phase object moves with a constant speed v, the fringe pattern moves in the opposite direction with a constant speed v_f. The time interval between successive maxima as seen by the photodetector is:

$$\Delta t = 1/\ \nu_1-\nu_2 \qquad 4.2c.6$$

Consider a circular aperture of radius a, as shown in Figure 4.7 placed in front of the photodetector. The interferogram moving through it may be described by:

$$I = 2 + 2\cos\{\, k(y-Y)\,\} \qquad 4.2c.7$$

where $k = 2\pi/\lambda_i$ and Y is the centre of the fringe pattern which varies with time

$$Y = v_f\ t \qquad 4.2c.8$$

The amount transmitted through a small element $rdrd\theta$ is:

$$dI = \{\, 2+2\cos\{\, k(y-Y)\}\,\}\ rdrd\theta \qquad 4.2c.9$$

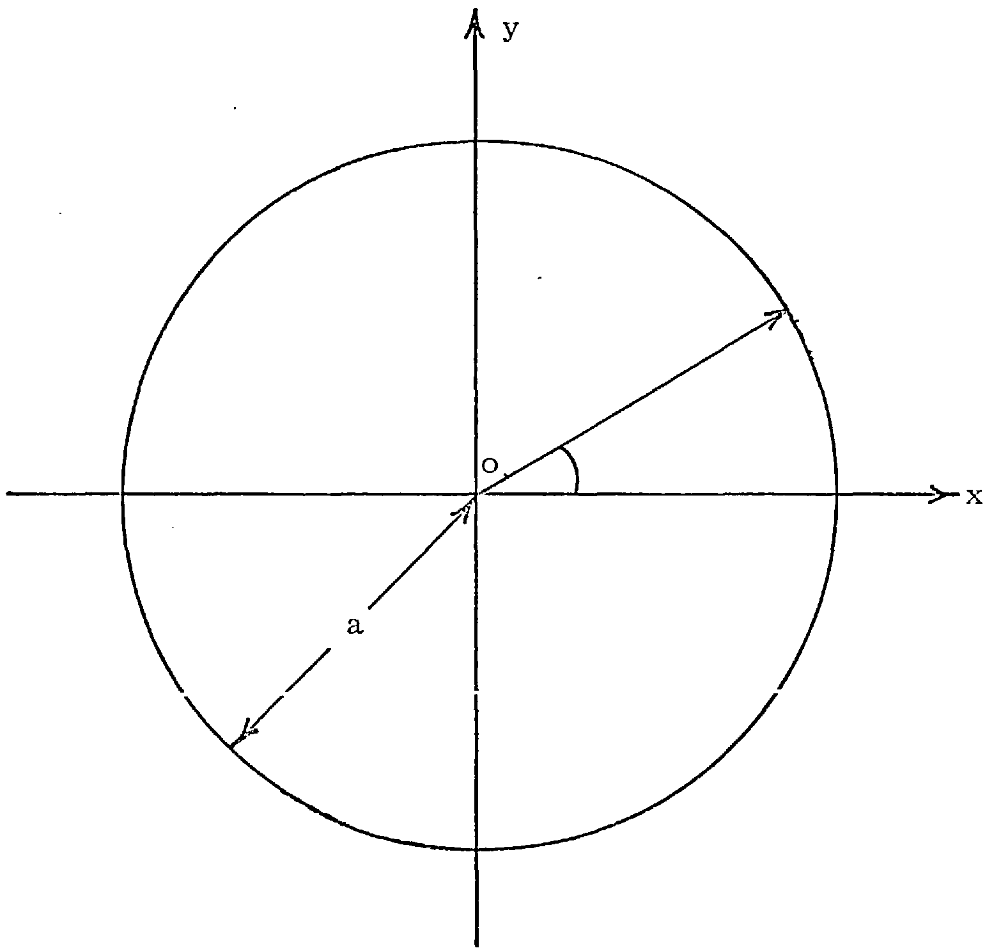

Figure 4.7 Circular photomultplier aperture of radius a, depicting coordinate system

where in circular coordinates, $y=r\sin\theta$. The total intensity transmitted through the circular aperture a is:

$$I = \int_0^{2\pi} \int_0^{a} \{ 2+2\cos\{k(r\sin\theta - Y)\}\} \, r dr d\theta \qquad 4.2c.10$$

The time variation of the intensity is :

$$\partial I / \partial t = 2 \int_0^{2\pi} \int_0^{a} \partial / \partial t \{ \cos\{ k(r\sin\theta - Y)\}\} r dr d\theta = 0 \qquad 4.2c.11$$

But

$$\int_0^{2\pi} \int_0^{a} \cos\{ k(r\sin\theta - Y)\} \, r dr d\theta$$

$$= \int_0^{2\pi} \int_0^{a} (\cos kY)\cos(kr\sin\theta) \, r dr d\theta$$

$$+ \int_0^{2\pi} \int_0^{a} (\sin kY) \sin(kr\sin\theta) \, r dr d\theta$$

$$= 2\cos kY \int_0^{\pi} \int_0^{a} \cos(kr\sin\theta) \, r dr d\theta$$

Since the cosine is an even function and the sine is an odd function, equation 4.2c.11 becomes:

$$\partial I/\partial t = -4k\sin kY(dY/dt) \int_0^{\pi} \int_0^{a} \cos(kr\sin\theta) \, r dr d\theta$$

or

$$\partial I/\partial t = -4kv_f \sin kY \int_0^{\pi} \int_0^{a} \cos(kr\sin\theta) \, r dr d\theta \qquad 4.2c.12$$

This is cyclic with period $Y=\lambda_f$

or

$$v_f \Delta t = \lambda_f \qquad 4.2c.13$$

i.e.

$$\Delta t = \lambda_f / v_f$$

Since in this arrangement, the reference source O falls on the optic axis, the fringe velocity v_f is given by:

$$v_f = Mv \qquad 4.2c.14$$

where M is the magnification of the system. By applying the lens equation (M=1-(v/f)) it immediately follows that:

$$M = -X/f \qquad 4.2c.15$$

Combining equations 4.2c.1, 4.2c.6, 4.2c.13, 4.2c.14 and 4.2c.15, we have:

$$\Delta t = \frac{X \lambda_i}{d\cos\theta} \quad X \quad \frac{1}{-(X/f)v} = -\lambda_i / v\sin\theta \qquad 4.2c.16$$

Therefore, from equation 4.2c.4:

$$\nu_b = -(v/\lambda_i) \sin\theta \qquad 4.2c.17$$

which is exactly the same as equation 4.2b.3 obtained from the general Doppler beat frequency equation.

4.3 Theoretical Aspects in the Design of Doppler Interferometers.

A Doppler interferometer consists essentially of a light source, schlieren lenses (or mirrors), a schlieren blind, a photodetector and a frequency metering device. In this section, the requirements of each component for optimum design are investigated.

4.3 Light Source

Figure 4.8 is a schematic diagram of the simplest form of Doppler interferometer. Consider the case where the wave field is produced by an extended source S and the phase structure of the test object remains unchanged during the time of measurement. For simplicity we assume that the light is linearly polarized and the medium between the two screens has refractive index of unity. Light variations from the two apertures $P_1(\underline{r}_1)$ and $P_2(\underline{r}_2)$ of the schleren blind Σ interfere at the point $P(\underline{r})$ on the screen Σ' and is detected by a photodetector. We may regard P_1 and P_2 as centres of secondary disturbances, so that the complex disturbance at P is given by (15):

$$V(\underline{r},t) = K_1 V(\underline{r}_1, t-t_1) + K_2 V(r_2, t-t_2) \qquad 4.3a.1$$

where $t_1 = d_1/c$ and $t_2 = d_2/c$. K_1 and K_2 are propagators

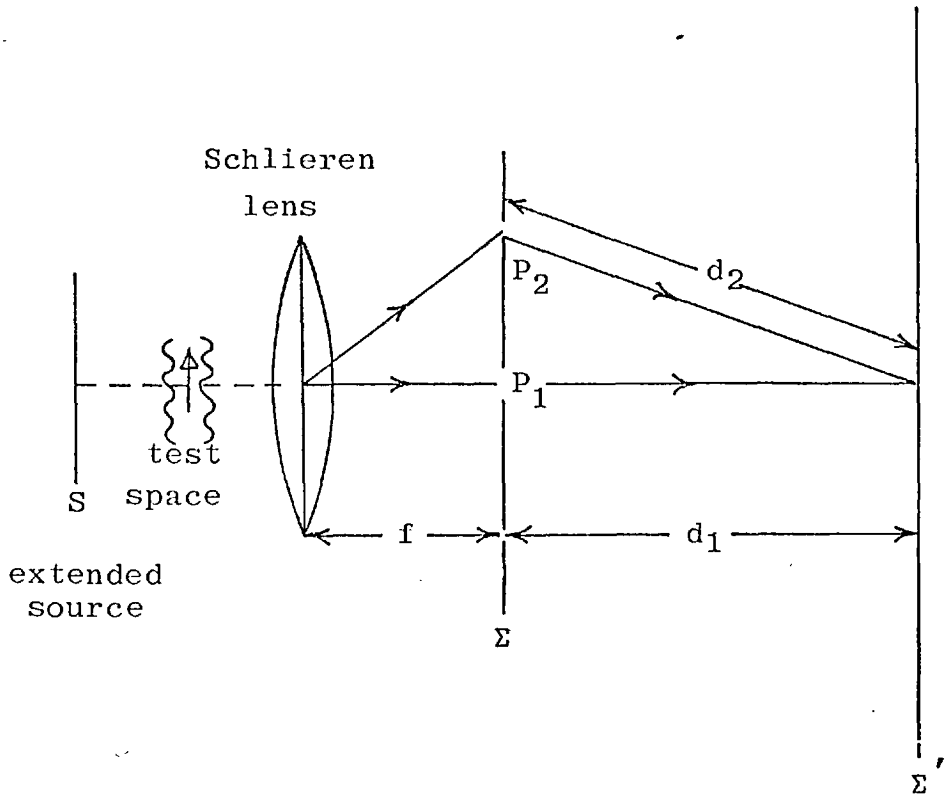

Figure 4.8 Schematic diagram of the simplest form of Doppler interferometer

between P_1 and P and between P_2 and P respectively.

The instantaneous intensity at $P(\underline{r})$ is:

$$I(\underline{r},t) = |K_1|^2 I(\underline{r}_1,t-t_1)+|K_2|^2 I(r_2,t-t_2)$$

$$+2\mathrm{Re}\{ K_1^* K_2 V^*(\underline{r}_1,t-t_1)V(\underline{r}_2,t-t_2) \} \qquad 4.3a.2$$

It follows that for stationary and ergodic fields, the average intensity of light at P is:

$$\langle I(\underline{r},t)\rangle = |K_1|^2 \langle I(\underline{r}_1,t)\rangle + |K_2|^2 \langle I(\underline{r}_2,t)\rangle$$

$$+2 |K_1 K_2| \mathrm{Re}\langle V^*(\underline{r}_1,t-t_1)V(\underline{r}_2,t-t_2)\rangle \qquad 4.3a.3$$

The quantity $\langle V^*(\underline{r}_1,t-t_1)V(\underline{r}_2,t-t_2)\rangle$ is just the mutual coherence function $\Gamma_{12}(\tau)$ (15), where $\tau_n=t_n-t_1$. Thus, equation 4.3a.3 may be written:

$$\langle I(\underline{r},t)\rangle = |K_1|^2 \langle I(\underline{r}_1,t)\rangle+|K_2|^2 \langle I(\underline{r}_2,t)\rangle +2| K_1K_2|\Gamma_{12}^{(r)}(\tau)$$

4.3a.4

where $\Gamma_{12}^{(r)}(\tau)$ is the real part of $\Gamma_{12}(\tau)$. We normalize $\Gamma_{12}(\tau)$ by defining the quantity:

$$\gamma_{12}(\tau) = \Gamma_{12}(\tau) / \{ (\Gamma_{11}(0))^{\frac{1}{2}}(\Gamma_{22}(0))^{\frac{1}{2}} \}$$

$$= \Gamma_{12}(\tau) /\{ (\langle I(\underline{r}_1)\rangle)^{\frac{1}{2}}(\langle I(\underline{r}_2)\rangle)^{\frac{1}{2}} \}$$

4.3a.5

$\gamma_{12}(\tau)$ is called the complex degree of coherence of the vibrations. Equation 4.4a.4 then becomes :

$$<I(\underline{r},t)> = <I^{(1)}(\underline{r},t)> + <I^{(2)}(\underline{r},t)>$$

$$+2 \{<I^{(1)}(\underline{r},t)>\}^{\frac{1}{2}} \{ <I^{(2)}(\underline{r},t)>\}^{\frac{1}{2}} \gamma_{12}^{(r)}(\tau)$$

4.3a.6

where $<I^{(1)}(\underline{r},t)>$ represents the average intensity of light reaching the point $P(\underline{r})$ through the aperture P_1 only, and $< I^{(2)}(\underline{r},t)>$ has a similar interpretation. γ_{12} may be written:

$$\gamma_{12}(\tau) = |\gamma_{12}(\tau)| \exp i\{ \alpha_{12}(\tau)-2\pi\bar{\nu}\tau \} \qquad 4.3a.7$$

where $\bar{\nu}$ is the mean frequency of the light and

$$\alpha_{12}(\tau) = 2\pi \bar{\nu}\tau + \arg \gamma_{12}(\tau) \qquad 4.3a.8$$

Then equation 4.3a.6 becomes:

$$<I(\underline{r},t)> = <I^{(1)}(\underline{r},t)> + <I^{(2)}(\underline{r},t)>$$

$$+2\{ <I^{(1)}(\underline{r},t)>\}^{\frac{1}{2}}\{<I^{(2)}(\underline{r},t)>\}^{\frac{1}{2}}| \gamma_{12}(\tau)|\cos\{\alpha_{12}(\tau)-\delta\}$$

4.3a.9

where $\delta = 2\pi\bar{\nu}\tau$. According to an inequality after Schwartz, it can be shown that:

$$|\gamma_{12}(\tau)| \leq 1 \qquad 4.3a.10$$

We see that if $|\gamma_{12}(\tau)|$ has the extreme value unity, the intensity at P is the same as would be obtained with strictly monochromatic light of wavelength $\bar{\lambda}$, and with the phase difference between the vibrations at $P_1$and P_2 equals $\alpha_{12}(\tau)$ (c.f. equation 4.2c.3).

The visibility of the fringes as defined by Michelson (41) may be written:

$$\mathcal{V}(\underline{r}) = 2\frac{\{<I^{(1)}(\underline{r},t)>\}^{\frac{1}{2}}\{<I^{(2)}(\underline{r},t)>\}^{\frac{1}{2}}}{<I^{(1)}(\underline{r},t)> + <I^{(2)}(\underline{r},t)>}|\gamma_{12}(\tau)| \qquad 4.3a.11$$

Therefore, to obtain sharp fringes, our source should ideally yield a unit value of $|\gamma_{12}(\tau)|$.

The function $\gamma_{12}(\tau)$ embodies both temporal and spatial coherence. Temperal coherence of the light source, which is measured by the autocorrelation function $\gamma_{11}(\tau)$ is important in that it must be capable of forming a sufficient number of fringes for accurate measurement of ν_b. The optical path difference between the test and reference beams must always be kept less than the temporal coherence of the source.

It is seen that the choice of the source is dependent upon the number of fringes required. Suppose that for a desired degree of accuracy, the conditions of our system require a minimum of 50 fringes. For a line source, from equation 4.3a.11, it can be shown that the fringes will be visible up to an order of interference (42):

$$p = \lambda_i/\Delta\lambda \qquad 4.3a.12$$

For λ_i=5000 Å, say:

$$\Delta\lambda = 100 \text{ Å}$$

and the temporal coherence of the source must not be less than 0.05 mm. For a source with spectral distribution characterized by a Gaussian function, the corresponding expression to equation 4.3a.12 is:

$$p = (2.96/\pi)\ \lambda_i/\Delta\lambda \qquad 4.3a.13$$

so that the spectral width of the sources must not be greater than 94.3 Å.

The requirement of spatial coherence in the design of Doppler velocimeters is minimal, because of the point to point correspondence between the test and reference beams and because of the facility of being able to arrange for zero optical path difference between the two beams.

It is clear then, that conventional thermal sources can be used for Doppler interferometry. However, due to the inherent problem of alignment in conventional interferometry, and that the requirement of small schlieren aperture for accurate definition of θ , the low power output of thermal sources is a distinct disadvantage. This is more evident when we consider the ready availability of gas lasers with vastly superior properties (32).

4.3b Schlieren Lenses (or Mirrors)

The choice of focal lengths of the schlieren lenses or mirrors is important in the design of Doppler interferometers, since it has the following three areas of influence :

1. The magnification of the system is inversely proportional to the focal length (c.f. equation 4.2c.14).
2. The angle of deflection θ is given by:

$$\theta = d/f \qquad 4.3b.1$$

where d is the distance between schlieren apectures.

3. Since $\theta = d/f$

$$\delta\theta = \delta d / \delta f \qquad 4.3b.2$$

With reference to equation 4.3b.4, it is seen that the error in the focal length will directly affect the accuracy of the measured value of ν_b and hence the velocity.

It is seen that the choice of f will depend upon the required sensitivity and that f must be specified as accurately as possible.

4.3c Schlieren Blind

The schlieren blind is probably the most important component of Doppler interferometers. It is the variability in its design which offers such a great possibility for velocity measurements using the Doppler interferometric technique. The design of the schlieren blind for the proposed Doppler interferometer will be fully discussed in section 4.4.

When devising a suitable schlieren blind, one must consider the following:

1. With reference to equation 4.3b.2, it is clear that for an accurate definition of θ , the linear dimension s, (or diameter in the case of two aperture design) of the selective aperture must be very much smaller than d.
2. When s is small, diffraction is important and the number of fringes formed is given by (assuming a coherent light source is used):

$$N = 2nd/s \qquad 4.3c.1$$

Therefore, for large values of N, s must be made very much smaller than d.

Beats can be observed only while the object is still within the transluminating beam. Therefore, the number of beats will depend on the width of the beam. The minimum beam width required to detect N beats is given by:

$$\omega_m = \nu(N/\nu_b) \qquad 4.3c.2$$

By making use of equation 4.2b.4, we have:

$$\omega_m = \frac{\lambda_i}{\theta} N$$

For the purpose of increasing N, it is clear that there is no point in making s so small that the value of N, as expressed in equation 4.3c.1, is greater than $\omega_m\theta/\lambda_i$. However, the smaller we make s the more accurately θ can be defined.

Doubling N will increase the accuracy of ν_b two fold. However, the fringe intensity will be decreased by a factor of 16. Therefore, the intensity of light source or the sensitivity of the photodetector or both must be correspondingly increased.

3. The best visibility of the fringes is achieved when:

$$\langle I^{(1)}(\underline{r},t)\rangle = \langle I^{(2)}(\underline{r},t)\rangle \quad \text{(from equation 4.3a.11).}$$

Since in most cases the intensity of the reference beam is much higher, a device must be included in the reference aperture to reduce its intensity. Preferably, it should be arranged so that the reference intensity can be varied continuously in order to accommodate different test objects.

4. From equation 4.3b.1, it can be seen that for a desired value of θ, d must be slected in conjunction with f.

4.3d Photodetector

Clearly the response time of the photodetector must be less than $1/\nu_b$. Consider the velocity of shock waves, take a unit mass of gas in front of a wave having a volume v_1 and pressure P_1 before, and v_2 and P_2 after compression. For $P_2/P_1 = 1000$ and $v_1/v_2 = 14.3$, the velocity of the shock wave is of the order of $10^4 m.s^{-1}$. The beat frequency as given by equation 4.2b.4 is :

$$\nu_b = 2 \times 10^7 \text{ Hz}.$$

where $\theta = 10^{-3}$ Rd. and $\lambda_i = 5000$ Å. Therefore, the response time of the detector must be at least 50 ns. Similarly, for the measurements of burning velocities, the required response time of the detector is of the order of 50 ms.

Another requirement of the photodetector is that it must be sufficiently sensitive. This is evident from the foregoing discussions concerning the determination of the optimum aperture size for the schlieren blind. The sensitivity required will, of course, be dependent upon the available power of the light source.

4.3e Frequency Metering Device

Beat frequency measurements can be done in three ways:

1. An electronic timer can be used to measure the time interval for a preset number of beats. This method is feasible because from the optical system, the number of beats can be estimated.
2. An electronic timer can be used to count the number of beats in a preset time interval. This method is not recommended unless an idea of the beat frequency expected is known, or that a continuous train of beats is being investigated.
3. The most convenient method is to display and photograph the beat signal using an oscilloscope.

4.4 A New Doppler Interferometer For The Direct Measurement Of Normal Propagation Velocities Of Phase Objects

In order to measure orthogonal velocities using interference fringes as markers and the frequency beat as a clock, we require that a small aperture be traversed by interference fringes locally parallel to surfaces of equal density, but whose spacing is constant, independently of that density field. This can be achieved by using the phase object as the beam splitter, with some other optical component defining the angle between the two interfering wave fronts. This section describes a new Doppler interferometer which is designed to accomplish this aim. This Doppler interferometer will measure directly the orthogonal

/

propagation velocities of phase objects with respect to a stationary observer as well as with respect to the approach stream.

4.4a The Schlieren Blind

A schlieren blind shaped as shown in Figure 4.9 will act as a double aperture transmitting rays of zero deflection and those at an angle r/f in the direction perpendicular to any element of a flame front. It will therefore produce fringes of constant spacing everywhere parallel to that section of the flame which is tangential to the light beam.

In practice the transparent ring of the schlieren blind was varied in diameter between 5.8 and 20 mm., depending on the dimensions of the polar diagram of deflections corresponding to each particular object. Its central aperture was provided with a small square of polaroid so that by its rotation, the relative intensity of the undeflected- with respect to the deflected- beam could readily be adjusted for maximum visibility of fringes in each case.

A photodetector covered by an aperture A, smaller than the fringe spacing, q, yielded a signal giving the orthogonal velocity, s, of the front directly, irrespective of its velocity, V. This can be seen from Figure 4.10. Suppose the set of fringes moves along the $\hat{\underline{k}}_1$ direction with a speed V. The small detector, A, would record a time t_1

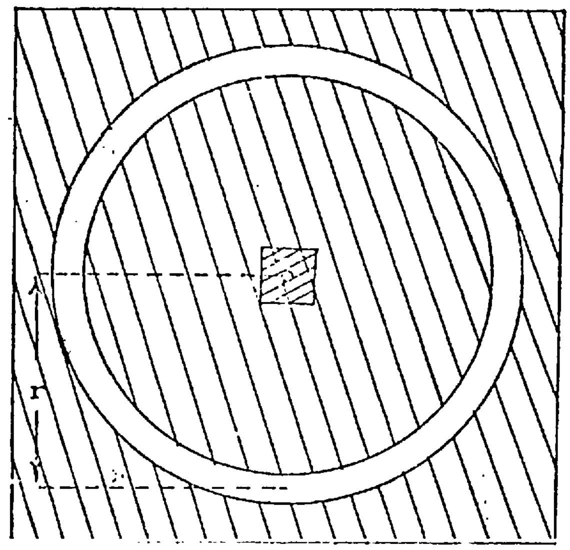

Figure 4.9 The Schlieren blind
(The shaded area is opaque while the cross-shaded area represents a piece of polaroid)

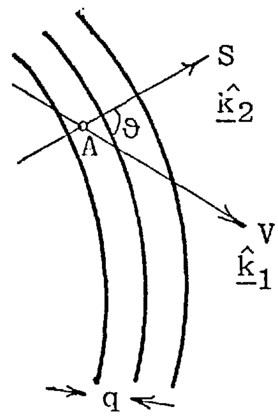

Figure 4.10 Fringe system moving across a small entrance aperture of a photomultiplier

between the passage of the fringes, where:

$$t_1 = V/q\sec\theta \qquad 4.4a.1$$

The orthogonal direction is represented by the unit vector $\hat{\underline{k}}_2$. To measure the normal velocity s, one would measure the time t_2 between the passage of the fringes travelling in the $\hat{\underline{k}}_2$ direction, where:

$$t_2 = s/q \qquad 4.4a.2$$

but $$s = V\cos\theta \qquad 4.4a.3$$

Therefore,

$$t_1 = t_2 \qquad 4.4a.4$$

The velocity is with respect to a stationary observer. To measure velocities with respect to the approach stream (burning velocity is defined with respect to the cold gas), it is customary to track small particles included in the gas. Unlike phenomena such as premixed flames, small particles do not deflect light in one direction, but diffract or scatter it symmetrically. With this design of the schlieren blind, they are displayed as concentric fringes, again of the same spacing.

The way such fringes interact with those due to a flame is shown in Figure 4.11. The photodetector covered by an aperture appreciably larger than each fringe system

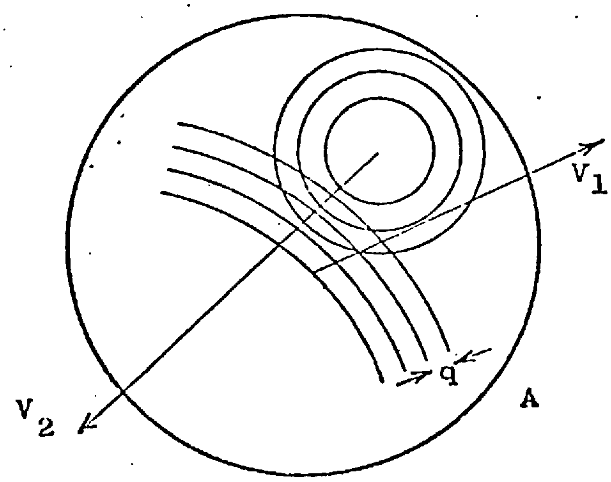

Figure 4.11 Moving fringe systems due to a particle and a flame interacting within the entrance aperture of a photomultiplier

will now respond by a periodic signal to two light grids (of equal spacing, where they are parallel) passing over one another. Consider a set of moving straight line fringes due to a flame traversing a set of stationary concentric fringes produced by a small particle. Following the approach given in section 4.2c, the total intensity at the photodetector aperture is:

$$I = 4+2\cos k_1 r + 2\cos \{ k_2(y-Y) \} \qquad 4.4a.5$$

where $k_1=2\pi/\lambda_1$, λ_1 being the spacing of the circular fringes and $k_2=2\pi/\lambda_2$, λ_2 being the spacing of the straight fringes. The amount transmitted through a small element $rdrd\theta$ is :

$$dI = \{ 4 + 2\cos k_1 r + 2\cos\{ k_2(r\sin\theta-Y)\}\} \quad rdrd\theta$$

4.4a.6

Therefore, the total intensity transmitted through a circular aperture of radius a is:

$$I = \int_0^{2\pi}\int_0^{a} \{ 4+2\cos k_1 r + 2\cos\{ k_2(r\sin\theta-Y)\}\} \quad rdrd\theta$$

4.4a.7

We are concerned with time variation, so we look at:

$$\partial I/ \partial t =2 \int_0^{2\pi}\int_0^{a} \partial/\partial t \{ \cos\{ k_2(r\sin\theta-Y)\} \} rdrd\theta$$

4.4a.8

Equations 4.4a.8 and 4.2c.11 are exactly the same. It follows that the frequency is:

$$f = V_f / \lambda_2 \qquad 4.4a.9$$

Since similar treatment will apply when the circular fringes are moving or when both sets of fringes are non-stationary, it is seen that the velocity deduced will be the component of the gas flow perpendicular to the front it is entering- whether the front, the particle or both are moving. Only that component of the circular fringes which is parallel to the flame corresponds to the A.C. signal - the perpendicular component generates a D.C. signal which is filtered out.

4.4b <u>The Detector Aperture</u>

If the photodetector is to record the motion of a single fringe pattern, it is clear that its entrance aperture should be less than the fringe spacing. The intensity transmitted through a circular aperture of diameter a is from equation 4.2c.10:

$$I = \int_0^{2\pi}\int_0^{a} \{ 2 + 2\cos\{ k(r\sin\theta - Y)\} \} \, r\,dr\,d\theta$$

$$= 2\pi a^2 + 4\pi a^2 \cos kY \frac{J_1(ka)}{ka}$$

$$= 2\pi a^2 \{ 1 + 2\cos kY \frac{J_1(ka)}{ka} \} \qquad 4.4b.1$$

where J_1 denotes the Bessel function of the first kind of order one. Therefore, the visibility of the fringes is:

$$\mathcal{V} = \left| \frac{2J_1(ka)}{ka} \right| \qquad 4.4b.2$$

When the diameter of the aperture is half the fringe spacing:

$$\mathcal{V} = \left| \frac{2J_1(\pi)}{\pi} \right| \simeq 0.1 \qquad 4.4b.3$$

which is much higher than the minimum perceptible by the eye ($\mathcal{V} \simeq 0.02$) and certainly above the limiting contrast detectable by a photomultiplier.

In the case of interacting fringes (Figure 4.11), the size of the aperture should always exceed the sum of the widths of the two interacting fringe pattern, for the following reason, If both the flame front and the particles are moving, the system can produce three frequencies : those due to each of the fringe patterns interacting with the edges of the aperture and those due to their interaction with each other. The former are also produced when a small aperture is used (Figure 4.10); the latter is not. If the aperture is larger than the two fringe systems together, the required signal is easily picked out by its length. The events of interest then produce trains of more pulses than the number of fringes in each pattern.

The upper limit to the aperture size is set in association with the density of the particle cloud. Too large an aperture may intercept fringe patterns due to more than one particle at a time. This is apart from the limit eventually set by saturating the photo-detector with steady illumination to the point where the D.C. signal can no longer be completely filtered out and the visibility of the A.C. signal falls.

A limiting value of visibility $\mathcal{V}_1$ for photo-multipliers can be easily estimated. Thus :

From equation 4.3a.11:

$$\mathcal{V} = \frac{I_{max} - I_{min}}{I_{max} + I_{min}} \qquad 4.4b.4$$

The limiting value of $\mathcal{V}$ is when:

$$I_{max} - I_{min} = I_N \qquad 4.4b.5$$

Where I_N represent the noise level of the photomultplier. Suppose the lowest intensity of light likely to be encountered in the experiment is such as to produce a photoelectric current of 10^{-1} μA. In this case, the signal, S, to noise, N, ratio for photomultipliers operated on D.C. is of the order of:

$$S/N \simeq 80 \text{ dB} \qquad 4.4b.6$$

or

$$10^{-1}/N \simeq 10^{4}$$

i.e. $N \simeq 10^{-5}$

Therefore:

$$\mathcal{V}_1 \simeq 5X10^{-5} \qquad 4.4b.7$$

The visibility of the interacting fringes can be calculated from equation 4.4a.7. After evaluating the integrals this equation becomes:

$$I = 4\pi a^2 + 4\pi/k_1\{ a \sin k_1 a + (1/k_1)(\cos k_1 a-1) \}$$

$$+ 4\pi a^2 \cos k_2 Y \frac{J_1(k_2 a)}{k_2 a}$$

i.e. the visibility is:

$$\mathcal{V} = \left| \frac{\dfrac{J_1(k_2 a)}{k_2 a}}{1 + \dfrac{\sin k_1 a}{k_1 a} + \dfrac{\cos k_1 a-1}{(k_1 a)^2}} \right| \qquad 4.4b.9$$

In this system, $k_1 = k_2$, so when $a=n$ where n is a positive integer, equation 4.4b.9 becomes:

$$\mathcal{V} = \left| \frac{J_1(2\pi n)}{2\pi n} \right| \qquad 4.4b.10$$

Figure 4,12 shows the variation of $\mathcal{V}$ with n, it is seen that even when n=10, the visibility is still more than an order of magnitude larger than $\mathcal{V}_1$ (equation 4.4b.7).

4.4c The Complete System

Figure 4.13 is a schematic diagram of the proposed Doppler interferometer. The light source W used was the argon ion laser as described in Chapter 3. For Doppler interferometry, this is an ideal light source (section 4.3a). The wavelength of 5145 Å was selected because the output power can be as high as one watt CW, which was more than sufficient for the experimental purposes. The function of L_1 and F are the same as that delineated for the large area interferometer (Chapter 3). M_1 and M_2 are schlieren mirrors, each having a focal length of 240 cm.±1%. The phase object, T, was used as the beam splitter. The schlieren blind, B, was made in two ways. The first method was to make a proportionally magnified version by cutting the desired segments using black paper and gluing them on a white board. This was then reduced photographically to the required size and processed as a positive on a

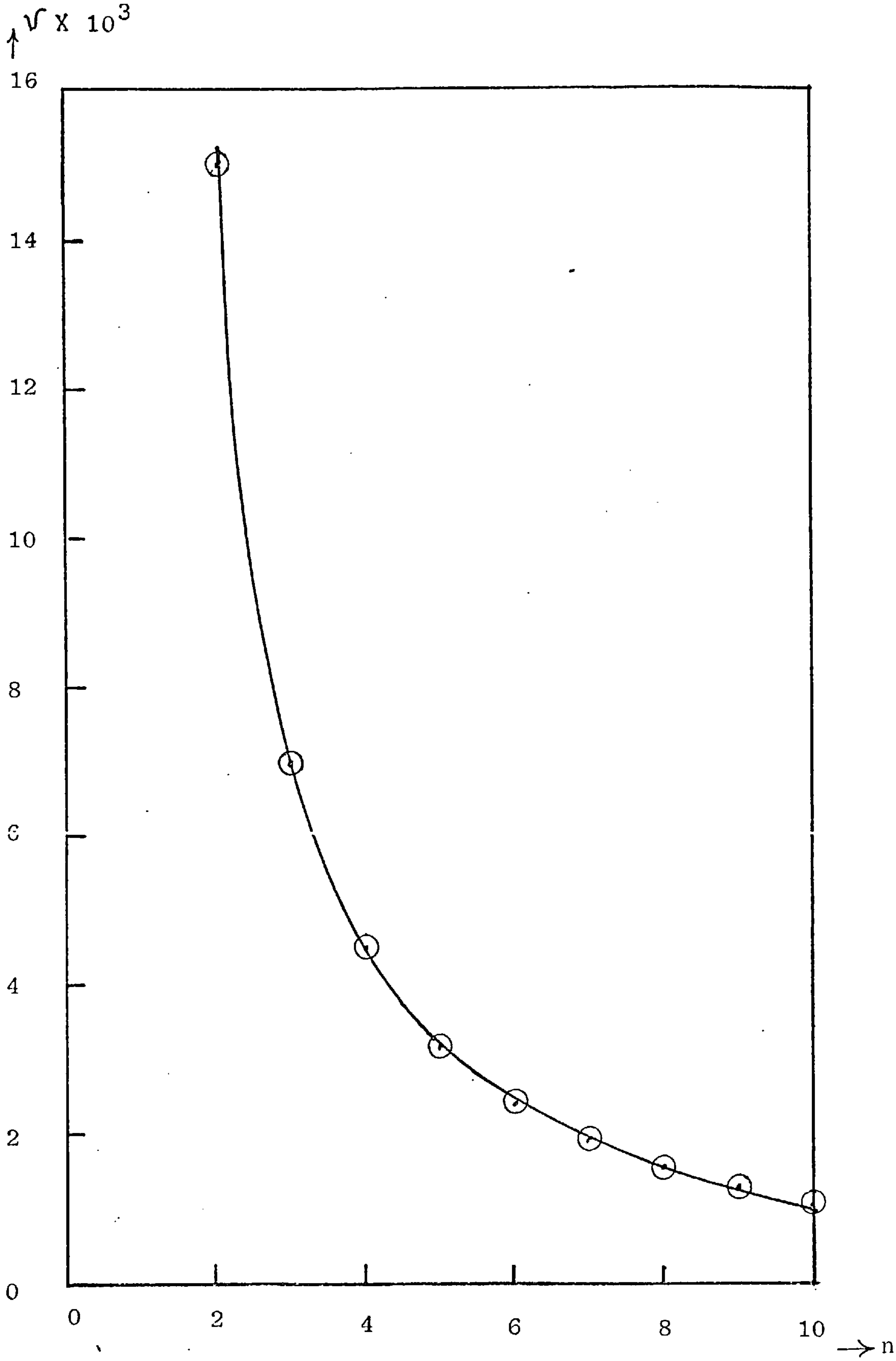

Figure 4.12 Theoretical plot of ν versus n. $\nu = \left| \frac{J_1(2\pi n)}{2\pi n} \right|$

For $n \geqslant 3$, the approximation $J_1(z) = \sqrt{(2/\pi z)}\ \cos(z - 3\pi/4)$

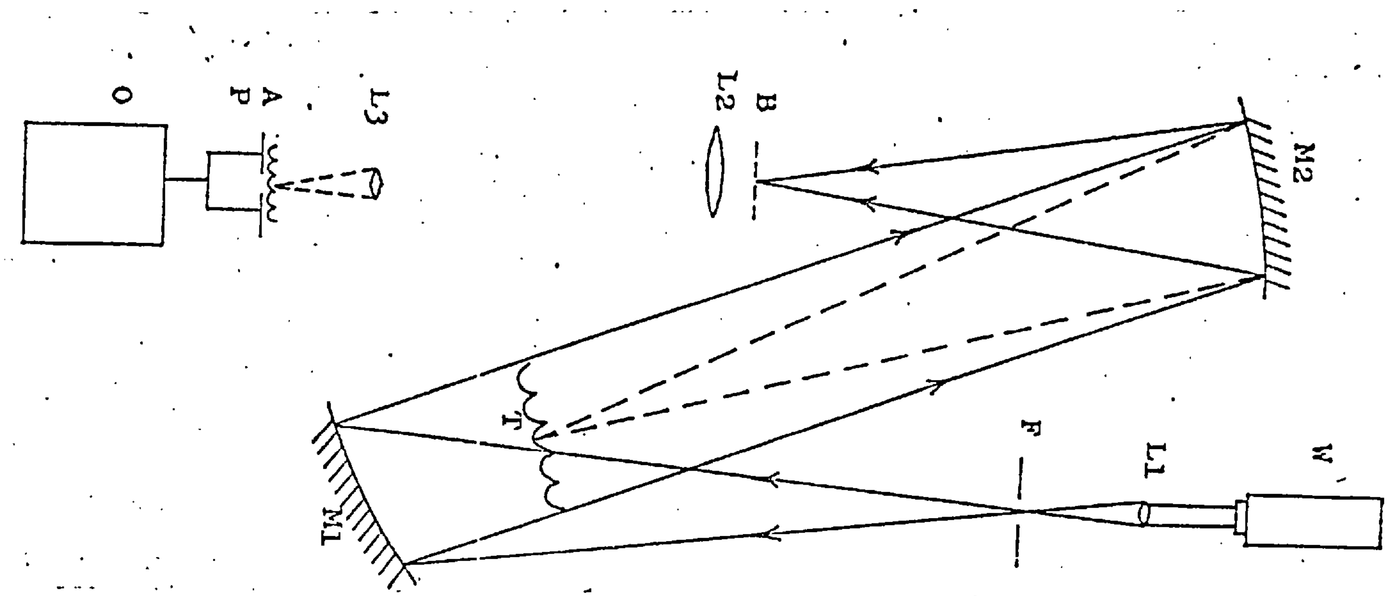

Figure 4.13 Optical system of the Doppler interferometer
(plan view: not to scale)
W - argon ion laser ; Li - microscope objective (X10);
F - pinhole filter ; M_1 & M_2 - Schlieren mirrors of focal length, f, 240 cm;
T - test object ; B - Schlieren blind (see Figure 4.9);
L_2 - convex lens of focal length 5.0 cm. ; L_3 - convex lens of focal length 4.5 cm. ; A - photomultiplier entrance apecture (variable diameter) ; P - photomultiplier ; O - oscilloscope

photographic plate. To obtain high density, Ilford Formolith plates were processed by Formolith liquid developer. The resulting opaque ring of the schlieren blind had an opacity of 10^6. The transparent part should ideally be optically flat so as to give no spurious fringes resulting from laser beams having slightly different optical path lengths through the glass slab. The second technique was to make the schlieren blind mechanically. Drills down to a diameter of 0.1 mm. were available, the various components of the blind were carefully machined from a sheet of copper foil which was first painted black. Finally these components were mounted on a fire-polished glass slide. The lenses L_2 and L_3 were used as a telescopic system which enlarged the fringe pattern to any desired size suitable for the detector. The detector aperture, A, was of variable diameter to suit different experimental requirements (section 4.4b). The frequency metering device employed was a Telequipment oscilloscope with an attached camera, the beat frequency was calculated from the photographs of the scope traces.

When measuring the velocity of a phase object with respect to the approach stream (Figure 4.11), the beat frequency is constant if velocities do not vary with time. However, due to the heating and expansion of the gas as it enters a flame front, the particles will accelerate and the peaks on the oscilloscope display will then compress with time. Although the trace correctly represents local velocity (and might thus be used for measuring density profiles) burning velocity is defined with respect to the cold unburnt gas. To obtain accurate burning velocities. Therefore, the range of measured frequencies should be extrapolated to the lowest value.

4.5 Orthogonal Velocity Measurements

The Doppler interferometer described in section 4.4 was tested on a number of practical systems relevant to combustion. It was demonstrated that the method may be successfully applied to moving solid objects such as moving diffraction gratings and particles, as well as to phase objects whether moving or stationary in the form of flames stabilized on a burner and propagating in a tube.

4.5a Velocity Measurement of a Rotating Diffraction Grating

In this and all subsequent experiments, the apparatus shown in Figure 4.13 was used. The object whose velocity was being measured was a 5 cm. square grating attached to a rotating arm of a motor, This grating had 7 lines per mm. and the length of the rotating arm was 50 cm.

The grating provided the most basic test of the method, since it gave rise to uniform deflection across its width and its velocity could be accurately controlled. In considering it as a "phase object", it differs from a flame in that at any one point it deflects light in more than one direction (because it has several diffraction orders) but, unlike a particle, its polar diagram (Figure 4.14a) lies along a straight line-i.e. does not manifest circular symmetry about a pole. The diameter of the ring in the schlieren aperture was such as to allow the +1 and -1 diffraction orders to pass through the blind, in addition to the undeflected beam.

Suppose the central beam and the beams emerging from the two parts of the ring corresponding to the +1 and -1 orders interfere at a point P in the observation phane. Denote their respective complex amplitude by ϕ_o, ϕ_{+1} and ϕ_{-1} (Figure 4.14b). The complex amplitude ψ at P is given by:

$$\psi = \phi_o + \phi_{+1} + \phi_{-1} \tag{4.5a.1}$$

where

$$\phi_o = a_o e^{-i\delta_o}$$

$$\phi_{+1} = a_{+1} e^{-i\delta_{+1}} \tag{4.5a.2}$$

$$\phi_{-1} = a_{-1} e^{-i\delta_{-1}}$$

and the intensity at P is:

$$I_P = a_0^2 + a_{+1}^2 + a_{-1}^2 + 2a_o a_{+1} \cos(\delta_o - \delta_{+1}) + 2a_{+1} a_{-1} \cos(\delta_{-1} - \delta_{+1})$$

$$+ 2a_o a_{-1} \cos(\delta_{-1} - \delta_o) \tag{4.5a.3}$$

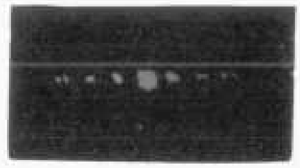

Figure 4.14a
Polar diagram of deflections
due to a diffraction grating

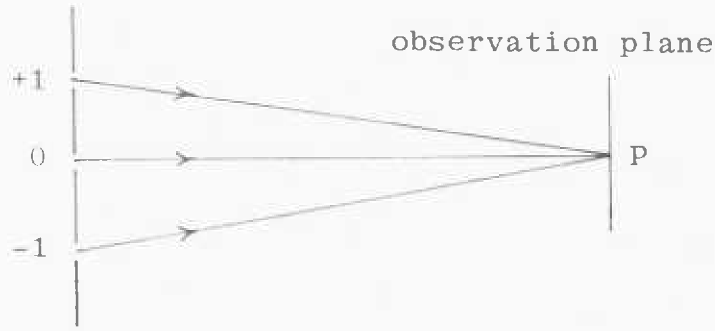

Figure 4.14b Interference of 0, +1 and -1 diffraction orders at a point P in the observation plane

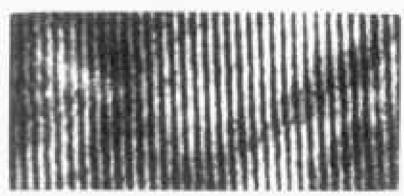

Figure 4.14c Fringe pattern produced by diffraction grating

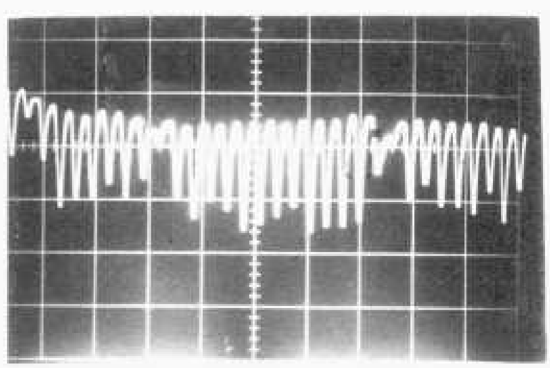

Figure 4.14d Oscillogram traces of Doppler beat frequency signal produced by a rotating diffraction grating as the fringe pattern (Figure 4.14c) moves across the photomultiplier

but

$$\cos(\delta_o - \delta_{+1}) = \cos(\delta_{-1} - \delta_o)$$

$$\cos(\delta_{-1} - \delta_{+1}) = \cos 2(\delta_o - \delta_{+1}) \qquad 4.5a.4$$

and $$a_{+1} = a_{-1}$$

Therefore:

$$I_P = 2a_{+1}^2 + a_o^2 + 2a_{+1}^2 \cos 2(\delta_o - \delta_{+1}) + 4a_{+1}a_o \cos(\delta_o - \delta_{+1})$$

4.5a.5

when:

$$2a_{+1}^2 + a_o^2 = 4a_{+1}a_o$$

$$a_o \simeq 3.4a_{+1} \qquad 4.5a.6$$

Then the fringe system produced by interference between the zero and ± 1 orders has maximum visibility. Direct interference between +1 and -1 orders (whose fringe spacing is half that between the zero and ± 1 orders) then produces only an imperceptible ripple on the main fringe pattern. This explains why, in practice, only the main fringe spacing is ever observed. To detect fringe motion, the entrance aperture of the photodetector should be less than the fringe spacing. An aperture whose diameter is larger than the fringe spacing of one set of fringes yet smaller than that of the other set, will only record the motion of the latter set.

The value of r (Figure 4.9) was 2.4 mm. and the diameter of the central aperture was 0.1 mm. The fringe pattern moving across a 0.4 mm. wide aperture over the photomultiplier is shown in Figure 4.14c and the resulting oscilloscope record in Figure 4.14d.

From equation 4.2b.4, substituting $\theta=10^{-3}$Rd ±1% (error due to the finite width of the circular slit tends to average out but the 1% uncertainty in the focal length of the schlieren mirror is absolute); $\lambda_i=5145$ Å; $\nu_b=6.74\times10^{3}$Hz ±0.6% (assuming that the turning point of an oscillation could be determined to tenth of a cycle). The linear velocity v is 3.47 m s^{-1} ± 1.6% and the corresponding angular velocity is 6.94 Rd/sec ±1.6%, which was in excellent agreement with the rated speed of the motor.

4.5b Velocity Measurements of a Burner Flame

A coal gas diffusion flame stabilized on a "bats' wing " burner was moved across the test space by hand. The parameters of the apparatus used were the same as that of section 4.5a. Figures 4.15a and b show the polar deflection diagram at the schlieren blind and the fringe pattern at the photomultiplier produced by the flame. This is a complex phenomenon ; the major lobes

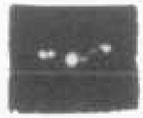

Figure 4.15a Polar deflection diagram due to a flame

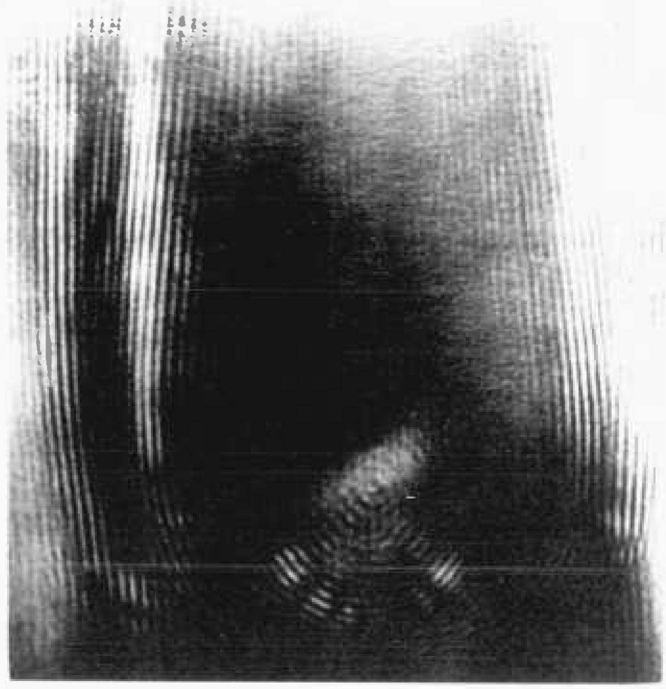

Figure 4.15b Doppler fringe pattern due to a flame

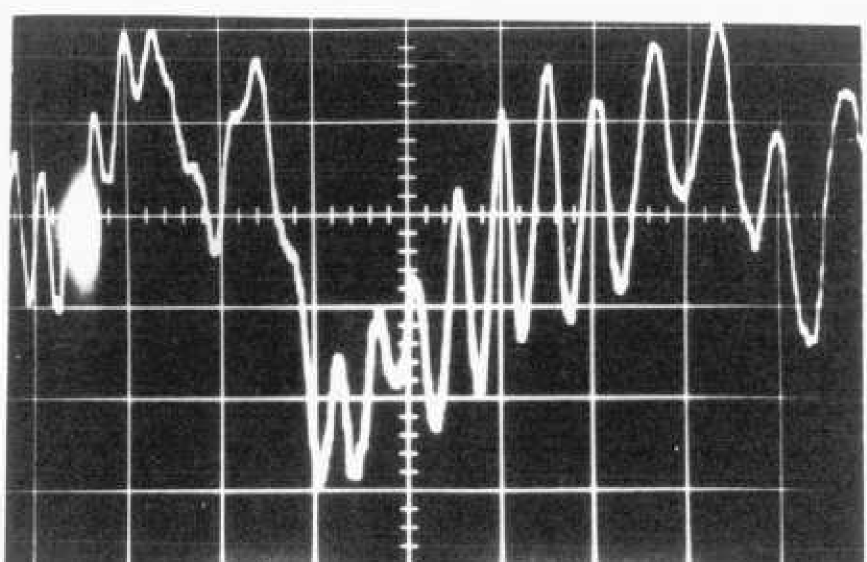

Figure 4.15c Oscillogram trace of Doppler beat frequency signals produced by moving a flame manually across the test space

of sideways deflection are due to the two long diffusion flame interfaces with the surrounding atmosphere, but, as the interferogram clearly shows, there is also a small central premixed front propagating downward in the centre. The oscillogram of Figure 4.15c was recorded at a sweep speed of 10 ms/cm. and at a sensitivity of 50mV/cm.. The frequency ranges from 333 ± 10% to 125 ± 5% Hz, corresponding to velocities between 17.1 ± 11% and 6.4± 6% cm. per second (from equation 4.2b.4) is a measure of the unsteadiness of the operator's hand movement.

4.5c <u>Velocity Measurements of Flame Propagation In A Tube</u>

A stoichiometric mixture of propane and air (4.02% propane, the fuel flow rate was 4.6 c.c./sec.) was introduced into a sloping transparent tube of rectangular cross-section (Figure 4.16) with the sliding door open. After a few minutes the sliding door was closed and the mixture ignited by a spark produced inside the tube. A high speed movie camera (400 frames per second) was synchronized with the ignition spark, and a high speed cine sequence of the fringe patterns was taken (The camera used was a 16mm. Miliken with pin register, using Kodak high contrast negative film 7457 developed in D76 for five minutes at 68° F) at the same time the oscillogram trace was recorded. A cine sequence of the moving interferogram is shown in Figure 4.17. Figure 4.18 shows the corresponding oscillogram. It is seen that the flame front can be of complex and varying shape and gives rise to varying flame

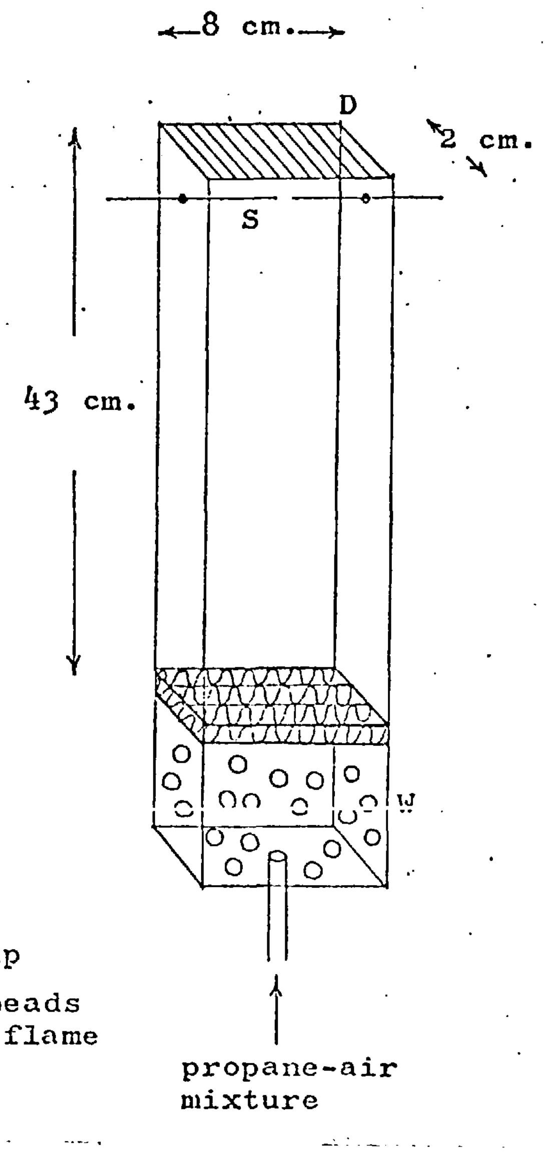

D - sliding door

S - 1 mm. spark gap

W - bed of glass beads surmounted by flame trap matrix

Figure 4.16 The flame propagation tube

Figure 4.17 A high speed cine sequence of fringe pattern for a flame propagating down a tube

speeds. In addition to the large variation of frequency along the trace, different regions gave different velocities. There is, of course, no reason why flame speed (as distinct from burning velocity) should be constant. However, this section has been included by way of warning of what might happen during burning velocity measurements when particles are introduced in the gas stream. If the flame front is convoluted and its fringe structure interacts with that of a particle, there is no guarantee that the particle itself encounters that part of the flame front. It may lie somewhere else along the beam, since the depth of focus of the method is very large and will generally include the depth of the entire working space. Such possible anomalies must be eliminated by a suitable arrangement of the combustion system. In some instances it may be necessary to inject particles along a particular stream tube. As regards the above measurement of flame speed, making the tube vertical and confining the test space by a narrow slit (Figure 4.19) disposes of this particular problem; Figure 4.20a,b,c show oscillograms corresponding to three propane/air mixtures. Using equation 4.2b.4 and $\theta = 10^{-3}$Rd ±1%, Table 4.1 summarizes the flame speed obtained from them.

<u>Table 4.1</u>

Figure Number	Propane(%)	ν_b(Hz)	Flame speed($cm.s^{-1}$)
4.22a	4.02	800 ±3%	41.16 ± 4%
4.22b	5.21	519 ±1%	26.70 ± 2%
4.22c	6.03	237 ±1%	12.19 ± 2%

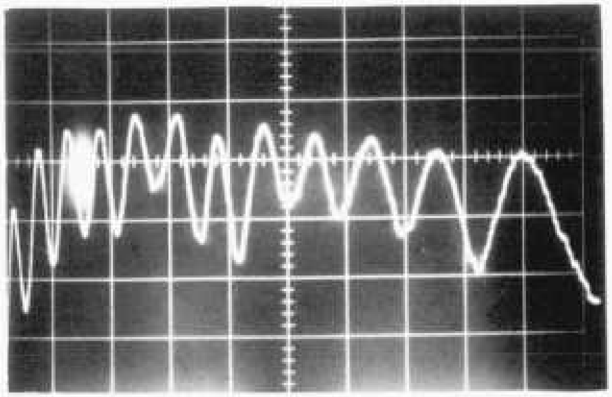

Figure 4.18

Typical oscillogram trace of beat frequency produced by the moving fringe patterns shown in Figure 4.17

(a)

(b)

(c)

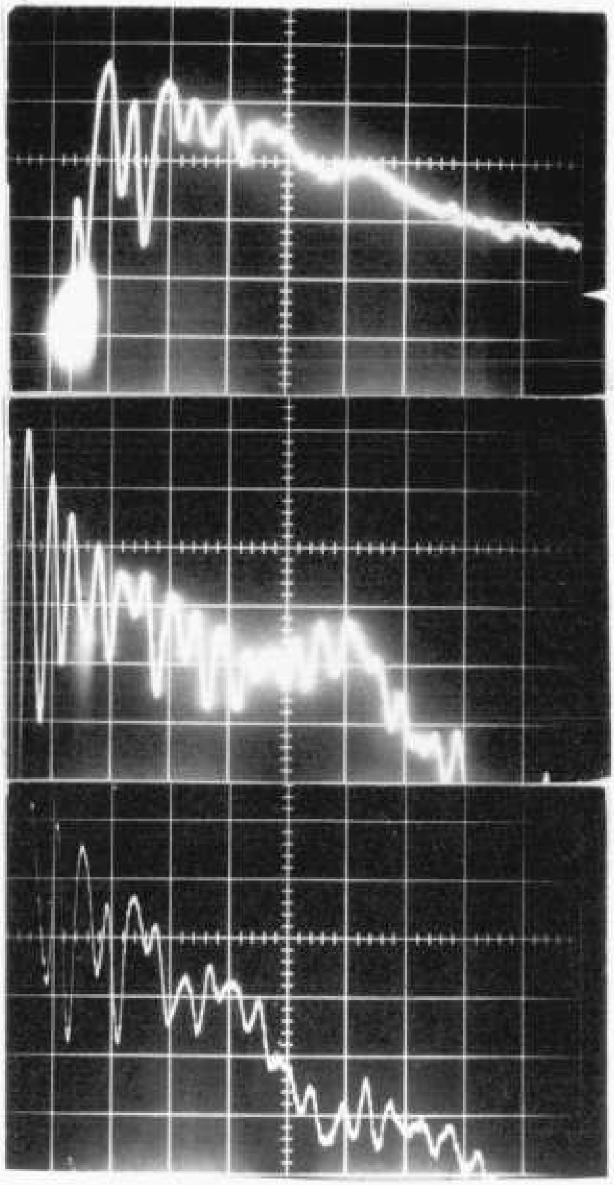

Figure 4.20 Three oscillogram traces of Doppler beat frequency signals corresponding to three propane-air mixtures in table 4.1

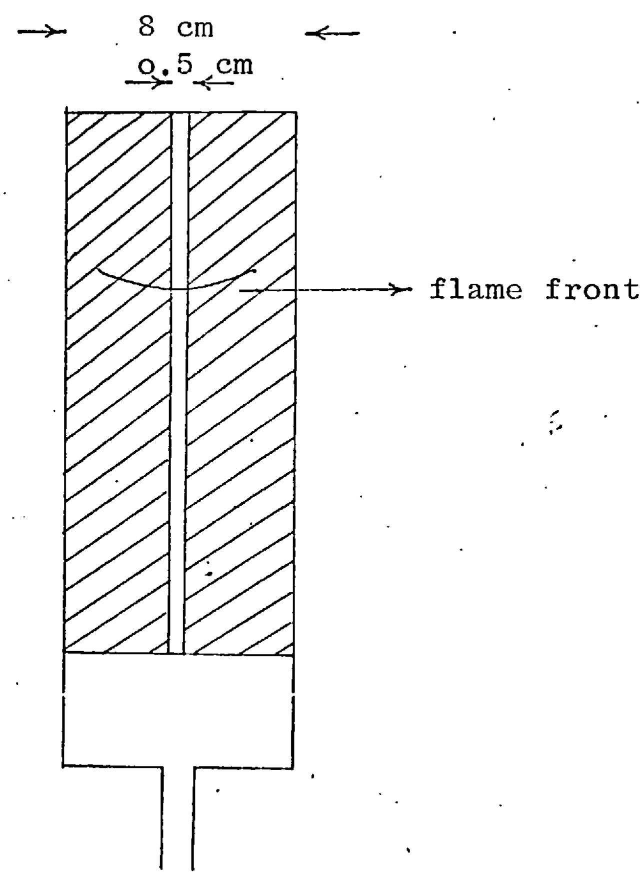

Figure 4.19 Optical confinement of the flame propagation tube

4.5d Velocity Measurements of Particles

The outer diameter, the diameter of the inner ring and that of the central aperture of the schlieren blind used were 1.2, 1.0 and 0.01 cm. respectively. Figure 4.21a shows a fringe pattern produced by a 0.8 mm. particle. In this instance, it is clear that the correct velocity of the particle will be portrayed only when the centre line of its fringe pattern traverses the aperture of the photomultiplier; when this happens, the frequency of the oscillogram is constant.

A fluidized bed was constructed, and the velocity of the air stream was measured using 75 μm particles (Ponty Bond 2156). Figure 4.21b shows a record of the beat frequency produced by a single particle travelling at 9.65 cm./sec. ±4%. The flow of air was ½l./sec., which flows through a tube of 4 cm. radius in the test space, so that the air flow velocity is 9.95 cm./sec. which is consistent with the above finding.

4.5c Measurement of the Burning Velocity of a Stationary Flame

This measurement was achieved by allowing the interference pattern due to one particle to interact with that of a stationary flame. Figures 4.22a,b,c and d show a burner-stabilized premixed flame, the same flame with particles injected, the fringe pattern produced by one part of the flame in the absence of particles and the same with the particles

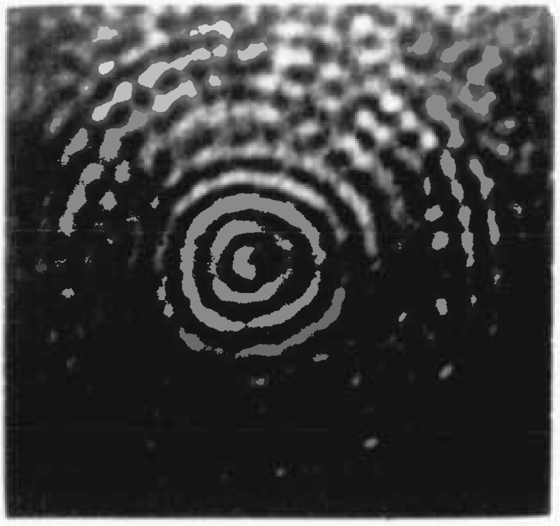

Figure 4.21a Fringe pattern produced by a 0.8 mm particle

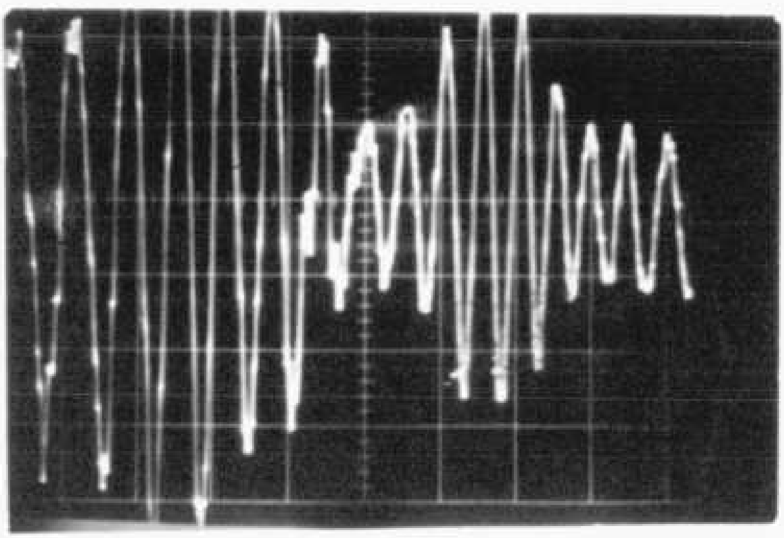

Figure 4.21b Oscillogram trace of Doppler beat frequency produced by a moving particle (70 µm)

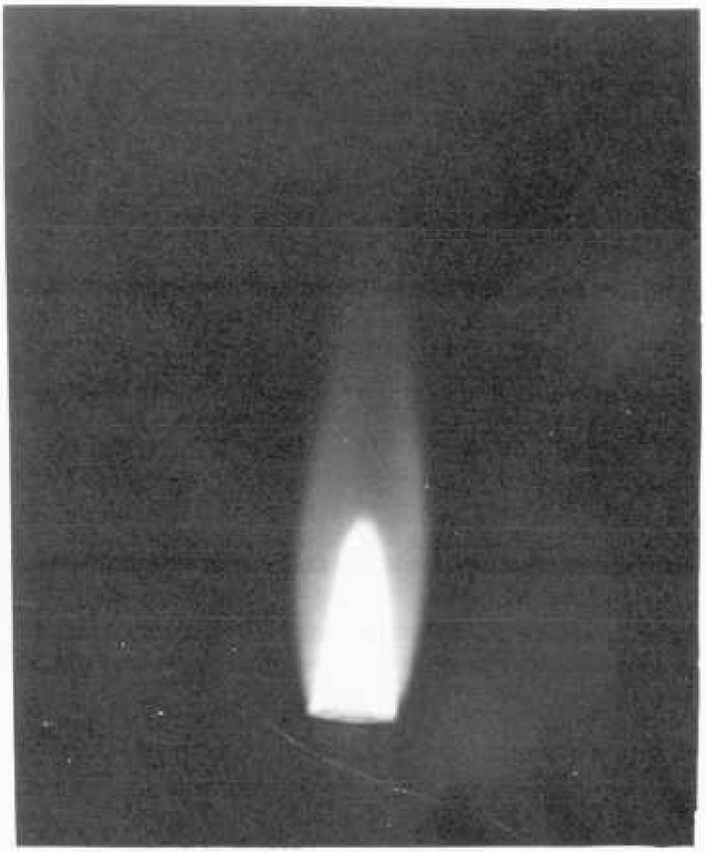

(a)

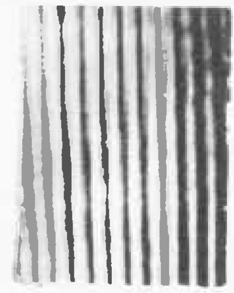

(c)

Figure 4.22c
Fringe pattern produced by one part of the flame

(b)

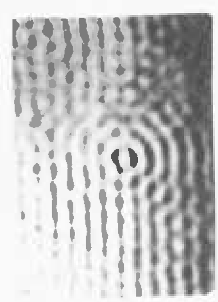

(d)

Figure 4.22d
Fringe pattern as in Figure 4.22c but with particles traversing the flame front

Figure 4.22a A burner-stabilized premixed flame
Figure 4.22b Flame as in Figure 4.22a but with particles injected into the fuel-air stream

traversing the flame front. The propane concentration used was 1.3 times stoichiometric.

Figure 4.23 is a schematic diagram of the apparatus used for injecting particles into the flow system. Glass particles of 5 to 10 μm were used. With an enlarged aperture over the photomultiplier (in this case the aperture diameter was 7 mm.; the optimum size has been discussed in section 4.4b), an oscillogram such as that shown in Figure 4.24 results. The measured velocity corresponds to the orthogonal velocity of one with respect to the other. In this case :

$$\theta = 2.29 \times 10^{-3}\,\text{Rd} \pm 1\%$$

$$\nu_b = 1.25 \times 10^{3}\ \text{Hz} \pm 2\%$$

and therefore the burning velocity, S_u, is:

$$S_u = \lambda_i \nu_b / \theta = 28.1\ \text{cm. s}^{-1} \pm 3\%$$

It is interesting to compare this result with that obtained by Harris et. al. (43), using a stationary flame technique. In this method a part of the cone area approximating a frustrum and excluding areas near the base and tip was selected. The measured burning velocity was 25 cm. s^{-1} for the above propane - air mixture.

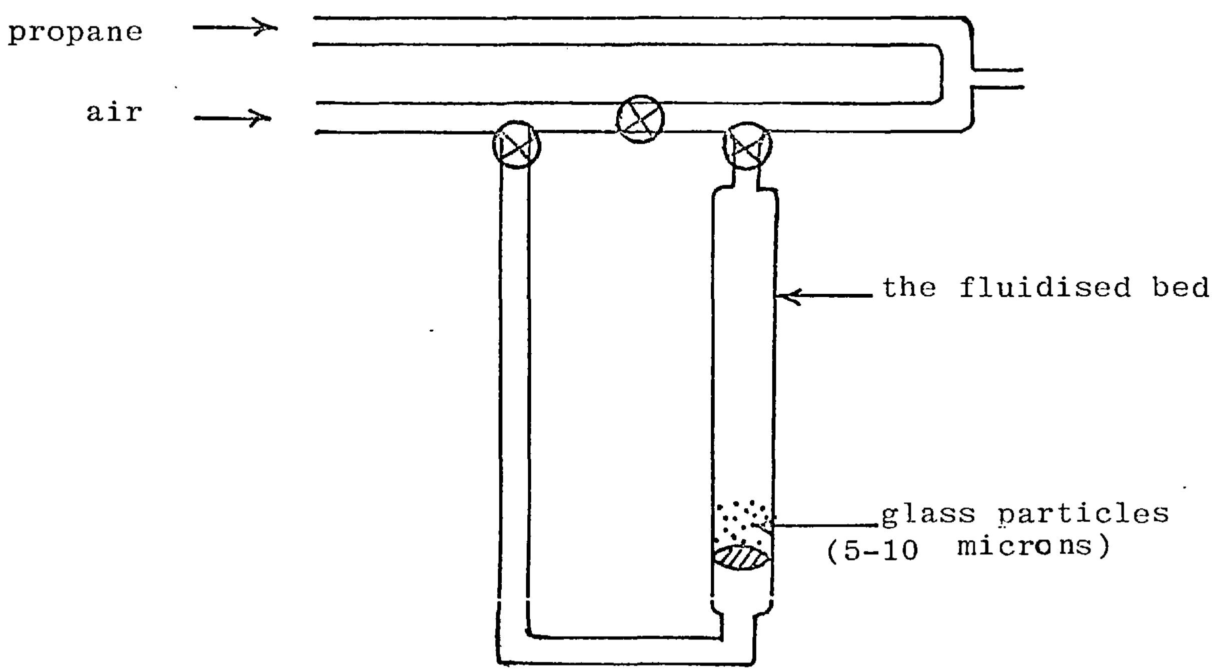

Figure 4.23 The particle injection system

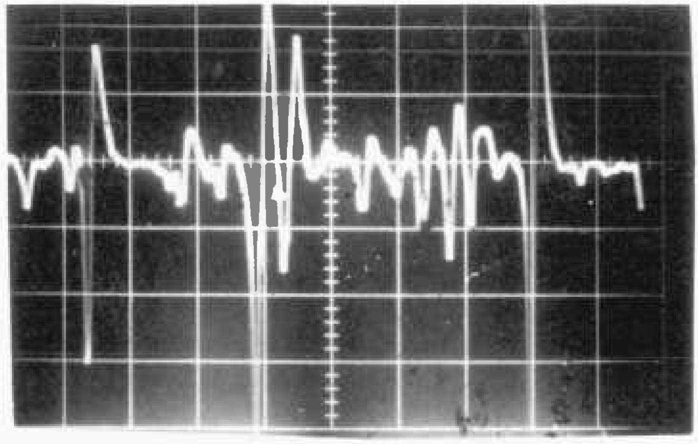

Figure 4.24 Oscillogram trace of Doppler beat signal produced by the fringe pattern due to one particle interacting with that of a stationary flame

(a)

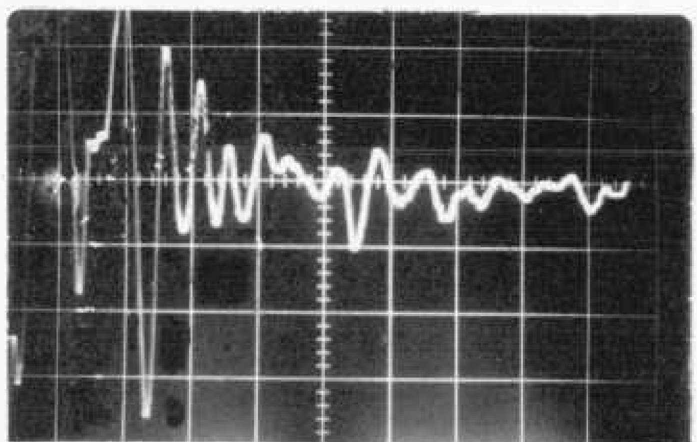

(b)

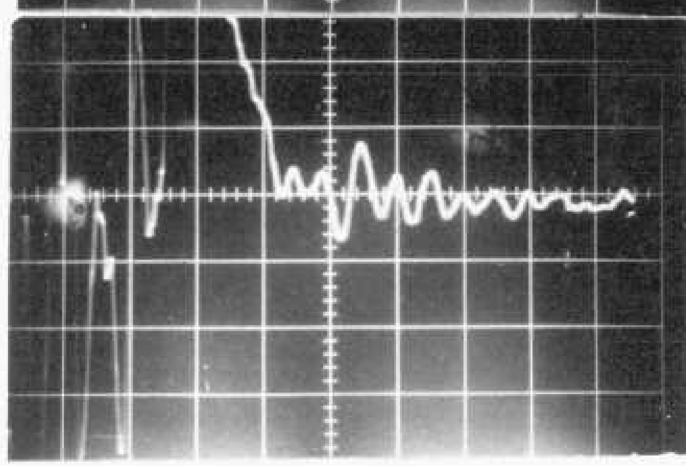

Figure 4.25 a&b
Two oscillogram traces of Doppler beat signals produced by the fringe pattern due to a particle interacting with that of a propagating flame

4.5f Measurement of Burning Velocity of Flame Propagation in a Tube

The rectangular flame propagation tube shown in Figure 4.16 was again used in this case. The aperture in front of the photomultiplier was 7mm. in diameter and glass particles were introduced with the propane - air mixture.

The propane concentration used was 1.3 times stoichiometric. Figures 4.25a and b are two separate photographs of the resulting beat frequencies of the same event repeated twice. Thus the accuracy of measuring the beat frequency is increased. Therefore, by repeating the events many times, one can obtain any desired degree of accuracy in the determination of the beat frequency, so the burning velocity can ultimately be measured to within 1%.

From the oscillograms, the beat frequency is:

$$\nu_b = 1.14 \times 10^3 \mathrm{Hz} \pm 2\%$$

and the burning velocity is:

$$S_u = 25.6 \text{ cm. } s^{-1} \pm 3\%$$

4.6 A Technique For Measuring Turbule Velocities

A knowledge of the velocity fields of buoyant plumes is essential in the computation of the patterns of heat and mass transport, and the heat release distribution in fires.

Their understanding, in turn, is of vital importance in the control of large fires. Furthermore, since most fire detectors depend on natural convection to carry sensible evidence of the fire to the detector, measurements of the upward velocity of the convective column are of paramount importance. An example is that of laser beam fire detectors (1,2), where the flicker frequency is directly dependent upon turbule velocity.

Measurements of velocity profiles inside fire plumes have been attempted using hot wire probes (44,45). However, apart from the disadvantage that the wires are fragile, this technique also suffers in that the calibrations are liable to vary and the wires need supports and mechanical devices for traversing the plume, which renders them rather inversatile. Also, velocity measurements may only be performed in a point by point fashion across the whole plume, which is a laborious process even if the velocity field stays constant throughout the time of measurement. An array of probes may be anticipated. However, this will evidently disturb the flow field and this drawback is inherent in all probe techniques. Yih (46) has tried using soap bubbles in connection with various photographic techniques, but he found that the motion of the bubbles relative to the surrounding air could neither be eliminated nor ascertained.

It is evident from the previous sections of this chapter that the laser Doppler technique can be advantageously employed in measuring turbule velocities, either using one photodetector traversing the image of the plume or utilizing an assembly of photodetectors placed in selected positions throughout the 'Doppler interferogram' of the plume. However, the size of the plume under test is limited by the practical dimensions of the schlieren lenses (or mirrors). Schwar et.al. (47) has proposed the use of large point holograms, but these would allow extension to dimensions only a few times larger than those of large schlieren mirrors and are very wasteful of light.

High speed cine-photography of the plume shadow has been tried, but it was found that the motion of individual turbules is difficult to follow from frame to frame, so the idea was abandoned. However, this method is found to be ideal for determining the shapes and sizes of fire plumes.

This section describes a new technique employing the large-area differential laser interferometer (Chapter 3) together with a chopping device and cine-photography for the measurement of turbule velocities. This method has the advantage that all the relevant data for the determination of the instantaneous distribution throughout the whole plume is contained in one frame of the movie film. Analysis of multiple frames will yield information concerning turbulence intensity distribution inside the plume. Other advantages are the automatic recording of the plume shadowgram and that the maximum dimension of the test object is in practice only limited by the size of the available screen and the maximum field of view of the camera used.

4.6a The Apparatus

A great merit of the setup for the present purpose is that it is exactly the same as the large-area differential laser interferometer with the exception of an additional shutter system. The shutter system employed was a motor-driven sectored disc shown in Figure 4.26. The sectored disc was placed in front of the laser and the exposure interval t_e is given by:

$$t_c = r\omega\ /nl \qquad 4.6a.1$$

where

$$l = r\pi/12 \qquad 4.6a.2$$

ω is the angular velocity of the motor, r is the radius of the sectored disc and n is an integer whose value ranges from one to twenty-four. Since r is fixed at 14 cm., t_e can be adjusted by varying the motor speed, the value of n or both. A stable Comtex motor in conjunction with a Gallenkemp variable geared stirrer was used. Figure 4.27a shows the arrangement used for measuring the motor frequencies. Figure 4.27b is a

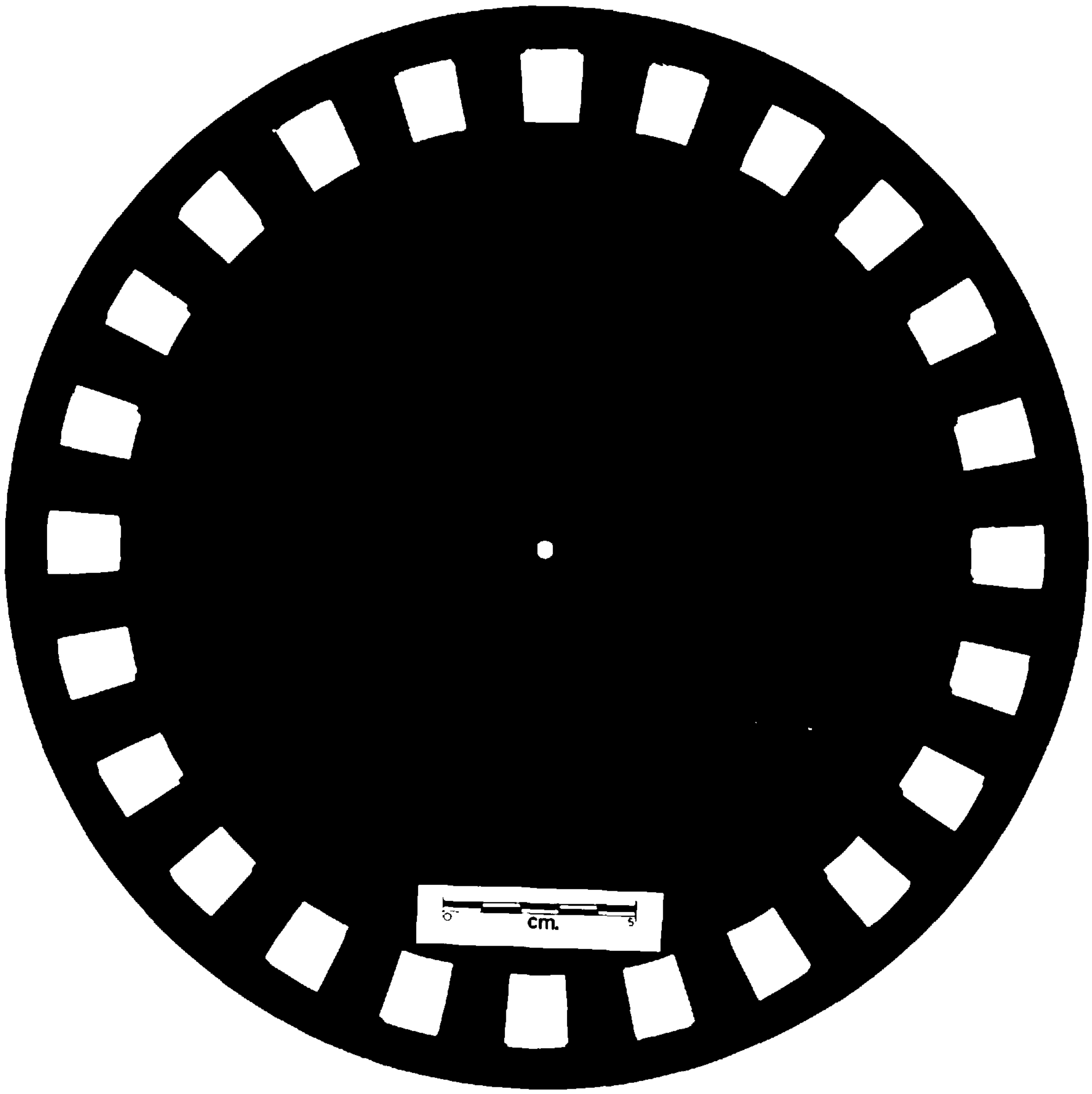

Figure 4.26 The sectored disc

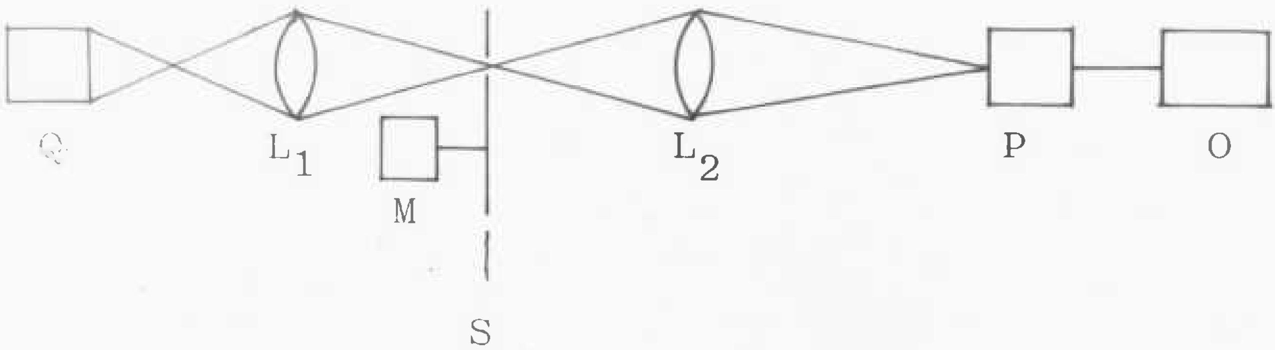

Figure 4.27a Schematic diagram of the set up used for measuring chopping frequencies.
Q, quartz -iodine lamp and condenser system ;
L_1 & L_2, convex lenses ; M, variable geared electric motor; S, the sectored disc ; P, photocell ; O, Oscilloscope

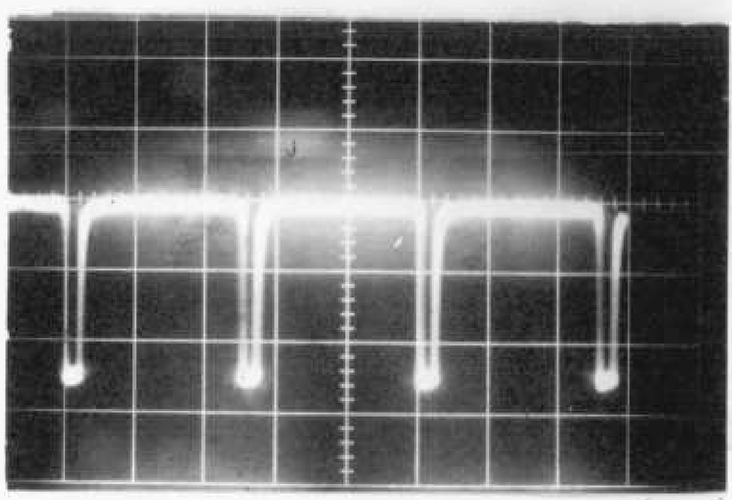

Figure 4.27b Typical oscillogram trace obtained using the setup shown in Figure 4.27a

typical scope trace, and the value of t_e in this case is 9.5 ms.

Turbule velocity measurements were made using triple exposures. The interval between each exposure could be varied from 1/714 to 1/30 second and the sensitivity of the system could be altered simply by changing the distance between the test object and the screen. Triple exposures were chosen so as to ascertain that the multiple exposures were due to the same turbule. The process of calculating the turbule velocity can be understood with the aid of Figures 4.28a and b. Either a common feature was picked out for each exposure of the turbule shadow (Figure 4.28a) or tangents were drawn on them to determine the direction of the turbule. The absolute turbule velocity, v_t, is given by:

$$v_t = K_c(d/t_e) \qquad 4.6a.3$$

where K_c is a constant depending upon the magnification of the system and the scale of a movie analyser. In practice, the distance d_y and d_x was measured so that the axial and radial velocity components can be computed as well as v_t.

4.6b Experimental Tests

In order to test the system, ethyl alcohol was burnt in petri dishes of various diameters. The burning time was determined in each case and photographs were

(b) (a)

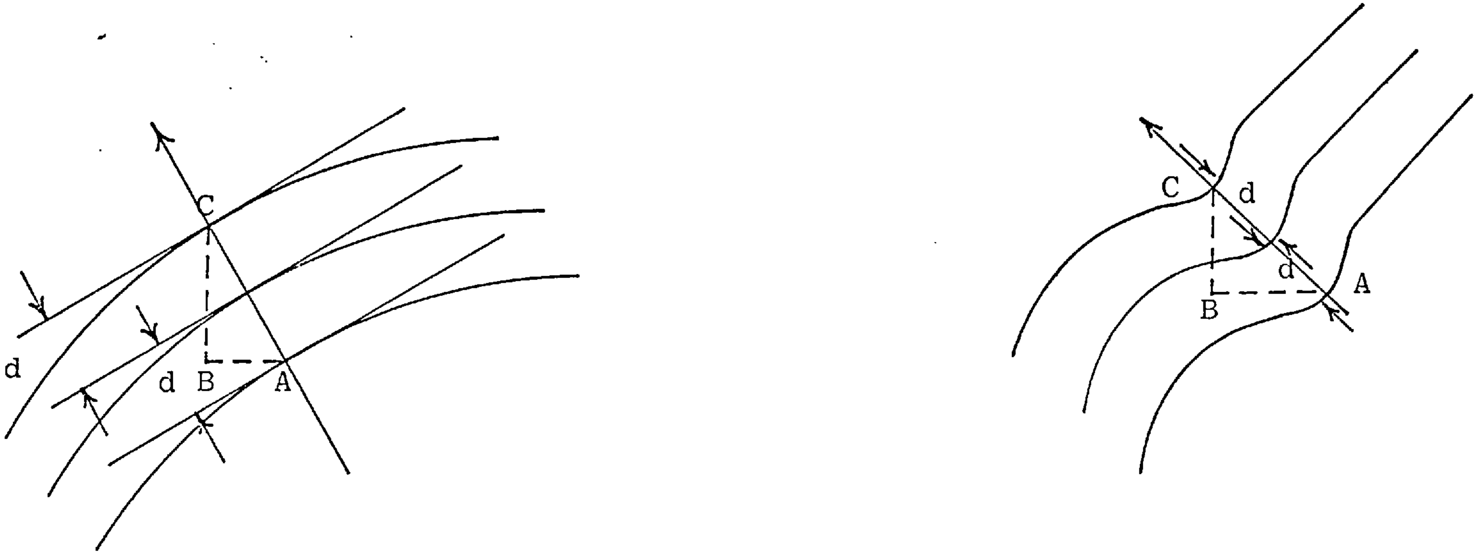

Figure 4.28 a&b Diagams illustrating the calculation of turbule velocities from triple exposure shadowgraphs.

CB = d_y ; BA = d_x

taken at a consistent stage of burning. Figure 4.29 is an example of such photographs with triple exposures. The dish diameter in this case was 12 cm. and the dish height was 2.5 cm..

The fire plume is, of course, a three-dimensional phase object and it is possible from photographs like this to deduce point by point velocity distribution of the plume in three diminsions (48, velocity measurements were done in this case using a schlieren system and photographing the scope traces as the turbules traverse three equidistant slits in front of a photomultiplier). However, we are interested here in the behaviour of a laser beam pasing through fire plumes and the relevant factors are the average velocities and velocity fluctuations up the column of a fire plume. Since this was a turbulent system. measurements were only meaningful if large samples were taken. Therefore, a method was devised in which the interrupted shadow interferometry was combined with cinephotography (a Vinten scientfic movie camera was used) in which the speed of the camera was synchronized with the chopper speed, so that it was possible to measure local turbule velocities from every frame. With 4000 frames in every 100 feet of film, a very large number of measurements could be taken. Thus enabling us to calculute the average velocity and turbulence intensity.

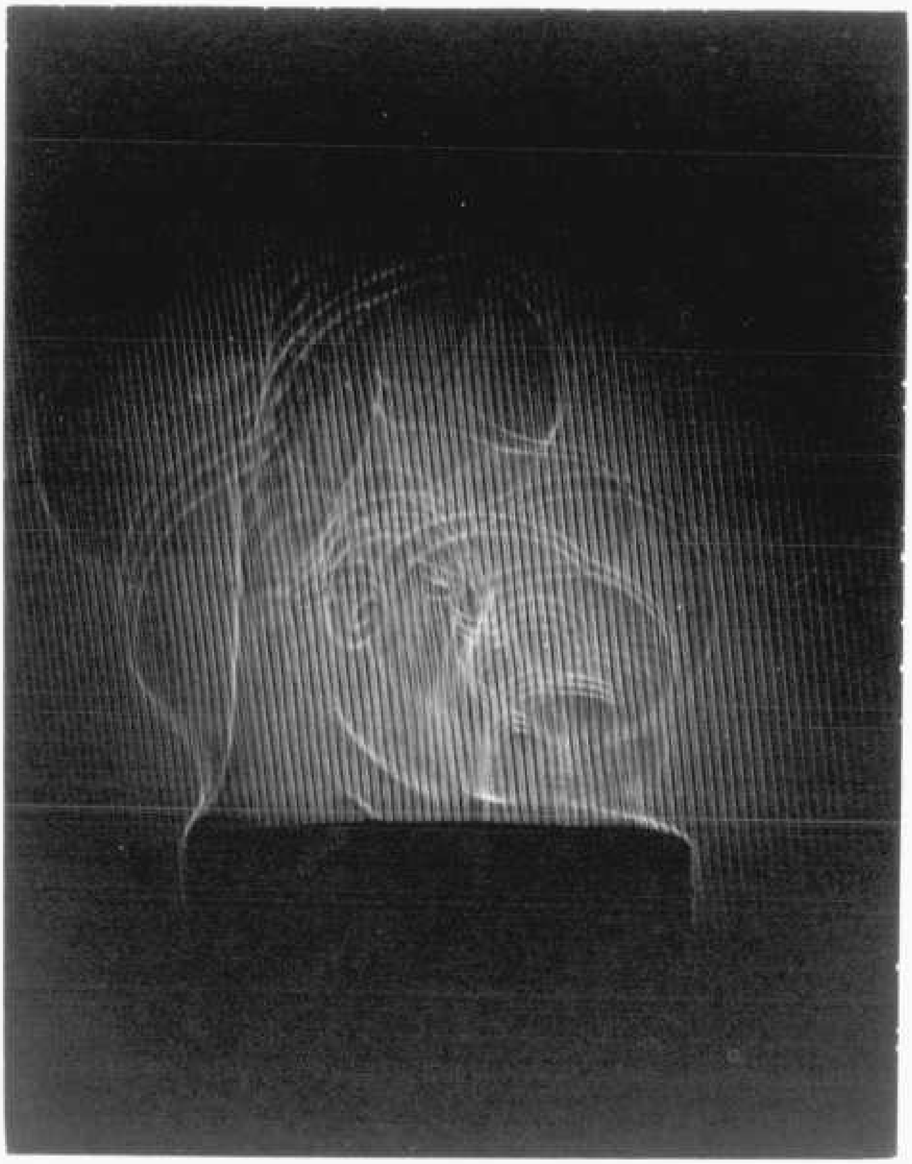

Figure 4.29 A typical triple exposure photograph of a fire plume due to a liquid pool fire

4.7 Conculsions

A theory has been presented describing in detail the nature of a new method for measuring the normal propagation velocities of phase objects. This is particularly useful in combustion research because it provides a very simple means of measuring burning velocities, orthogonal velocities of detonations and shock waves directly. The optimal design of each element of the apparatus has been investigated. The method has been successfully tested on moving diffraction gratings, particles, flames stabilized on a burner and propagating in a tube. The measured burning velocity for a propane-air mixture with a propane concentration of 1.3 times stoichiometric was found to be 26.8 cm./sec. (±3%), which agrees well with an elaborate stationary flame technique (43). It is believed that the method can be usefully employed to obtain a complete set of data on burning velocities.

It was demonstrated that a simple adaptation of the large-area differential interferometer provides a very simple and direct method for measuring turbule velocities. Apart from being capable of fulfiling the present objectives of measuring flicker frequencies of laser fire detectors and upward convective velocity distributions inside fire plumes, the method can be utilized to measure plume profiles, temperature distributions and detailed point by point velocity distributions inside fire plumes.

With the ease of availability of fast optical shutters such as the Kerr cell (t_e down to about 10^{-8} second), the technique can be easily adapted to measure a variety of high speed phenomena of interest in combustion research.

CHAPTER 5

Velocity and Turbulence Intensity Distributions Within Plumes Above Liquid Pool Fires

5.1 Introduction

Laser fire detectors are generally ceiling-mounted. These detectors receive information of an outbreak of fire via the hot air plume rising above a burning zone. The mechanism of plume formation in fires is basically that the hot products generated in a fire, being lighter than the ambient air, experience an upward buoyant force. Thus a column of rising hot gas is formed. Workers in fluid dynamics have made various theoretical attempts to analyse convection plumes above fires. (49, 46, 50, 51, 52, 53, 54,55, 56, 57,58,45,59,60,61,62)

From these and numerous other efforts, it is seen that precise quantitative analysis of such free convection driven flow fields is generally not feasible. Except for a few special fire configurations amenable to boundary layer treatment, numerical flow field analysis is required. Even the numerical approach is beset with serious difficulties due to turbulence and the general geometric complexity of real fires. It is believed that this is an area of science (as in many other areas) where the most fruitful results can only be obtained through the co-ordinated efforts of both the theorists and the experimentalists.

The purpose of the present endeavour is not to improve the present modelling techniques, (however, a theoretical development is given in the Appendix) it is to devise a new optical technique for the measurements of velocity and turbulence intensity distributions within fire plumes (section 4.7). Nevertheless, a brief summary of several theoretical considerations will be given and the well-known result concerning the variation of the average upward plume velocity with height (in weakly buoyant plumes) will be used to test the viability of the analysis. Although for laser fire detectors, the region of primary interest is the upper weakly buoyant portion of the plume and the present objective is to measure the laser flicker frequencies for different source sizes, this is important because it enables one to distinguish between the convective turbulence resulting from an unwanted fire and random fluctuations due to ambient conditions such as temperature changes, draughts etc.. However, the method also lends itself very readily to the study of the lower regions of a fire plume, where modelling is most difficult because of very significant heat transfer by radiation and is further complicated by fuel breakdown (due to vaporization) and combustion.

In the application of laser fire detectors, the fire plume is generally enclosed by walls. Impingement of the fire plume on a ceiling, results in a gas flow near the ceiling even at a considerable distance from the fire axis. The present technique was also used to measure the gas velocity distribution along a ceiling.

Ethanol pool fires were used throughout the experiment as fire sources. Thus the heat of combustion was known and the source size could be varied simply by chnaging the pan diameter. Also the rate of burning of ethanol remains fairly constant with time(63). Another advantage of choosing burning pools of a light fuel is that the fire plumes from such sources in the horizontal boundary of an otherwise unrestricted and calm atmosphere provides one of the simplest types of fires for theoretical modelling, since the essential interaction between flame and fuel is present, but complications due to pyrolysis and fuel geometry are reduced to a minimum.

A discusion of liquid pool fires is given in section 5.3 together with some experimental observations. The results of velocity and turbulence intensity distributions for source diameters varying from 1.3 to 12.5 cm. and the variation of the gas velocity along a ceiling as well as the characteristic of laser flicker frequencies are presented in section 5.4.

5.2 Theoretical Consideration of Fire Plumes

According to the present experimental observations for open ethanol pool fires, the hot gas column is largely turbulent for all pan sizes larger than about five centimetres. Even for smaller pan sizes, the flow becomes fully turbulent after a distance of a few pan diameters. Therefore, in the study of ceiling-mounted laser fire detectors, we are only interested in turbulent convection columns.

Theoretical treatments of the turbulent diffusion flame and resulting convection column may be broadly divided into two regions. The first contains that part of the flame between the fuel source and the point at which sufficient air has been entrained to provide a surface of stoichiometric mixture of fuel and air. In this region, the maximum temperatures are high, radiation plays an important role and the gases are strongly buoyant. The second region uses the final condition of the bottom region as the inital condition and continues to infinity. In this region, the temperatures have fallen to levels at which the plume behaviour is weakly buoyant.

5.2a Weakly Buoyant Plumes

The basic assumptions underlying theoretical treatments for turbulent, weakly buoyant plumes are :

1. The Boussinesq approximation (64) : Variations of density is neglected in so far as they affect inertia and need be taken into account only through the resulting buoyancy forces.
2. The similarity assumption : The mean profiles of longitudinal velocity, temperature and density are similar in shape at all heights above the source.

This assumption is based on the fact that turbulent plumes spread slowly with increasing distance from the source, so that the flow may be expected to be self-preserving and profiles of mean quantities to be approximately similar.

3. The entrainment velocity v is taken to be some fraction α of the mean vertical velocity on the plume axis.
4. Mixing in the vertical direction is negligible compared to that in the horizontal direction - a boundary-layer type of approximation valid for slowly spreading flows; and that molecular diffusion is negligible relative to turbulent diffusion.
5. The ambient fluid is of uniform density and temperature - most open fires and all laboratory flames are not large enough so that atmospheric density and temperature variations are worthy of consideration. However, it is possible to include variations of this type (65).
6. The properties have one constant value inside the plume, and another outside it, i.e. a "top hat" profile. For example,

$$u(z,r)=\begin{cases} u(z) & 0 \leqslant r \leqslant b(z) \\ o & b(z) < r \end{cases} \qquad 5.2a.1$$

7. Radiation from the flame is neglected.

Let $<u>$ and $<v>$ be the components in the z (axial) and r (radial) directions, of the time-mean velocity of the fluid at a point inside the plume

flow field as shown in Figure 5.1 (c.f. equation 4.3b.5). Then from the standard conservation equations of fluid dynamics (an alternative derivation is given in the Appendix), the governing equations for the plume field are:
Continuity equation:

$$\frac{\partial}{\partial z} \langle u \rangle + \frac{1}{r} \frac{\partial}{\partial z} (r\langle v \rangle) = 0 \qquad 5.2a.2$$

Conservation of momentum :

$$\{ \langle u \rangle (\partial \langle u \rangle / \partial z) + \langle v \rangle (\partial \langle u \rangle / \partial r) \}$$

$$= g/\langle \rho \rangle (\rho_\infty - \langle \rho \rangle) - 1/r \, \partial/\partial r (\langle u'v' \rangle) \qquad 5.2a.3$$

Conservation of energy :

$$\{ \langle u \rangle (\partial H/\partial z) + \langle v \rangle (\partial H/\partial r) \}$$

$$= - 1/r \, \partial(rq)/\partial r = - C_p/r \, \partial(\langle v'T' \rangle)/\partial r \qquad 5.2a.4$$

By integrating over the plume and noting that the velocity field tends to zero at infinity, the conservation equations become :
Conservation of total mass flow in the plume :

$$d/dz \int_0^\infty r\langle u \rangle dr = - \lim_{r\to\infty} r\langle v \rangle \qquad 5.2a.5$$

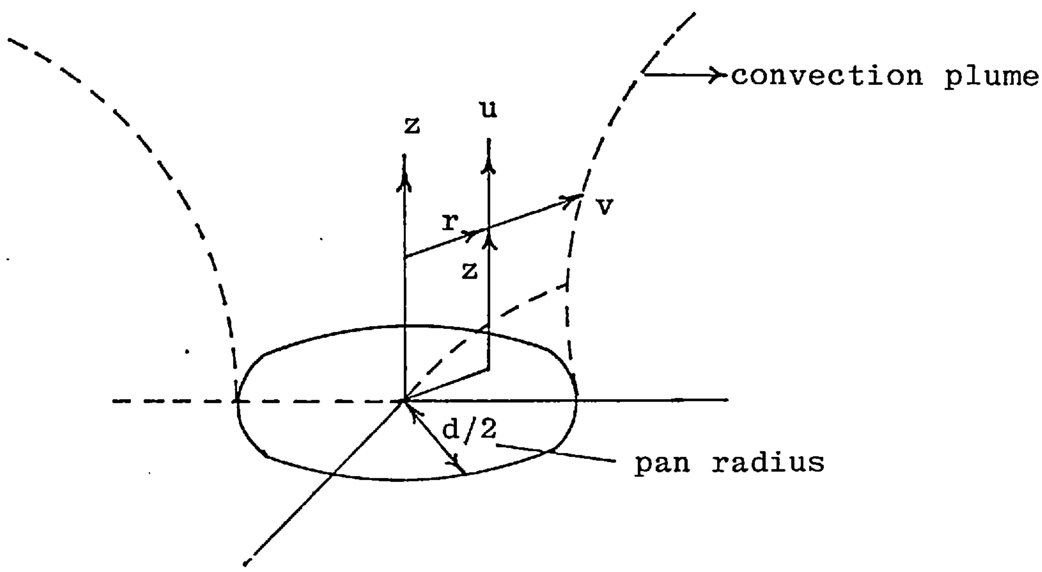

Figure 5.1 Plume field depicting coordinate system

From assumption 3, we have

$$- \langle v \rangle = \alpha \langle u \rangle \qquad 5.2a.6$$

Equation 5.2a.5 may then be written :

$$d/dz\ (\bar{u}\ \bar{b}^2) = 2\alpha\bar{u}\bar{b} \qquad 5.2a.7$$

where the mean velocity $\bar{u}$ is :

$$\bar{u} = \int_0^\infty r\langle u^2\rangle dr \ / \int_0^\infty r\langle u\rangle\ dr \qquad 5.2a.8$$

and the mean width $\bar{b}$ is given by :

$$\bar{b}^2 = 2 \int_0^\infty r\langle u\rangle\ dr \ / \ \bar{u} \qquad 5.2a.9$$

The mean values $\bar{u}$ and $\bar{b}$ may be looked upon as defining the equivalent top-hat profiles.

Conservation of momentum :

$$d/dz \int_0^\infty r\langle u^2\rangle dr = g/\langle\rho\rangle \int_0^\infty r(\rho_\infty - \langle\rho\rangle)\ dr \qquad 5.2a.10$$

or

$$d/dz\ (\bar{u}^2\bar{b}^2) = g/\bar{\rho}\ \bar{b}^2\ (\rho_\infty - \bar{\rho}) \qquad 5.2a.11$$

Conservation of energy :

$$d/dz \int_0^\infty r\langle u\rangle\ \langle H\rangle dr = -\lim_{r\to\infty} r\langle v\rangle\ \langle H\rangle \qquad 5.2a.12$$

or

$$d/dz\ (\bar{b}^2\bar{u}\langle H\rangle) = 2\alpha\bar{b}\bar{u}\ H_\infty \qquad 5.2a.13$$

From equation 5.2a.7, equation 5.2a.13 may be written :

$$d/dz\ \{(H_\infty - \bar{H})\ (\bar{b}^2\bar{u})\ \} = 0 \qquad 5.2a.14$$

But

$$H_\infty - \bar{H} = C_p\ (T_\infty - T) \qquad 5.2a.15$$

Therefore, equation 5.2a.14 implies that

$$\tau\ \bar{b}^2\ \bar{u} = \text{constant} = K \qquad 5.2a.16$$

where

$$\tau = (T - T_\infty)\ /\ T_\infty \qquad 5.2a.17$$

Assuming perfect gas , then

$$(\rho_\infty - \bar{\rho})/\bar{\rho} = \{\rho_\infty - (\rho_\infty T_\infty/\ T)\}/(\rho_\infty T_\infty/T)$$

$$= (T-T_\infty)/T_\infty = \tau \qquad 5.2a.18$$

and equation 5.2a.11 becomes :

$$d/dz\ (\bar{u}^2\bar{b}^2) = g\tau\bar{b}^2 = gKu^{-1} \qquad 5.2a.19$$

From equation 5.2a.19, we may write :

$$d/dz\ (\bar{u}^2\bar{b}^2)^2 = gK\bar{u}\bar{b}^2 \qquad 5.2a.20$$

Combining equations 5.2a.20 and 5.2a.7, we have :

$$d^2/dz^2\ (\bar{u}^2\bar{b}^2)^2 = 2gK\alpha\bar{u}\bar{b} \qquad 5.2a.21$$

A solution of this equation is :

$$\bar{b}\bar{u} = ((9/20)\ gK\alpha)^{1/3}\ z^{2/3} \qquad 5.2a.22$$

Substitution of this result into equation 5.2a.20 gives :

$$\bar{b}^2\bar{u} = 6\alpha/5\ ((9/20)\ gK\alpha)^{1/3}\ z^{3/5} \qquad 5.2a.23$$

Equations 5.2a.22 and 5.2a.23 yield :

$$\bar{b} = (6\alpha/5)z \qquad 5.2a.24$$

and

$$\bar{u} = 5/6\ (9\ gK/20\ \alpha^2)\ z^{-1/3} \qquad 5.2a.25$$

The result that the average upward velocity within weakly buoyant plumes is inversely proportional to the 1/3 power of the axial distance is supported by experimental evidences (52, 76), and will be shown to be in accord with present measurement.

5.2b <u>Strongly Buoyant Plumes</u>

For a proper treatment of strong buoyancy, the most important modifications to the weak buoyant plume model are:

1. Full account must be taken of variations in density.
2. Losses due to radiation must be included.
3. Entrainment will involve the additional factor, $\langle\rho\rangle/\rho_\infty$.

When these factors are taken into account, the governing differential equations become :

Conservation of mass :

$$\partial/\partial z\ (\langle\rho\rangle\langle u\rangle) + 1/r\ \partial/\partial z\ (r\langle\rho\rangle\langle v\rangle) = 0 \qquad 5.2b.1$$

Conservation of momentum :

$$\langle\rho\rangle\ \{\langle u\rangle(\partial\langle u\rangle/\partial z) + \langle v\rangle(\partial\langle u\rangle/\partial r)\}$$

$$= g\ (\rho_\infty - \langle\rho\rangle) - 1/r\ \{\partial(\langle\rho\rangle\langle u'v'\rangle)\}/\partial r \qquad 5.2b.2$$

Conservation of energy :

$$\langle\rho\rangle\ \{\langle u\rangle(\partial\langle H\rangle/\partial z) + \langle v\rangle(\partial\langle H\rangle/\partial r)\} + \langle u\rangle g\rho_\infty$$

$$= 1/r\ \partial(rq)/\partial r - Q_r \qquad 5.2b.3$$

where radiation losses are expressed in the term Q_r.

The flux of radiation from the hot plume gases depends on the composition of these gases, on the concentration of carbon dioxide and water vapour, and particularly on the presence of finely divided carbon particles and ash (In chapter 2, it was established that emissivity due to a cloud of soot particles is strongly dependent upon the shape of the sooty agglomerates). With a proper choice of ε, we may assume that the plume radiates as a black body. Then:

$$\int_0^{\bar{b}} Q_r \, dr = 2\bar{b}\sigma\varepsilon \, (\bar{T}^4 - T_\infty^4) \, \{1+(d\bar{b}/dz)^2\}^{\frac{1}{2}} \qquad 5.2b.4$$

Following the integral treatment as given in section 5.2a, the above conservation equations may be written :

Continuity equation :

$$d/dz \, (\bar{b}^2\bar{\rho}\bar{u}) = 2\bar{b}\alpha \, (\bar{\rho}\rho_\infty)^{\frac{1}{2}} \, \bar{u} \qquad 5.2b.5$$

Conservation of momentum :

$$d/dz \, (\bar{b}^2\bar{\rho}\bar{u}^2) = g\bar{b}^2 \, (\rho_\infty - \bar{\rho}) \qquad 5.2b,6$$

Conservation of energy :

$$d/dz \, \{(H_\infty - \bar{H}) \, \bar{b}^2\bar{\rho}u\}$$

$$= g\rho_\infty\bar{b}^2\bar{u} + \bar{b}\sigma\varepsilon \, (\bar{T}^4 - T_\infty^4) \, \{1+(d\bar{b}/dz)^2\}^{\frac{1}{2}} \qquad 5.2b.7$$

In the above equations, the entrainment relation assumed was :

$$- \rho_\infty^{\frac{1}{2}}\langle v\rangle = \langle\rho\rangle^{\frac{1}{2}} \langle u\rangle \qquad 5.2b.8$$

This formula was first suggested by Ricou and Spalding (66) to account for the reduced rate of entrainment for flows with $\bar{\rho}/\rho_\infty<1$. Nielsen and Tao (57), on the other hand, have argued that the entrainment is likely to be proportional to the mass velocity and accordingly they used the entrainment relation :

$$- \rho_\infty\langle v\rangle = \alpha\langle\rho\rangle\langle u\rangle \qquad 5.2b.9$$

However, the virtue of equation 5.2b.8 is that it is supported by experiments (66,67,68).

Nielsen and Tao (57) have also introduced a species conservation equation to account for changing gas composition and obtained numerical solutions to the conservation equations.

5.3 Liquid Pool Fires

To devise effective methods for the extinction of liquid fires, it is necessary to have some knowledge of the way in which they burn. The rate of burning and the temperature distribution below the surface of burning liquids have already been extensively investigated (69,70, 71,68,72,73). This investigation is, however, primarily directed towards fire detection, Hence, the most important relevant parameter is the characteristics of the plume above liquid pool fires. Measurements of the structure of the plume boundaries for ethanol pool fires of various diameters will be given as well as the corresponding distributions of the visible flame heights.

5.3a Plume Width

Shadow photographs were taken of the plumes resulting from burning ethanol in circular vessels with diameters ranging form one to twelve centmetres at laboratory conditions. From, several of these ' instantaneous ' (1/10 second exposure) shadowgraphs, it became apparent that the structure of the plume boundary is highly irregular. An example of this 'instantaneous' visualization of the flow is shown in Figure 5.2, where the diameter of the pool is three centimetres.

In order to determine the mean flow, the plume shadows were photographed using a Vinten Scientific cine-camera running at eight frames per second. The apparatus used was again that of the large area differential interferometer described in Chapter 3 (Figure 3.2). This was very convenient, since no modification of the setup for measuring the velocity and turbulence distributions was needed except that the use of the chopper (Fig. 4.27) was no longer necessary, since the exposure time was sufficient to freeze the shadow patterns. A representation of the mean plume profile was achieved

Figure 5.2a Shadowgraph of a plume resulting from a 3 cm. - diameter pool fire

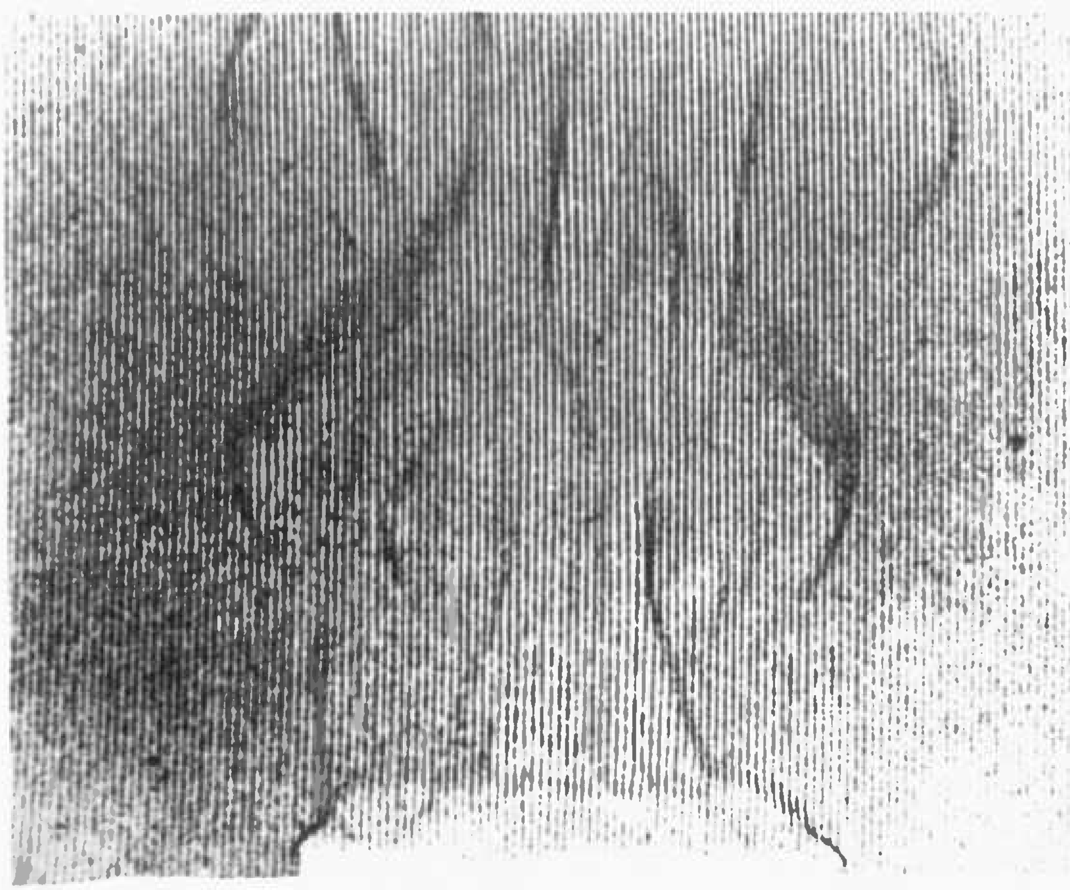

Figure 5.2b Shadowgraph of a plume resulting from a 10 cm.-diameter pool fire

by drawing on a tracing paper while the film ran through a movie analyzer at a high speed (60 frames per second). In this way, several hundred images were superposed. The average flow profiles for vessel diameters of 1,3, and 12 cm. are shown in Figure 5.3.

It is seen that in all cases, the radius of the column at first decreases with height, reaches a minimum and then increases. The latter is approximately conical and the cone angle varies with dish diameter as indicated in Figure 5.4. At pool diameter, d=1 cm., product- rich combustion gases diffuse across the entire pool surface and the visible flame is laminar. At d=3cm. , a region of essentially pure fuel vapour appear over the centre of the pool and the visible flame is still laminar. As d increases to 12 cm., the central region of cold fuel vapour grows and is bounded by a conical laminar flame boundary layer. Transition to turbulence occurs just above the flame boundary layer (Fig. 5.3). When the shadows are viewed continuously, the general configuration of the flame boundary layer is seen to fluctuate. Occasionally, the central fuel vapour region disappears entirely. Turbulence and general instability are apparent on both the inner and outer surfaces of the flame boundary layer.

From Figure 5.4, variations of the column width with height above the pool can be measured and are plotted in Figure 5.5. Thus for pool diameters of 1,3,4.7 and 12 cm.

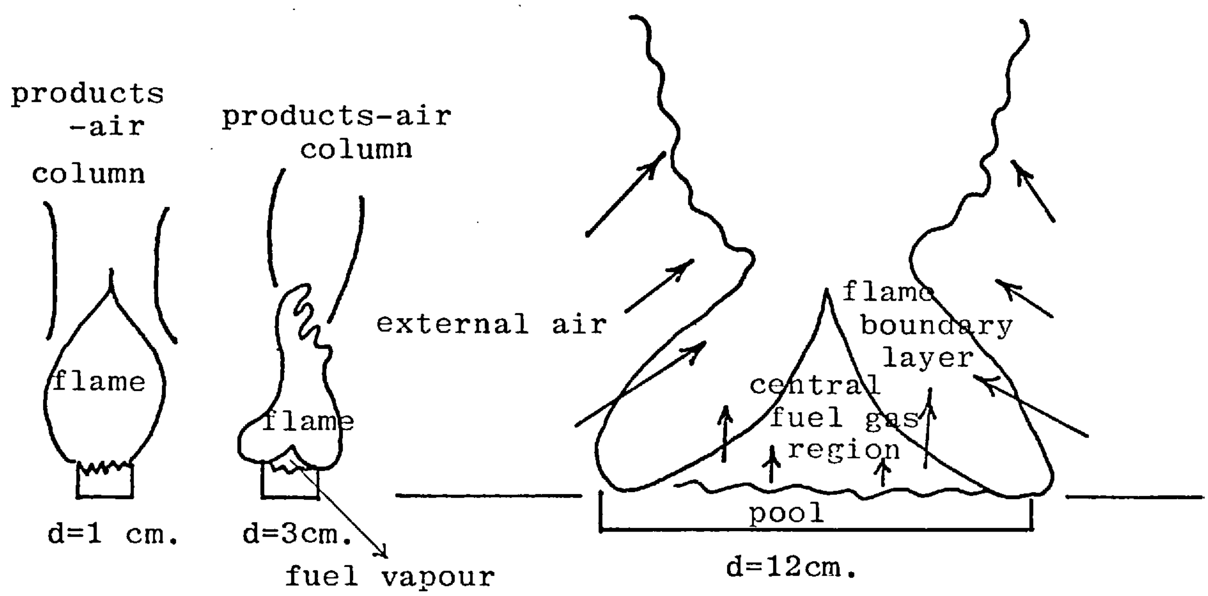

Figure 5.3 Flow Profiles

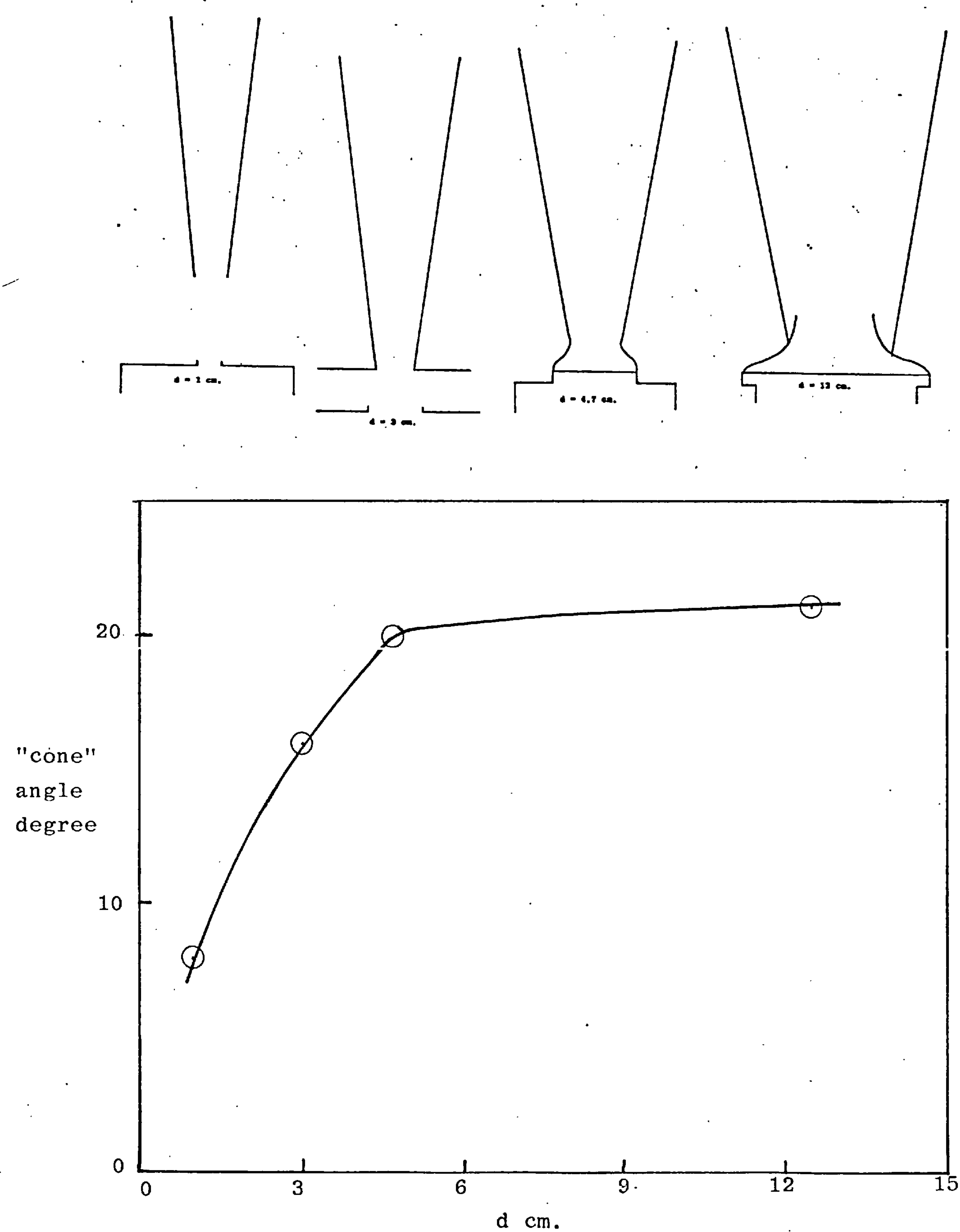

Figure 5.4   Variation of "cone" angle with diameter

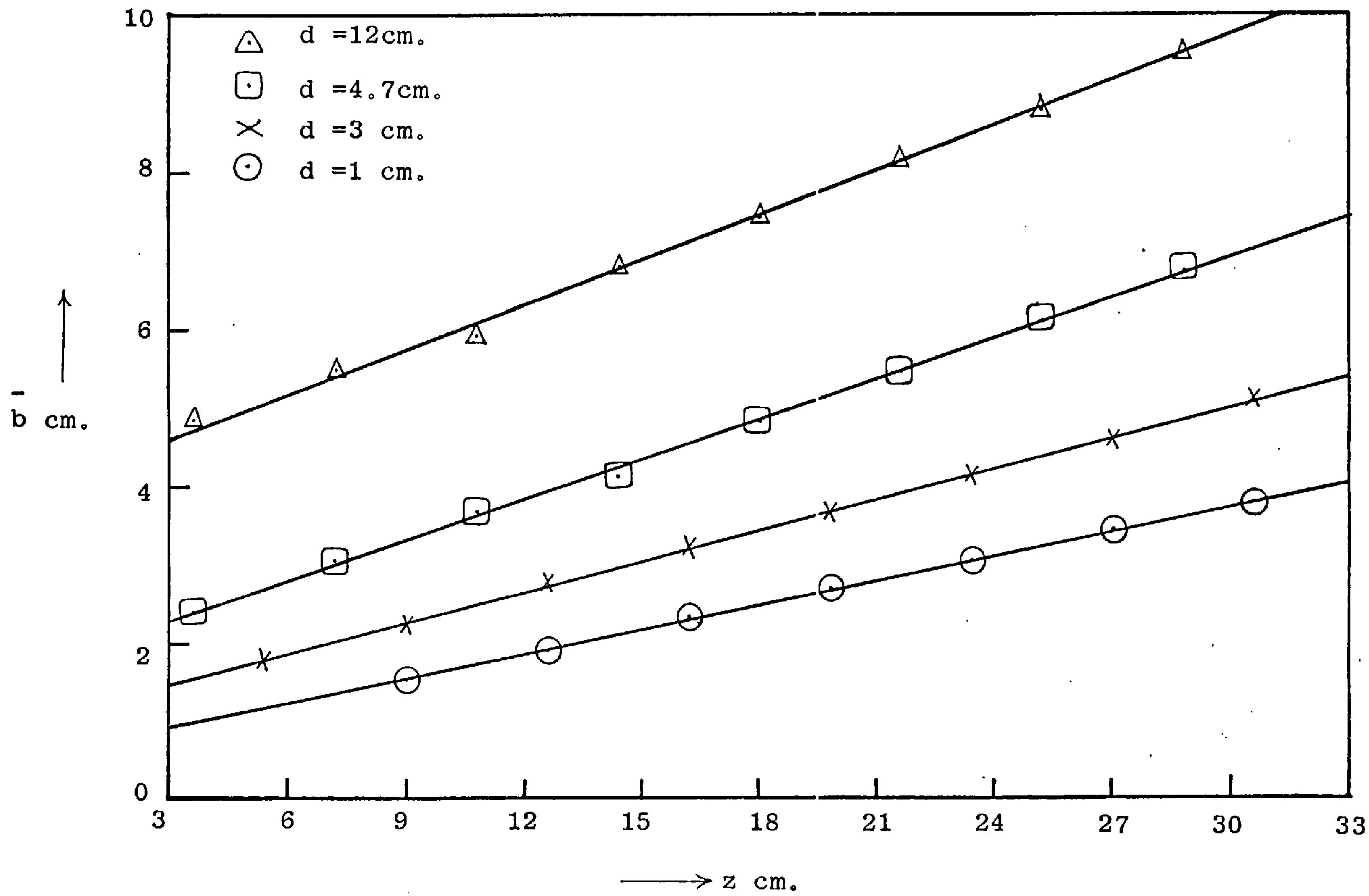

Figure 5,5 Variation of Column Width With Height respectively, we have

$$\bar{b} = 0.59 + 0.11z$$
$$\bar{b} = 1.11 + 0.13z$$
$$\bar{b} = 1.77 + 0.17z \qquad 5.3a.1$$
and
$$\bar{b} = 4.03 + 0.19z$$

or in general

$$\bar{b} = b_1 + b_2 z \qquad 5.3a.2$$

where the constants b_1 and b_2 both increase in value as the pool diameter increases. It is seen that for the solution of weakly buoyant plumes to be valid (equation 5.2a.24) the height z must be much greater than b_1/b_2. Equation 5.3a.2 then reduces to

$$\bar{b} = b_2 z \fallingdotseq (6/5)\alpha\ z \qquad 5.3a.3$$

The value of the entrainment coefficient α varies from 0.09 for a 1 cm. diameter pool to 0.16 for a pool diameter of 12 cm. (Escudier (62) found that the best value of α for a turbulent gas jet plume is 0.13).

5.3b <u>Visible Flame Heights</u>

Atallah (74) has studied the variation of flame height with pool size. He estimated the flame heights both visually and photographically. He took long exposure as well as 'instantaneous' photographs of the flame. However, he found a large scatter in data because a long exposure photograph gives the maximum flame height and an 'instantaneous' photograph cannot be a representative of the average flame height of a fluctuating flame. Steward (59) has derived an equation which relates the visible flame height to the fuel burning rate, heat of combustion of the fuel, the jet entrainment coefficient, stoichiometric air to fuel ratio of the fuel and the size of the fuel source. He measured the visible height of the flame simply by visual observation of the fluctuations of the flame above and below a marker. However, it is found that in the case of liquid pool fires, this process of observation can result in an error of up to 50%. Furthermore, it is found that there is no unique value of the visible flame height and only a mean value can be specified.

It was found that for ethanol pool flames of all burner diameters, rhythmic pulsation of the flames was observed. The pulsation cycle starts with an expansion of the flames near the base of the fire and is followed by a sudden collapse of these flames toward the centre of the fire. A flame bulge then travels upward to the flame tip in an even, wavelike motion. Expansion of the lower part of the flames starts the cycle again. The pulsating frequency tends to decrease with increasing pool diameter and at d = 10 cm., the frequency is around three per second.

Direct flame cinematography was used and measurements of the flame heights were performed every eighth of a second. Thus a statistical distribution of flame heights was obtained for each burner diameter. Figures 5.6 a and b show two such direct flame photographs separated by eighth of a second in time. The pool diameters were ten and three centimetres in both cases.

Figure 5.7 shows probability distribution curves of visible flame heights expressed as a multiple of the pool radius for pool diameters ranging from 1.5 to 10 cm.. The variation of the mean flame height versus pool diameter is shown in Figure 5.8. It is seen that the relative flame height decreases as the diameter of the pool increases. This is attributed to the increasing turbulence effects as the pool diameter increases. From a least square fit, it is found that

$$h/d = 8.25 - 2.34d + 0.18d^2 \qquad 5.3b.1$$

5.4 Velocity, Turbulence Intensity and Laser Flicker Frequency Distributions

In this section, the result of measurements of velocity and turbulence intensity distributions within fire plumes above ethanol fires with pool diameter ranging from 1.3 to 12.5 cm., utilizing the technique already described in section 4.7 will be presented. Calculated values of laser flicker frequencies from these measurements will be given as well as the effect on plume velocity induced by a horizontal ceiling.

(a)

(b)

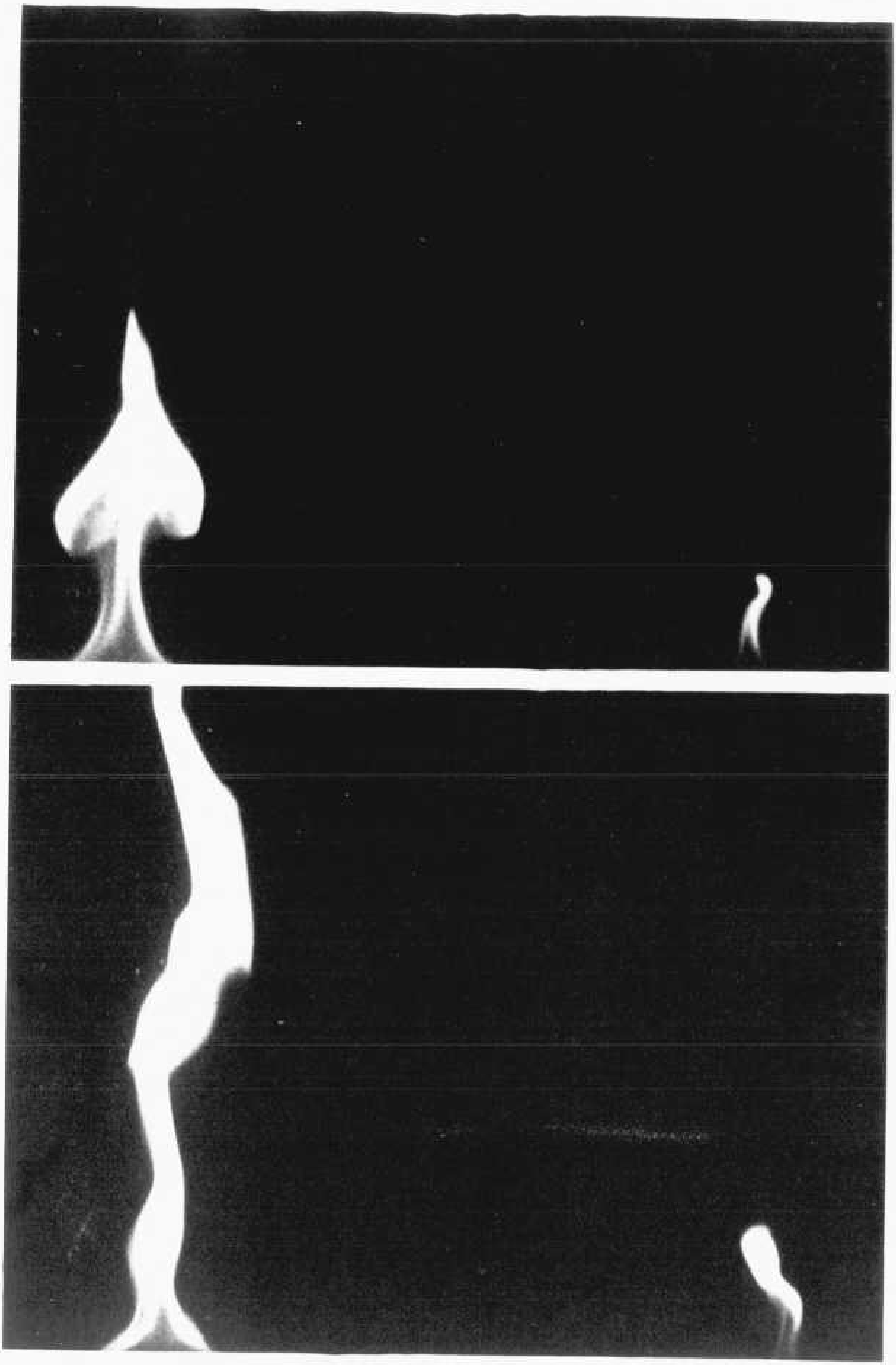

Figure 5.6 a&b Direct flame photographs of 3 and 10 cm.- diameter pool fires;(a) & (b) are successive photographs taken at 1/8 second interval.

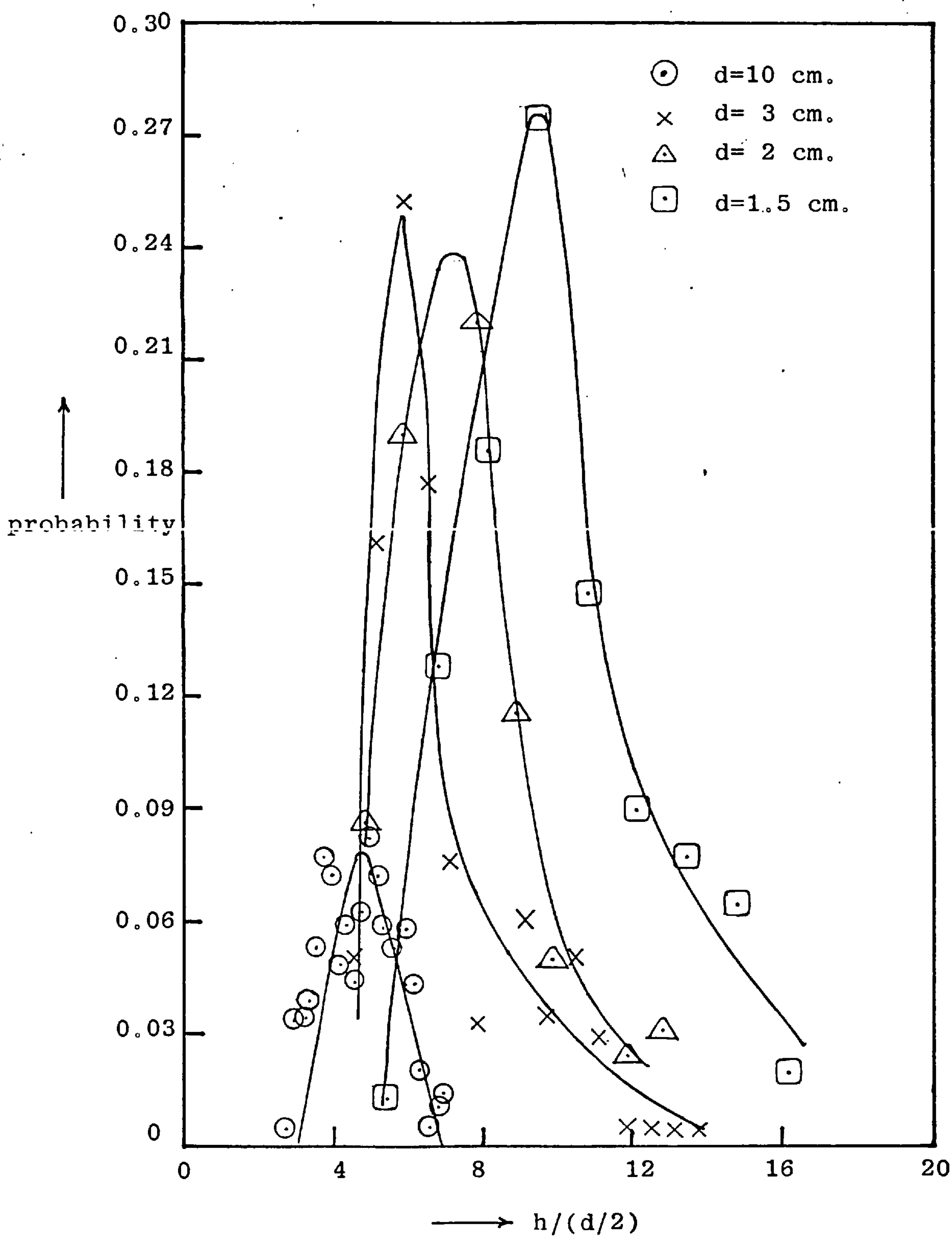

Figure 5.7 Probability Distributions of Visible Flame Heights

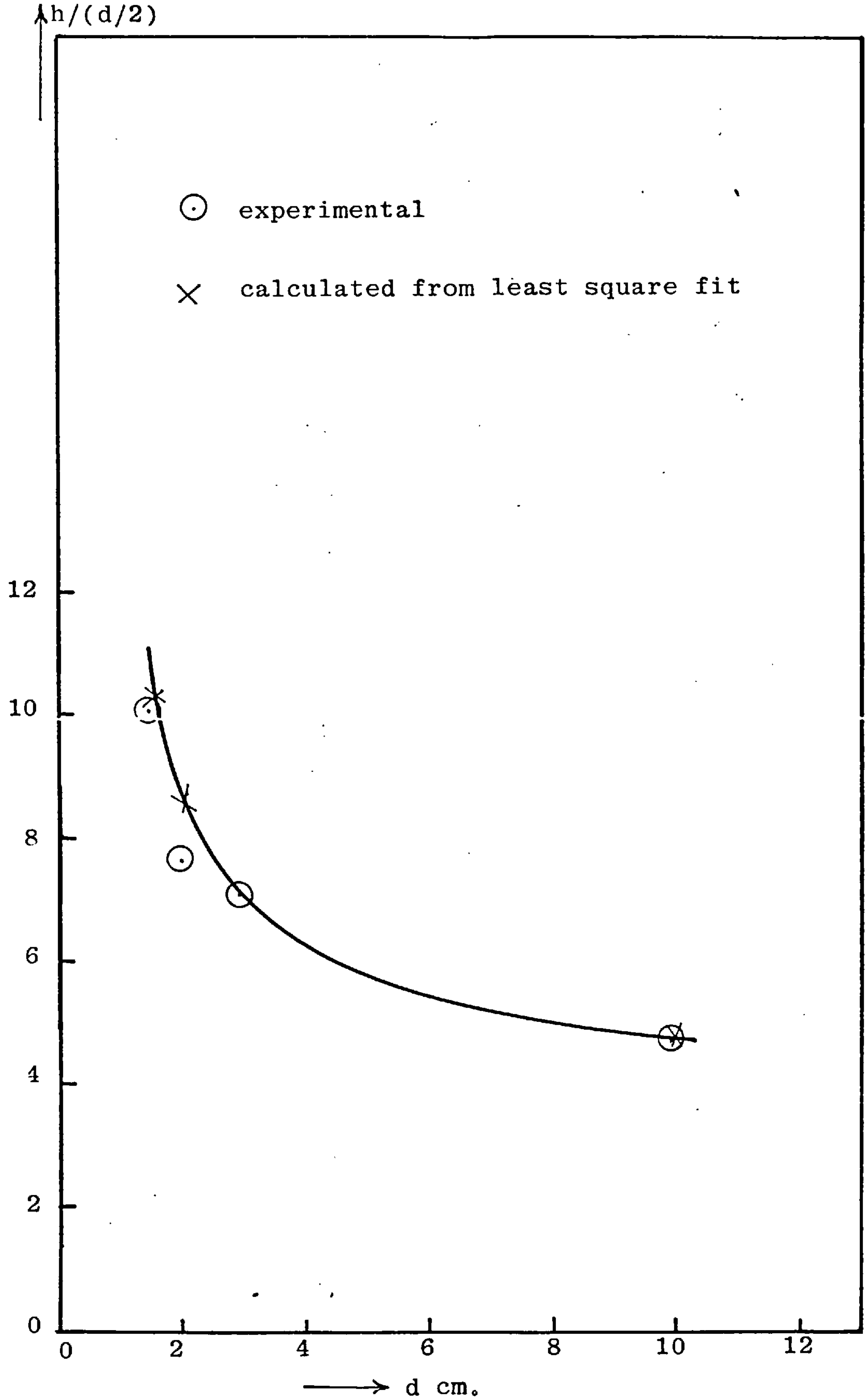

Figure 5.8 Plot of Relative Flame Height Versus Pool Diameter

5.4a Unconstrained Plumes

Cine records were obtained of the interrupted shadow interferograms of the fire plume at intervals of ten centimetres above the burning pool. These were analysed by first measuring the progress of identifiable features in each region and drawing the result of local velocity vectors on a tracing paper. The average velocity vector across the whole plume within this height interval was obtained from these results. The data was then transferred onto paper tapes and then onto punched cards. A computer program (Fig. 5.9) was written to compute the average horizontal and vertical velocities as well as the turbulence intensities. This procedure was repeated for each height interval. Figure 5.10 is an example of such local velocity vectors for plume originated from a 4.7 cm. diameter pool burner at an altitude between 10 and 20 cm.. In order to find out the variation of velocity across the plume, Figure 5.10 was arbitarily divided horizontally into seven zones and the average resultant velocity calculated for each zone. The result is plotted in Figure 5.11, which shows that the velocity distribution horizontally across the plume is Gaussian. The corresponding turbulence intensity distribution is shown in Figure 5.12. Figure 5.13 shows the change in the ratio of the vertical to horizontal velocity component across the plume. As is to be expected from entrainment considerations, it

```
                  PROGRAM PLUME(INPUT,OUTPUT,TAPE5=INPUT,TAPE6=OUTPUT)
000002            DIMENSION JA(400),JB(400),JC(400),JD(400),JE(400),JF(400)
000002            DIMENSION VX(400),VY(400),V(400)
          C       J5,N=61
000002            N=61
000003            DO 10 I=1,N
000005            READ (5,1000) JA(I),JB(I),JC(I),JD(I),JE(I),JF(I)
000024       1000 FORMAT (I5,5I6)
000024            WRITE(6,2000) I,JA(I),JB(I),JC(I),JD(I),JE(I),JF(I)
000046       2000 FORMAT(7I10)
000046         10 CONTINUE
          C       CALCULATE INDIVIDUAL VELOCITIES
000051            C1=0.24
000052            C2=0.14
000054            WRITE(6,3000)
000057       3000 FORMAT(1H1,22H X VELOCITY COMPONENT,8X,22H Y VELOCITY COMPONENT
                 1,8X,20H RESULTANT VELOCITY )
000057            DO 11 I=1,N
000062            VX(I) =ABS(FLOAT(JC(I)-JA(I))*C1)
000065            VY(I) =ABS(FLOAT(JF(I)-JD(I))*C2)
000072            V(I)=SQRT(VX(I)*VX(I)+VY(I)*VY(I))
000101            WRITE(6,3001)I,VX(I),VY(I),V(I)
000115       3001 FORMAT(I6,F17.2,F30.2,F28.2)
000115         11 CONTINUE
          C       CALCULATE SUM OF VELOCITIES
000120            SX=0
000120            SY=0
000121            SV=0
000122            DO 12 I=1,N
000131            SX=SX+VX(I)
000132            SY=SY+VY(I)
000134            SV=SV+V(I)
000135         12 CONTINUE
          C       CALCULATE AVERAGE VELOCITIES
000136            AVX=SX/N
000140            AVY=SY/N
000142            AV=SV/N
000145            WRITE(6,4000) AVX,AVY,AV
000156       4000 FORMAT(1X,6HAVX = ,F6.2,6HAVY = ,F6.2,5HAV = ,F6.2)
          C       CALCULATE SUM OF VELOCITY SQUARES
000156            SXSQ=0
000157            SYSQ=0
000157            SVSQ=0
000160            DO 13 I=1,N
000167            SXSQ=SXSQ+VX(I)*VX(I)
000171            SYSQ=SYSQ+VY(I)*VY(I)
000172            SVSQ=SVSQ+V(I)*V(I)
000174         13 CONTINUE
          C       CALCULATE MEAN OF VELOCITY SQUARES
000175            ASQVX=SXSQ/N
000177            ASQVY=SYSQ/N
000201            ASQV=SVSQ/N
          C       CALCULATE TURBULENCE INTENSITIES
000203            TIVX=(SQRT(ASQVX-AVX*AVX))/AVX
000210            TIVY=(SQRT(ASQVY-AVY*AVY))/AVY
000216            TIV =(SQRT(ASQV-AV*AV))/AV
000225            WRITE(6,5000) TIVX,TIVY,TIV
000236       5000 FORMAT(1X,8H TIVX = ,F4.2,8H TIVY = ,F4.2,7H TIV = ,F4.2)
000236            STOP
000240            END

UNUSED COMPILER SPACE
015200
```

Figure 5.9 A comuter program for calculating turbule velocities and turbulence intensities

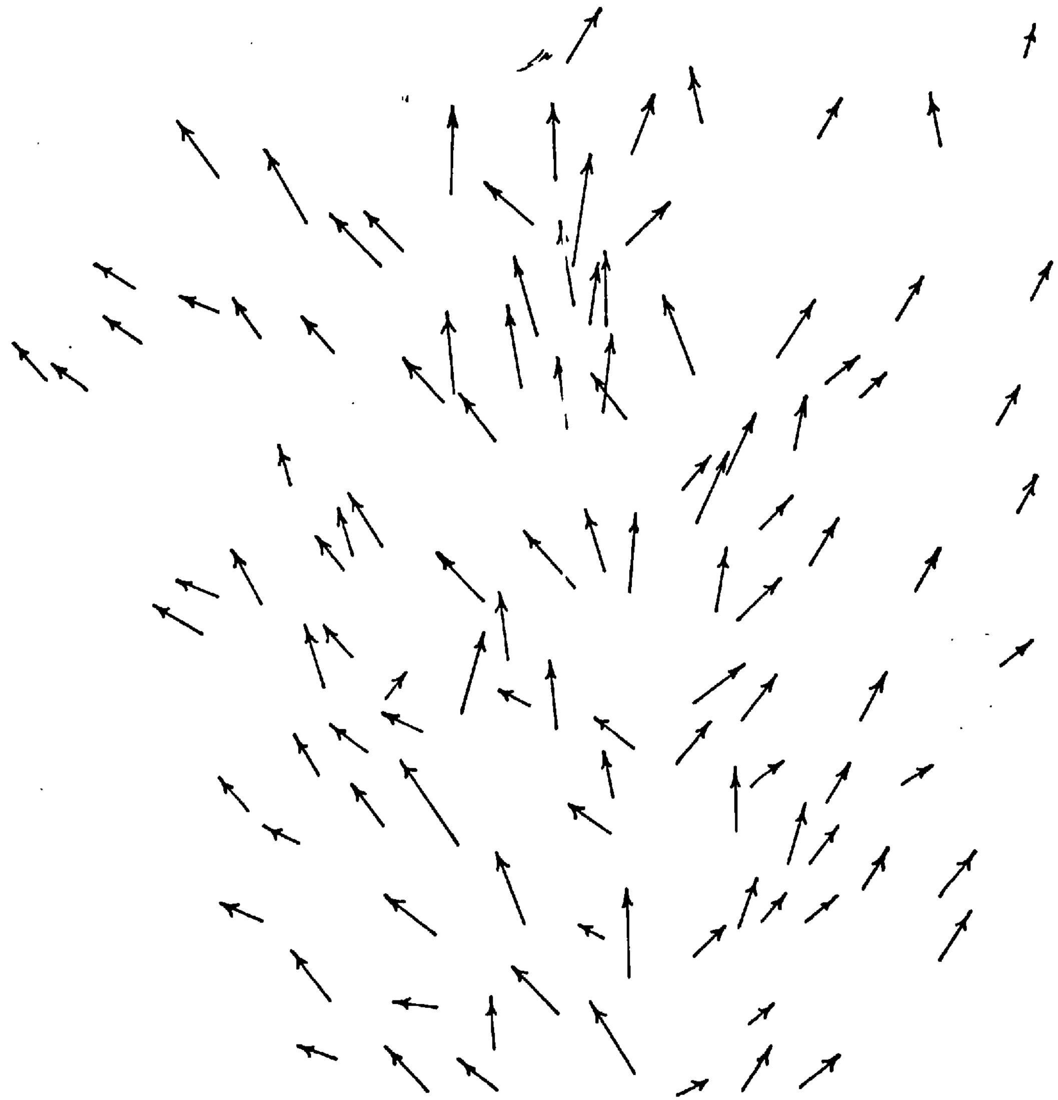

Figure 5.10 Local Velocity Vectors

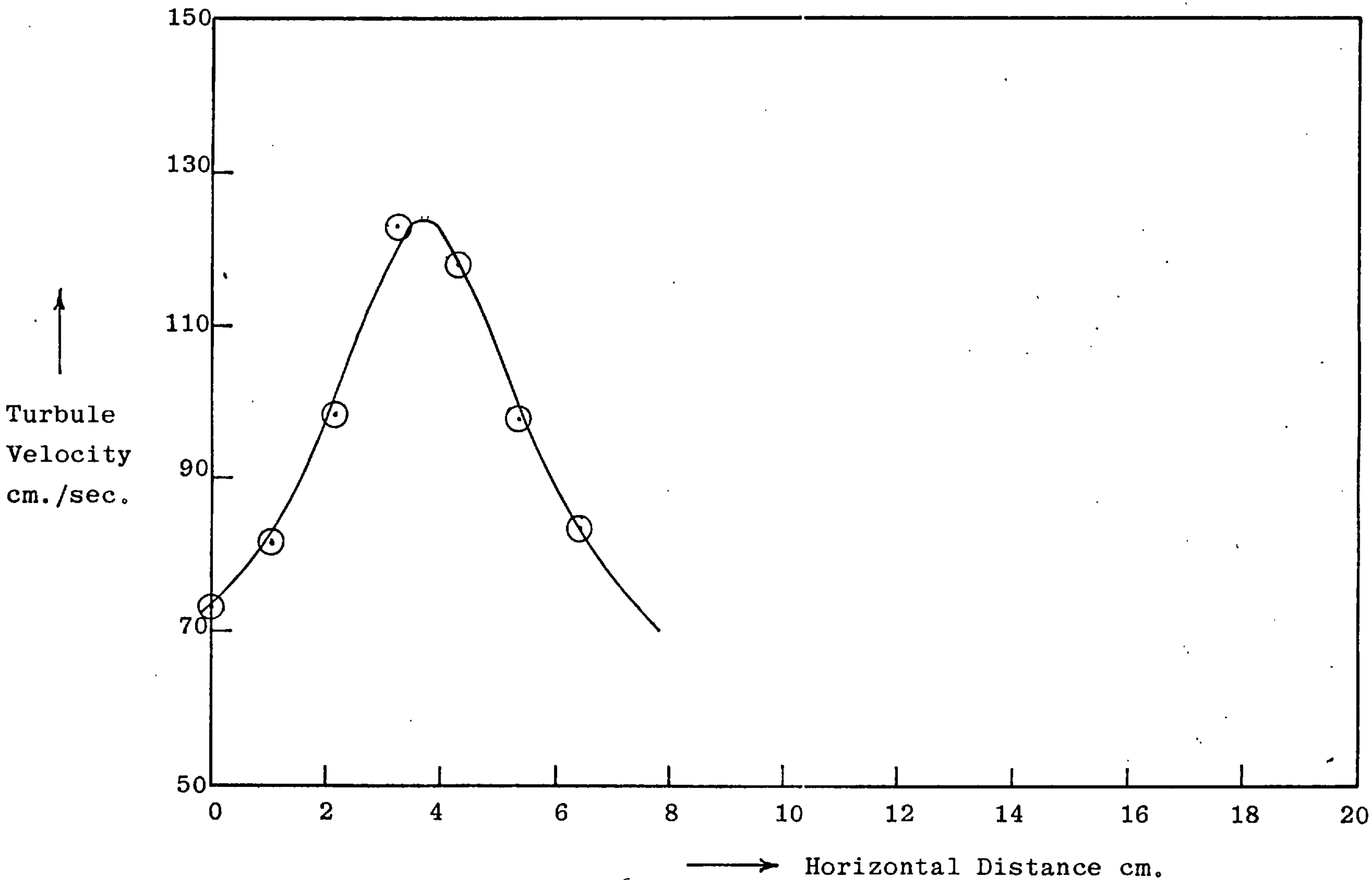

Figure 5.11 Horizontal Distribution of Turbule Velocities

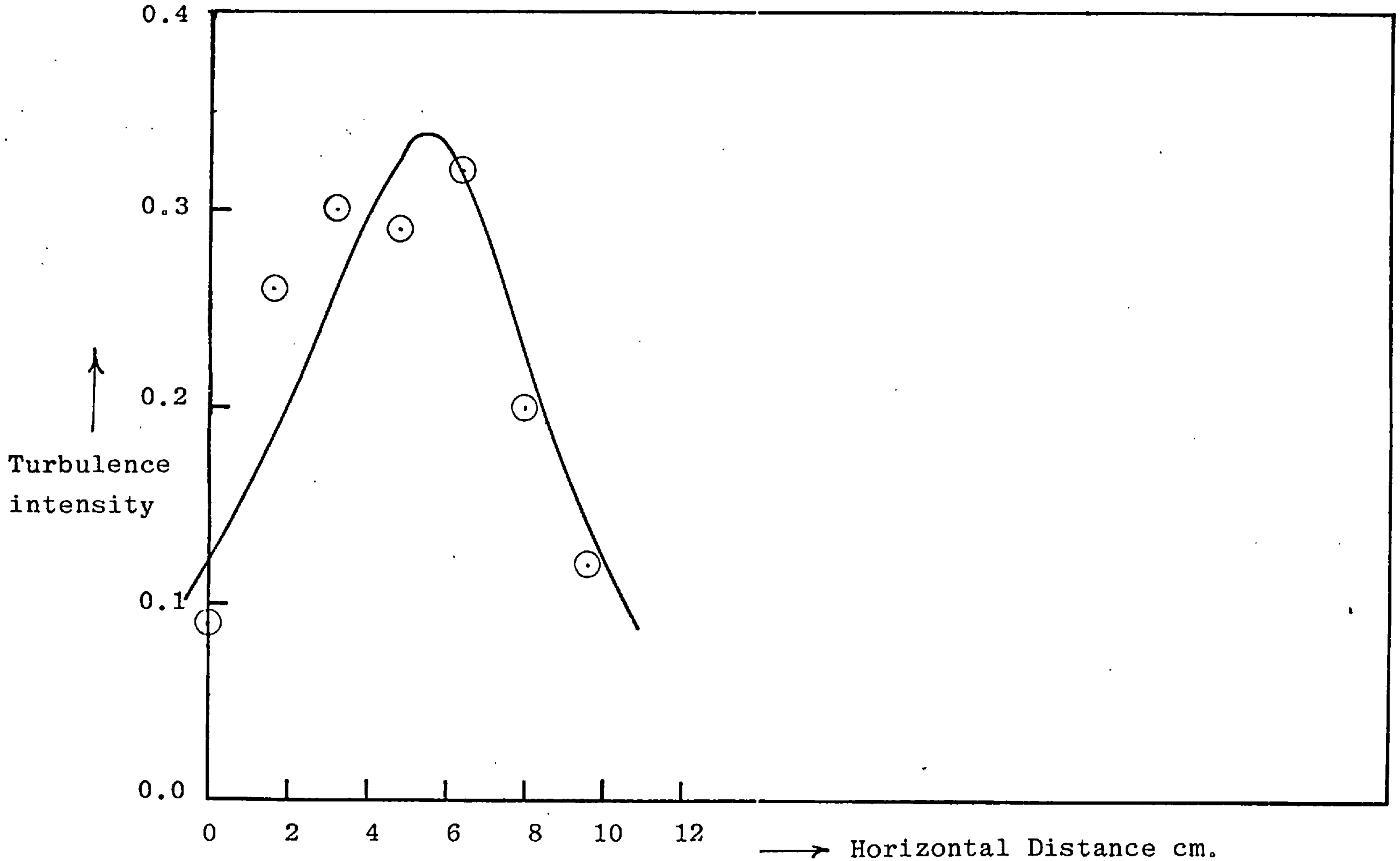

Figure 5.12 Turbulence intensity distribution horizontally across a fire plume

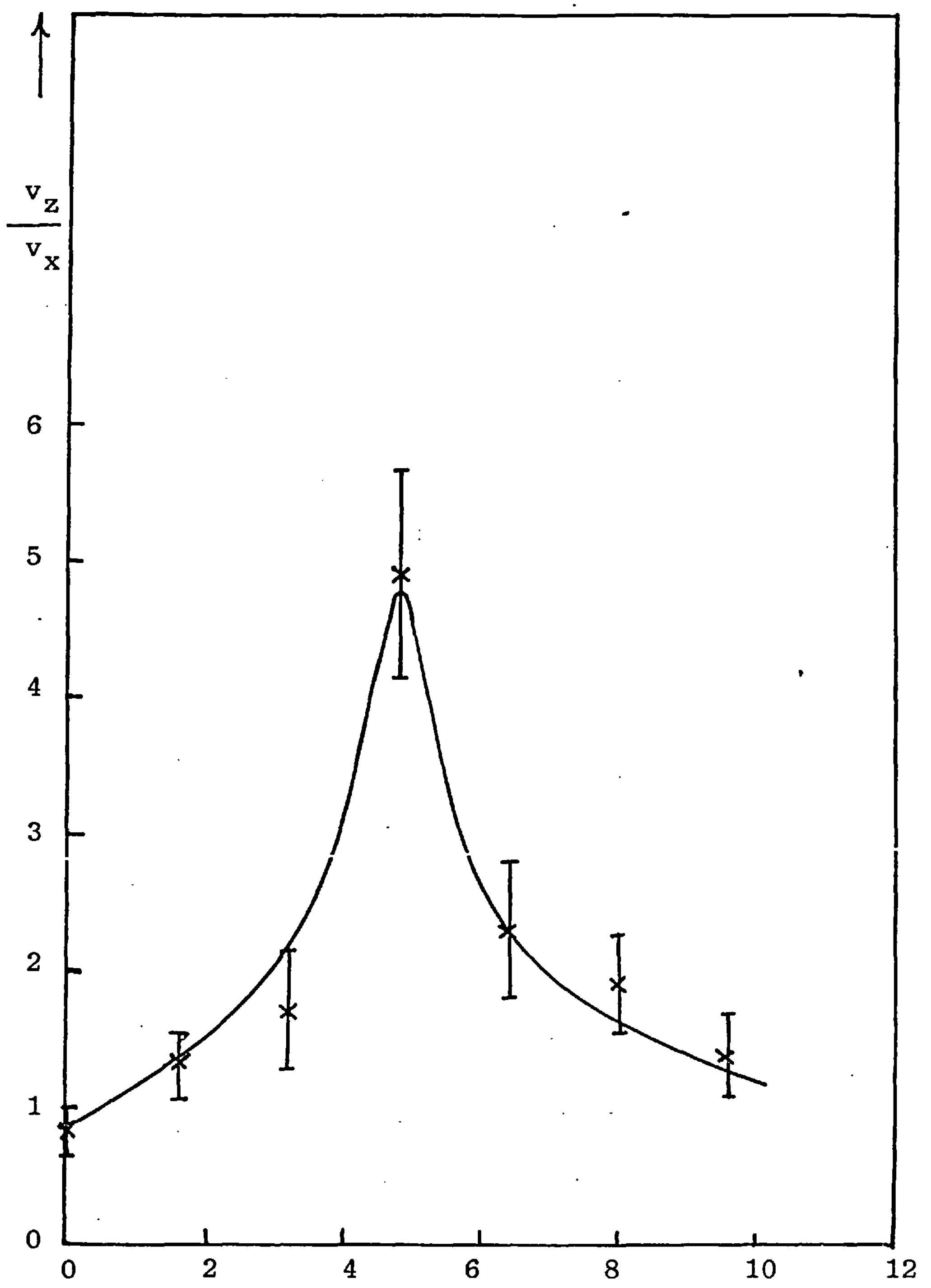

Figure 5.13 Change in the ratio of the vertical to horizontal velocity component across the plume

is found that this ratio decreases towards the plume edge.

The average vertical velocity distributions for different pool diameters are shown in Figure 5.14. Each point plotted on this curve represents an average of around one hundred local velocity values. A plot of log AV_z against log z us shown in Figure 5.15. The most interesting feature of this graph is that after reaching the maximum velocity, the velocity for all pan diameters decreases as :

$$AV_z \propto z^{-1/3} \qquad 5.4a.1$$

This is in exact agreement with that expected from the weak buoyant plume theory (section 5.2a). In order to determine the dependence of the average upward plume velocity on the pool diameter d, logarithmic plots of AV_z versus d for several values of z (the values of z are chosen in the weakly buoyant regions) are depicted in Figure 5.16. From these lines, it is established that

$$AV_z \propto d^{1/3} \qquad 5.4a.2$$

Therefore, combining equations 5.4a.1 and 5.4a.2, we have:

$$AV_z \propto (d/z)^{1/3} \qquad 5.4a.3$$

This relationship is borne out very clearly in Figure 5.17,

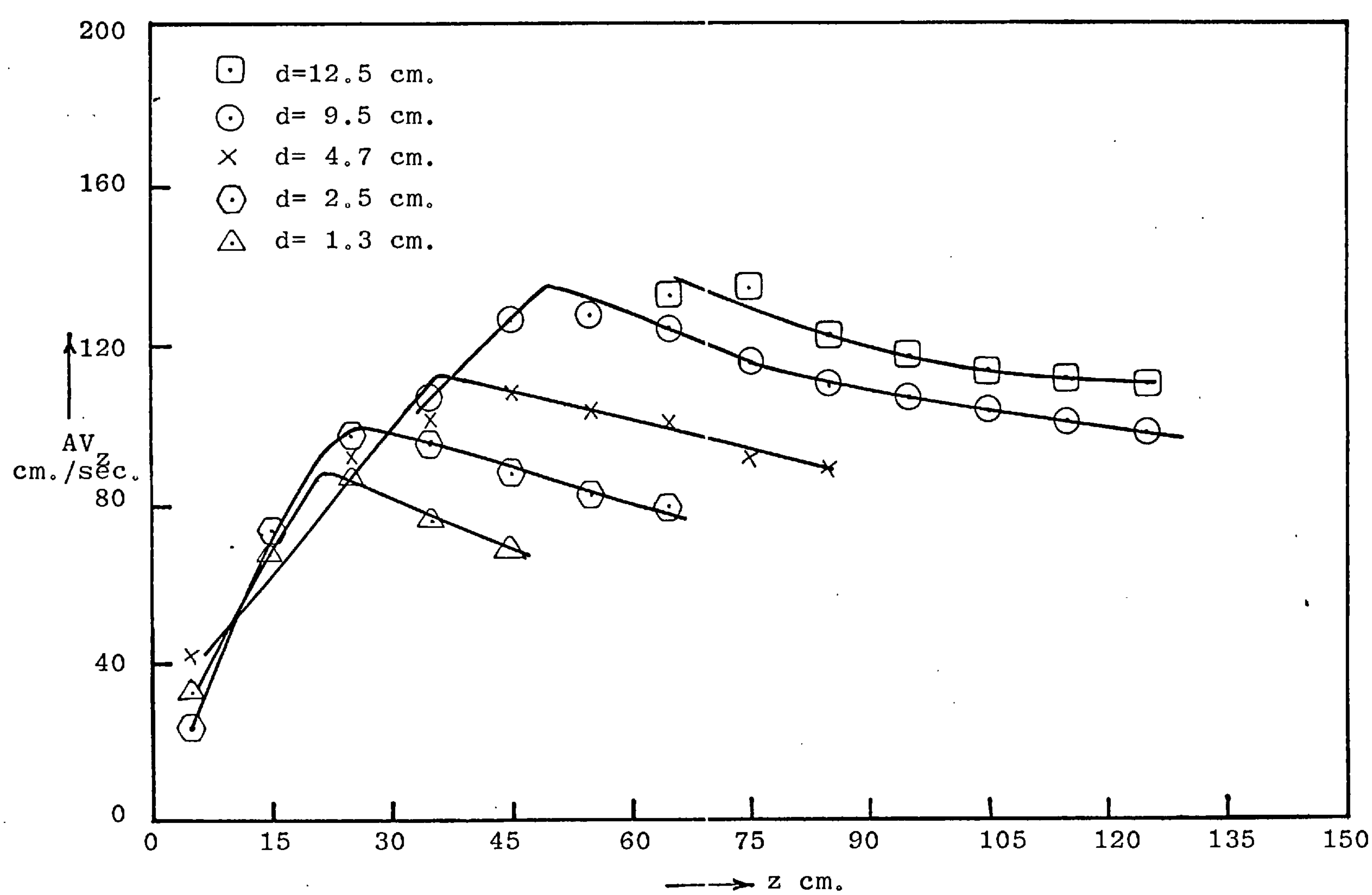

Figure 5.14 Distributions of vertical plume velocity

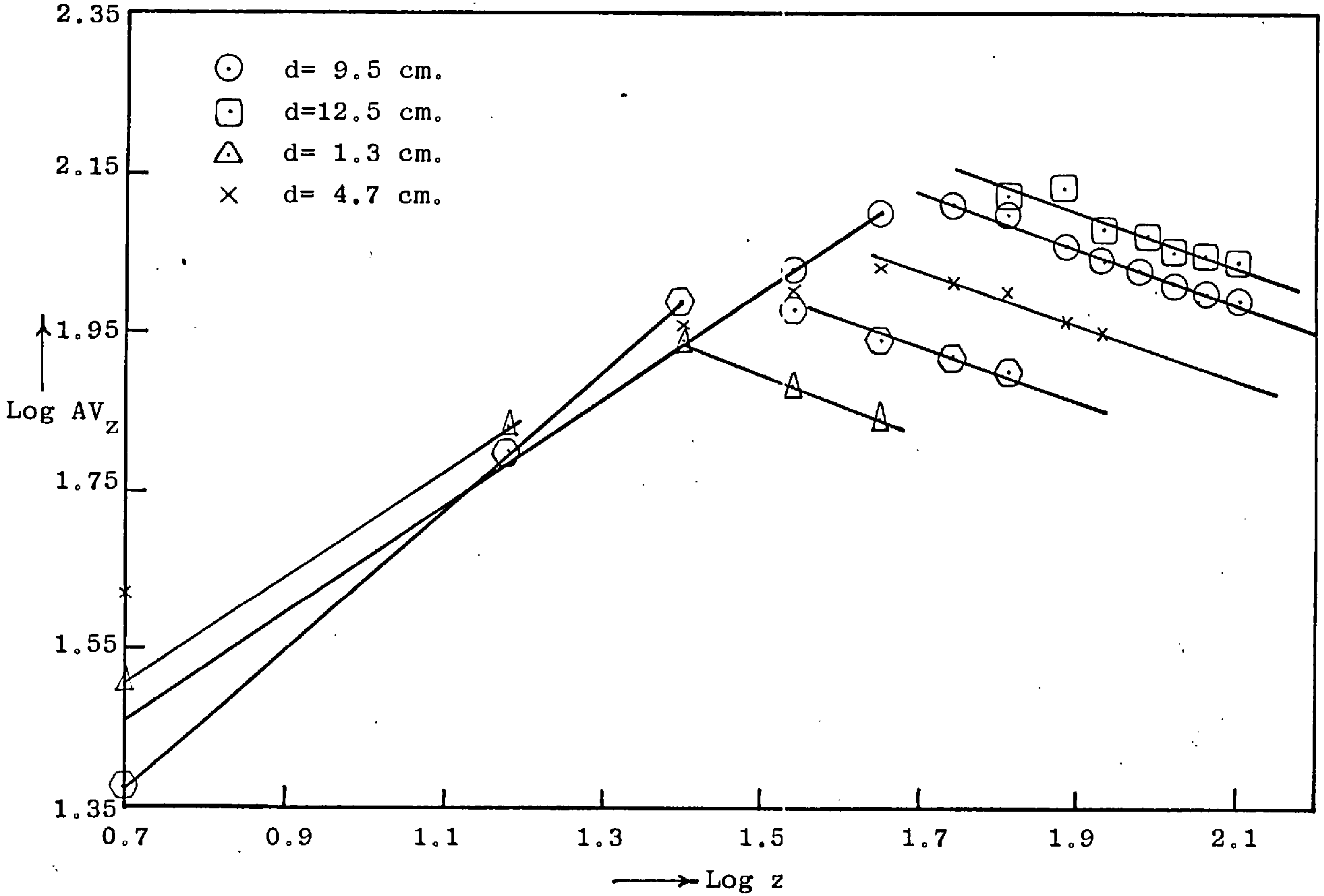

Figure 5.15 Logarithmic plot of vertical plume velocity versus height

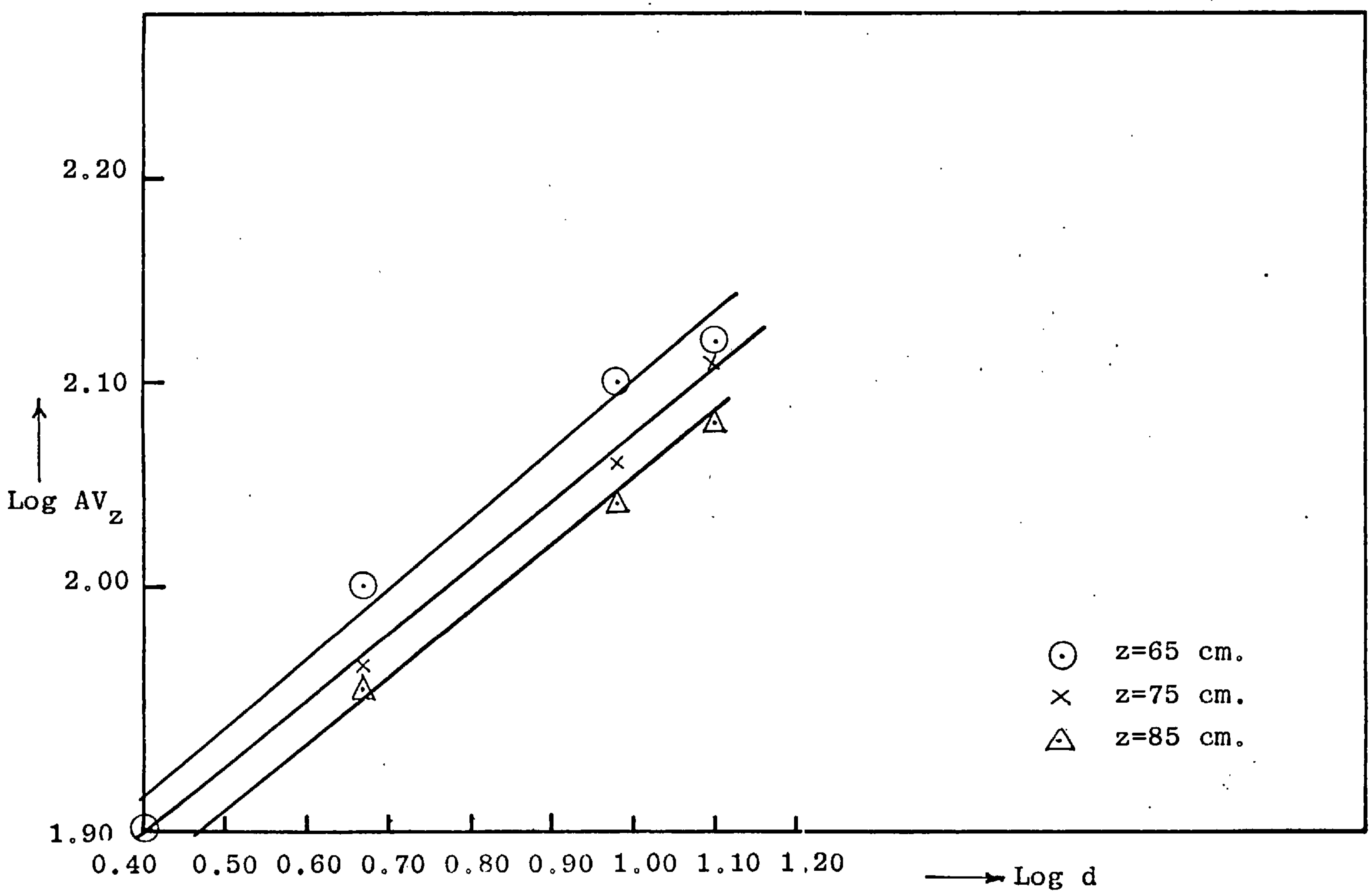

Figure 5.16 Logarithmic plot of vertical plume velocity versus pool diameter

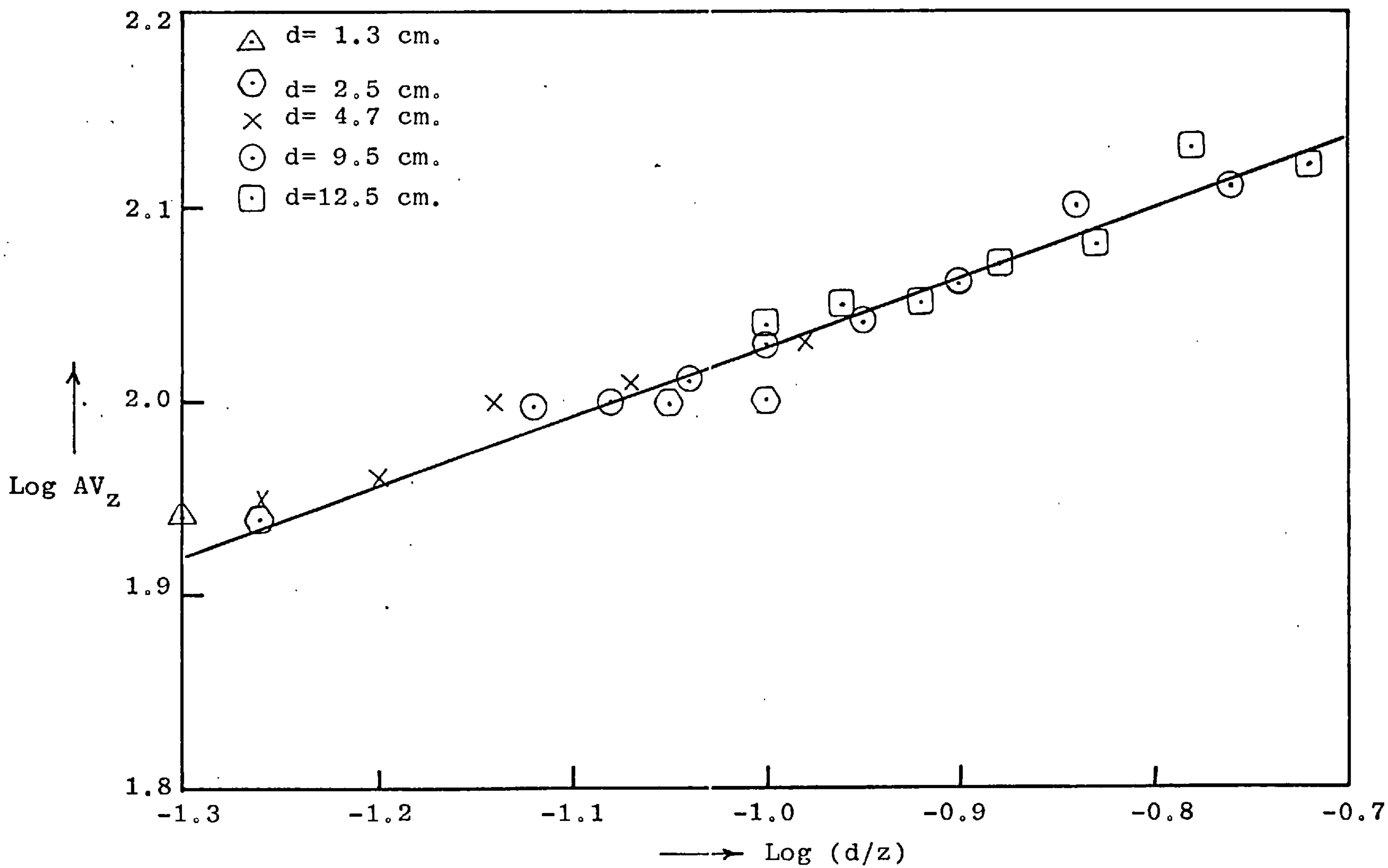

Figure 5.17 Logarithmic plot showing the inverse third power dependence of the average upward plume velocity with height

which is a plot of $\log AV_z$ against $\log(d/z)$ for five different values of d. The variation of the average horizontal velocity with height, the vertical and horizontal turbulence intensity distributions are shown in Figures 5.18, 5.19 and 5.20 respectively.

The results were used considered in terms of the interaction with a laser fire detector. If the horizontal laser beam passes through any point of the fire plume, in regions where the average distance $\bar{L}$ between turbule shadows on the record is greater than the mean characteristic scale $\bar{l}$, of the trubules, the mean laser flicker frequency in the vertical direction would be :

$$\bar{\eta} = AV_z/\bar{l} \qquad 5.4a.4$$

On the other hand, when $\bar{L} < \bar{l}$, then :

$$\bar{\eta} = AV_z/\bar{L} \qquad 5.4a.5$$

From the interrupted shadowgrams, it is clear that for the plumes under consideration, equation 5.4a.5 is appropriate because the width of the plume over which the beam intergrates is >>l. The deduced flicker frequency variation with height for several values of pool diameters is shown in Figure 5.21 (the value of $\bar{L}$ was obtained by measuring L for several frames and an average value taken). To gain some insight into the

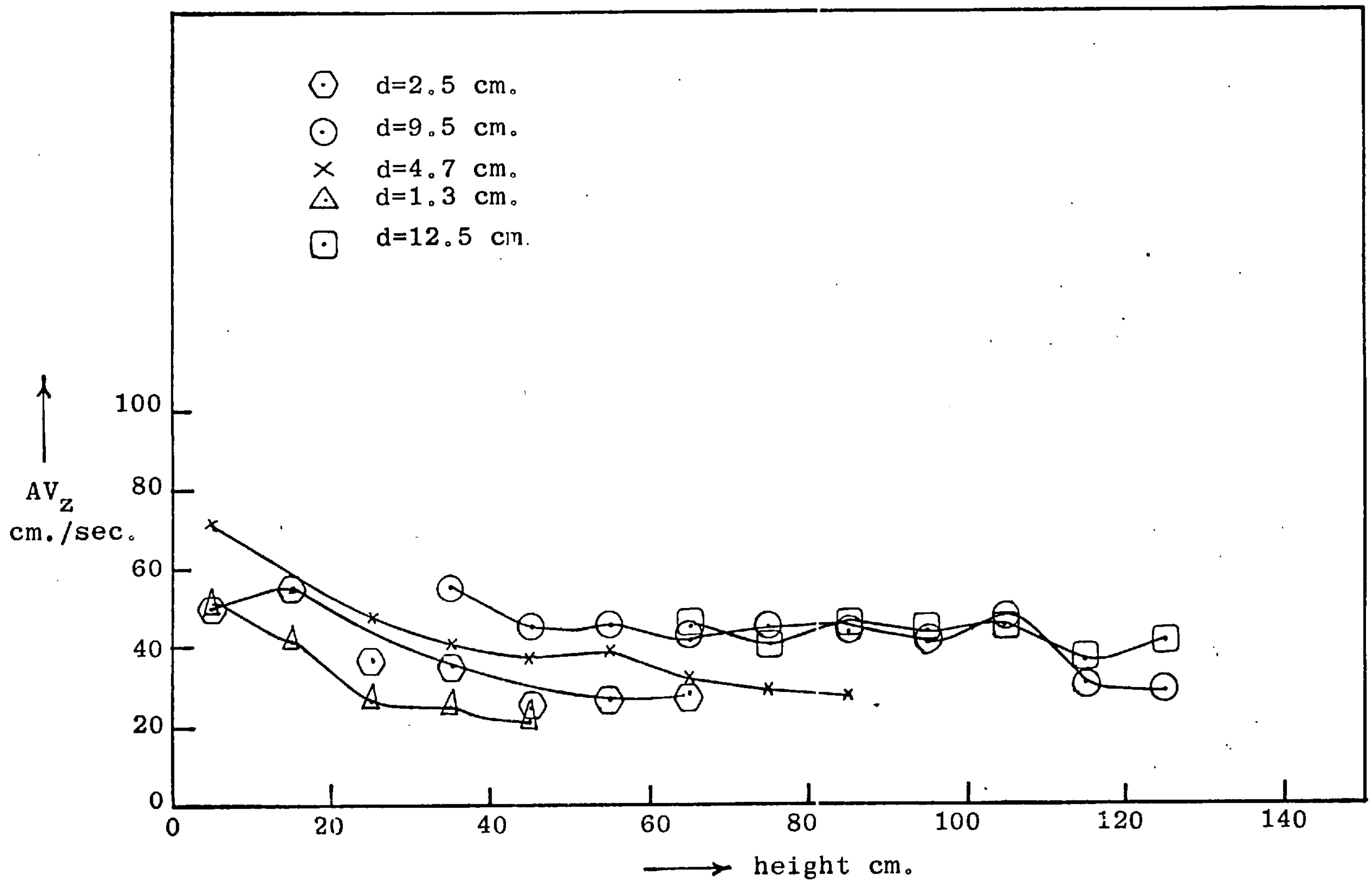

Figure 5.18 Dependence of averge horizontal turbule velocity with height

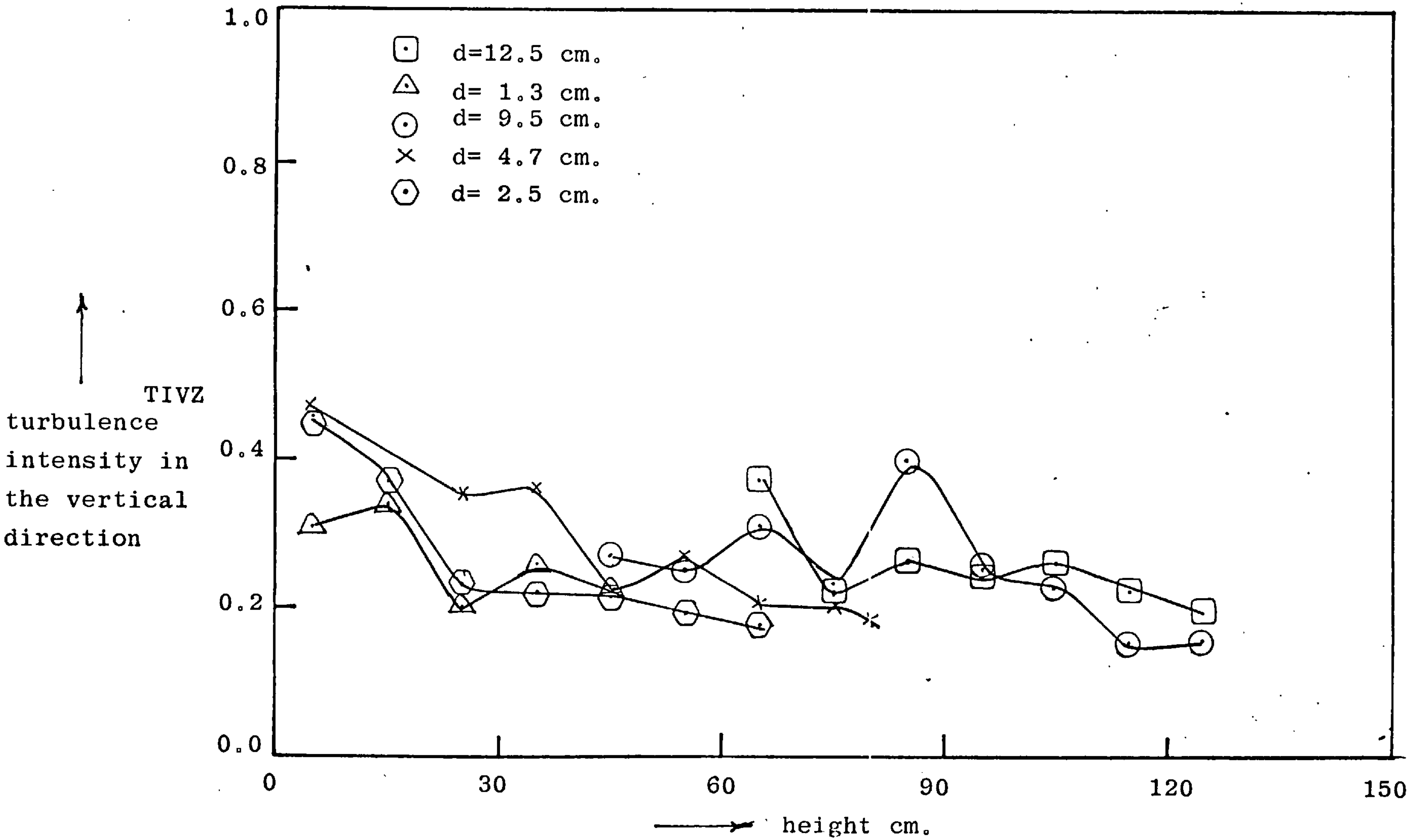

Figure 5.19 Vertical turbulence intensity distributions

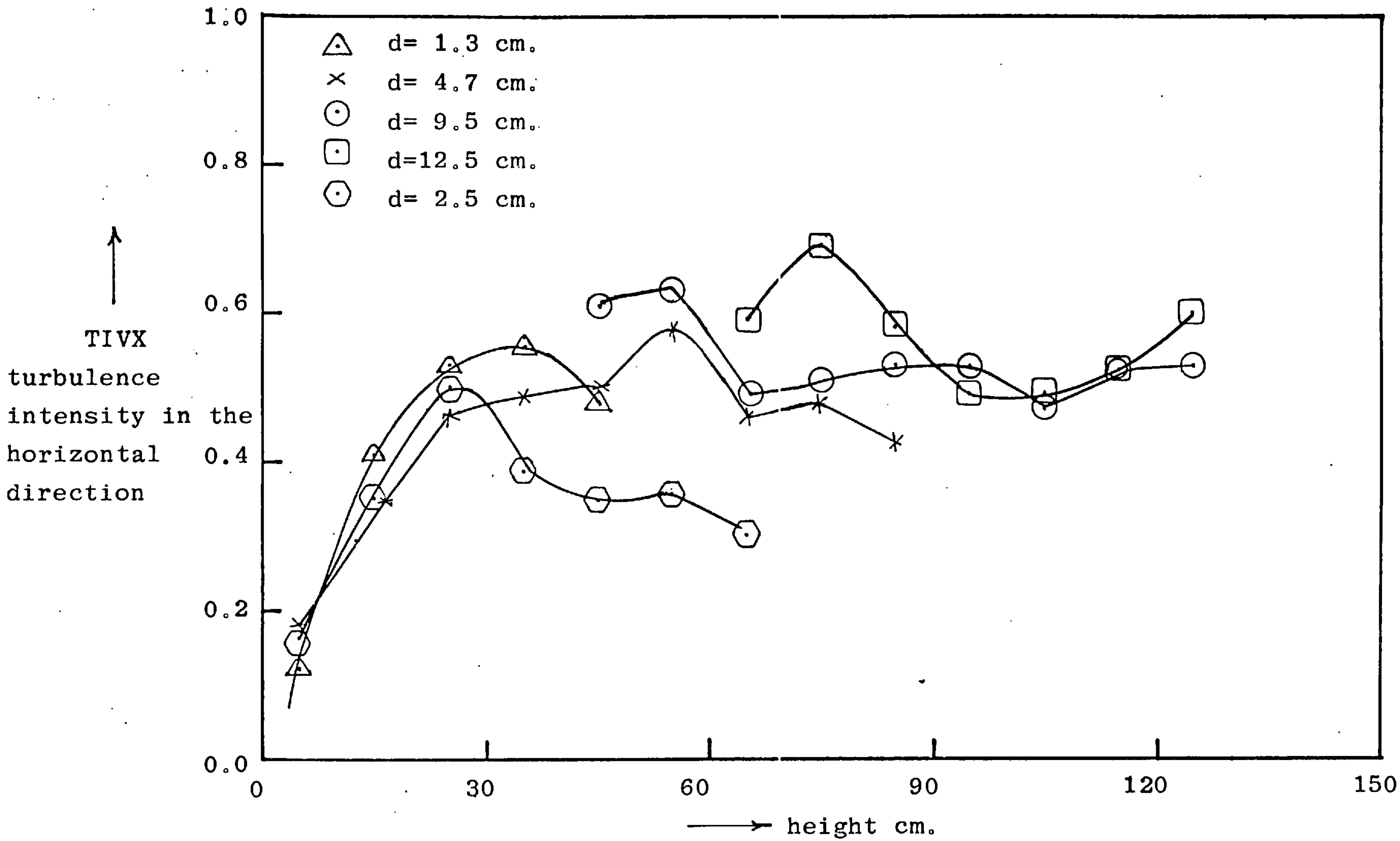

Figure 5.20   Horizontal turbulence intensity distributions

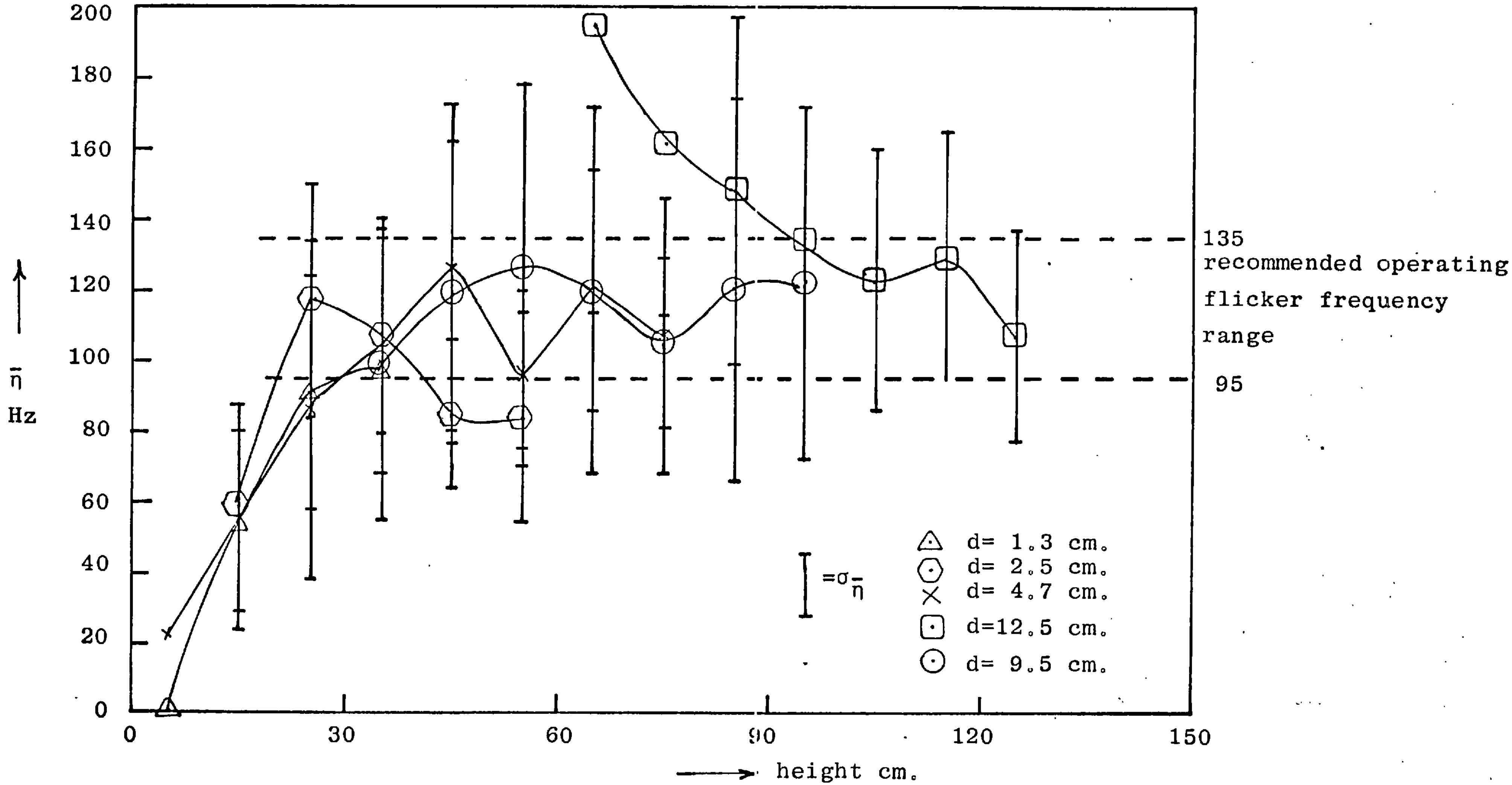

Figure 5.21 Variation of flicker frequencies with height above pool fire source

magnitude of the flicker frequency spread, we can calculate the standard deviation $\sigma_{\bar{\eta}}$. It is easily shown that :

$$\sigma_{\bar{\eta}}^2 = \bar{\eta}^2 \{(\sigma_{AV_z}/AV_z)^2 + (\sigma_{\bar{L}}/\bar{L})^2\} \qquad 5.4a.6$$

This information is plotted in Figure 5.22, which shows the values of $\sigma_{\bar{\eta}}$ at different heights for various burner diameters. These values of $\sigma_{\bar{\eta}}$ are incorporated in Figure 5.21 in such a way that there is a probability of 0.68 that the flicker frequency in any instance lies within the 'bar'. It is estimated that for the sizes of pool fires studied and for the height interval considered, the optimum operating frequency range for a ceiling-mounted laser fire detector is 95 to 135 Hertz.

5.5 The Interaction Between Fire Plumes and a Horizontal Ceiling

For fires in an enclosed space, for example, in a warehouse, the properties of the fire plume will be affected by the ceiling and this may be important in the design of fire detectors. Torrance and Rocket (75) have obtained numerical solutions for the flow field generated within an enclosure by a heat source at the bottom. The room model used in their study was a vertical cylinder of height, a, and radius, b, with the fire simulated by a small heat source in the centre of the floor. They eliminated the possibility of the inclusion of any

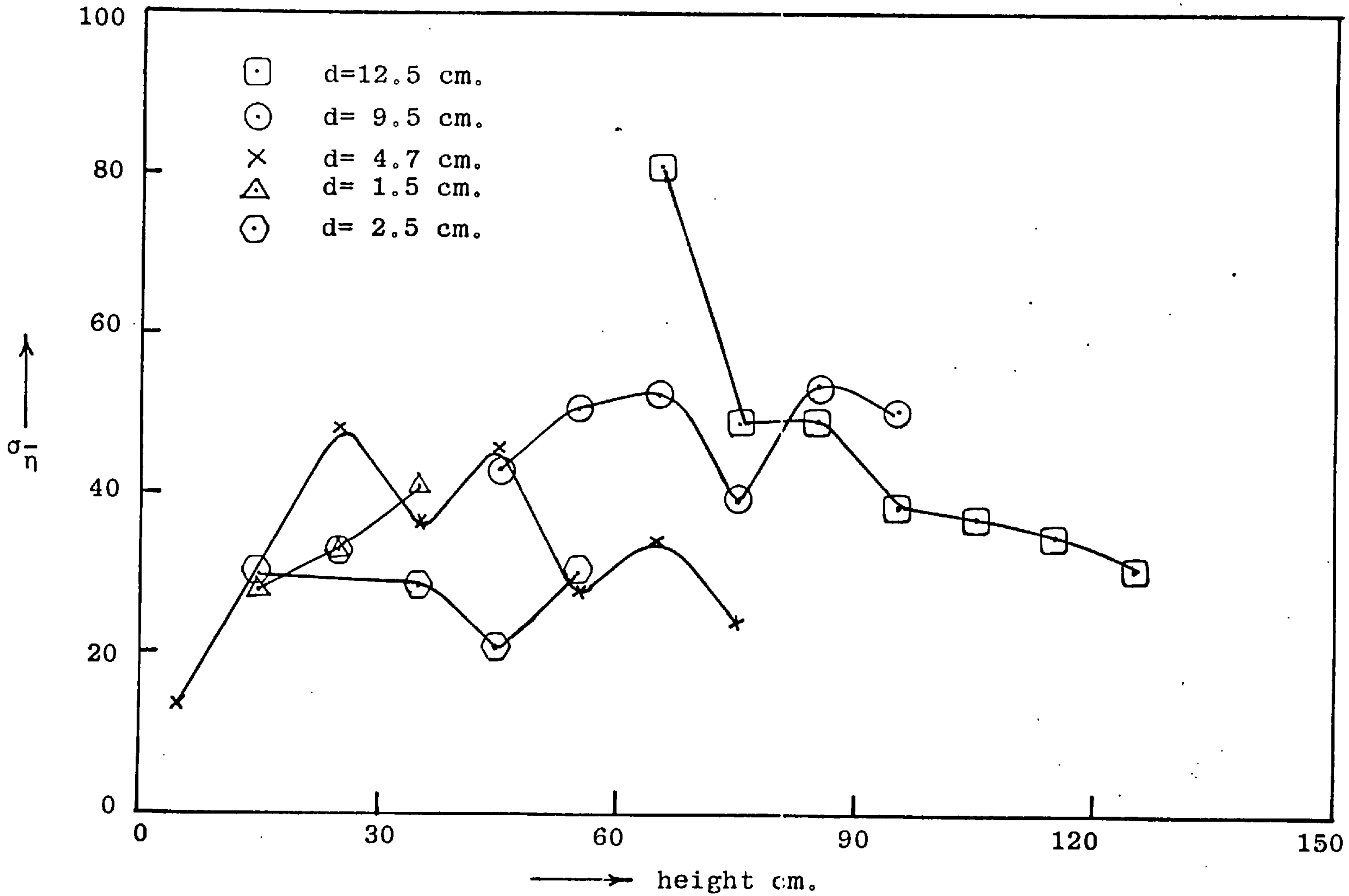

Figure 5.22 Plot of $\sigma_{\bar{\eta}}$ versus height

turbulent flow in their computation by assuming a two-dimensional, axisymmetric and totally laminar plume. However, in practice, the plume is certainly turbulent and the present aim was to study experimentally the effect of a ceiling on the velocity distribution of convective pool fire plumes.

The technique of triple-exposure cinematography was again employed, the test object being a 4.7 cm. diameter ethanol pool fire with a steel 'ceiling' of dimension 27 X 21 X 0.1 $cm.^3$ mounted at a distance of 22 cm. above the pool burner (Fig. 5.23). Figures 5.24a and b are triple exposure shadowgraphs of the plume, and the other half of the plume are just its mirror image. The velocity vectors and the plume boundary (obtained from an average of many shadowgraphs) are shown in Figures 5.25a and b respectively. The dotted lines arbitarily divide the plume into six regions. The average resultant velocity was computed for each region and Figure 5.26 depicts the turbule velocity distribution along the ceiling (c.f. Fig. 5.11, which is the velocity distribution in the absence of the ceiling). A least square fit of these points reveals that :

$$^{A}V_{R} = 108.92 - 9.43\ x + 0.38\ x^{2} \qquad 5.5.1$$

The corresponding turbulence intensity distribution is shown in Figure 5.27.

From these result an approximate temperature

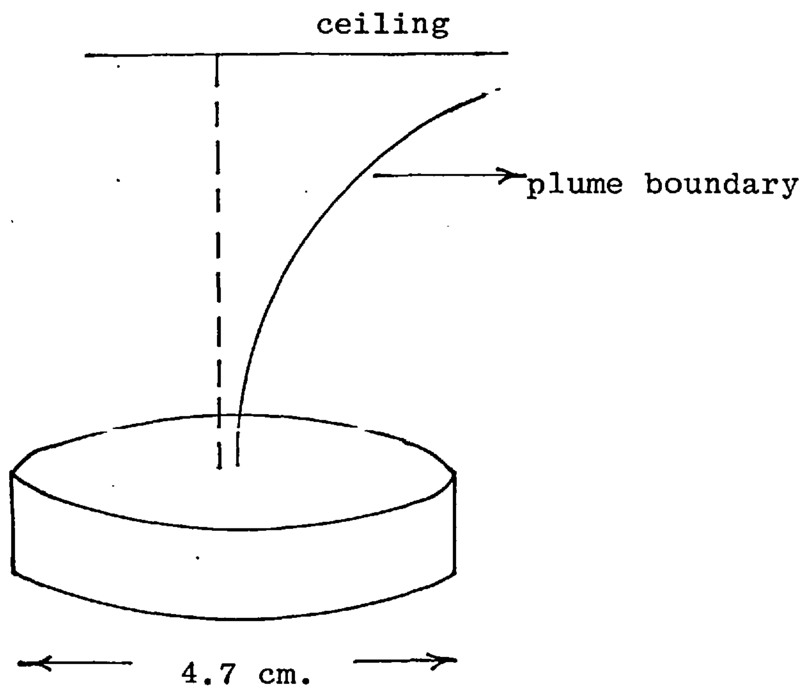

Figure 5.23 Schematic diagram showing the affect of ceiling on fire plume

(a)

(b)

Figure 5.24 a&b Triple exporsure shadowgraphs of a fire plume, showing the effect on it of a horizontal ceiling.

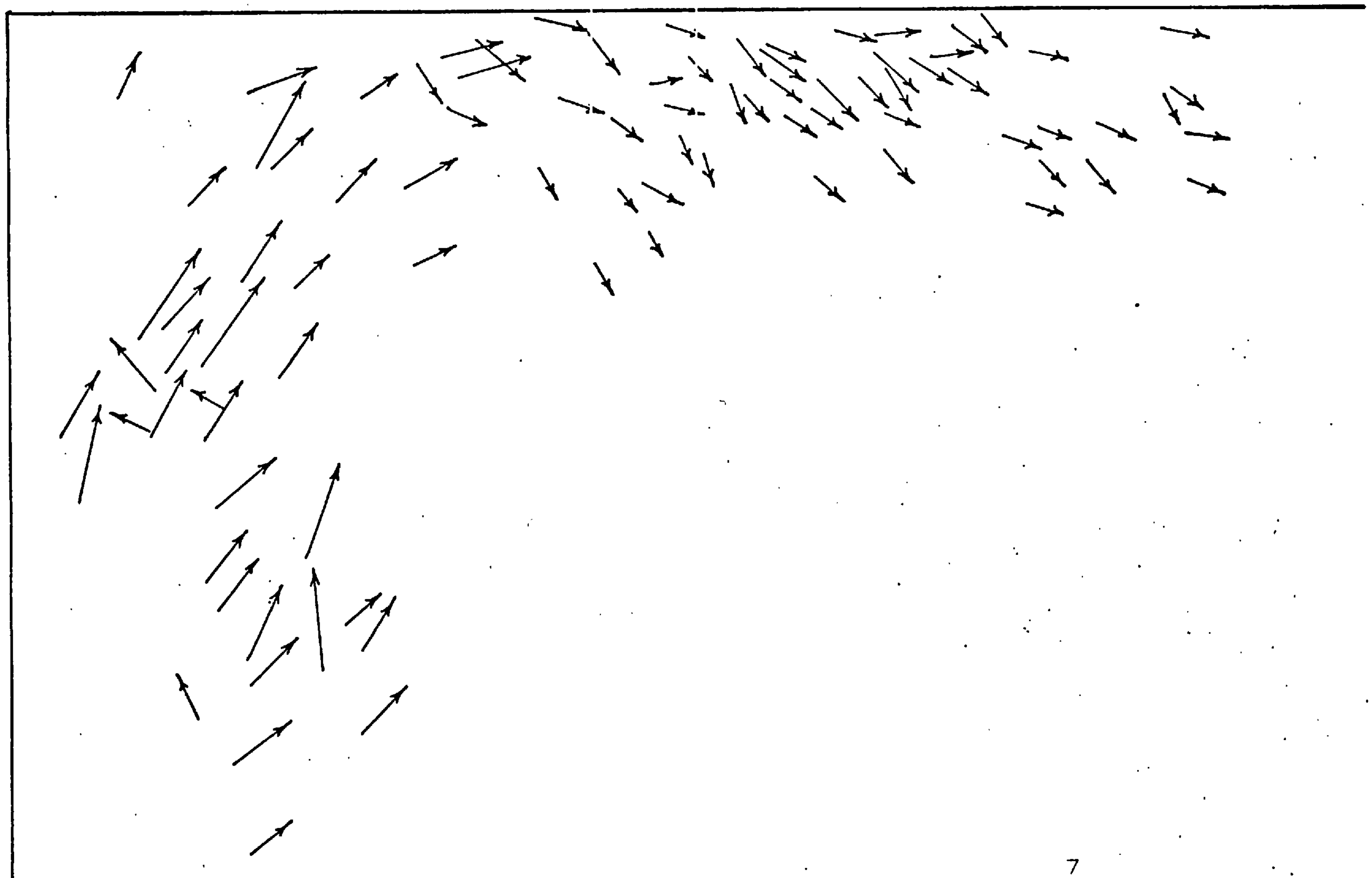

Figure 5.25a Turbule velocity vectors in the presence of the horizontal ceiling

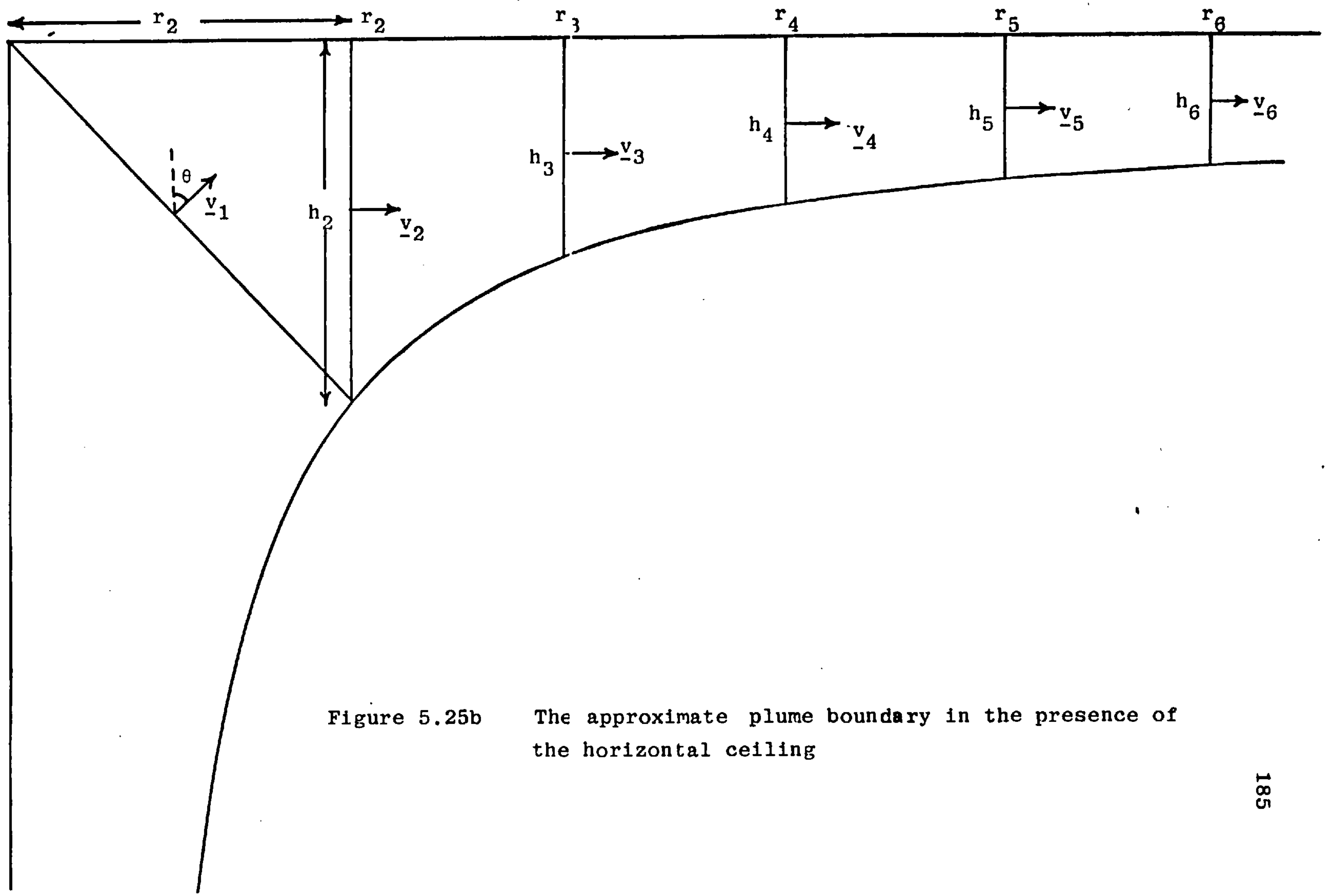

Figure 5.25b The approximate plume boundary in the presence of the horizontal ceiling

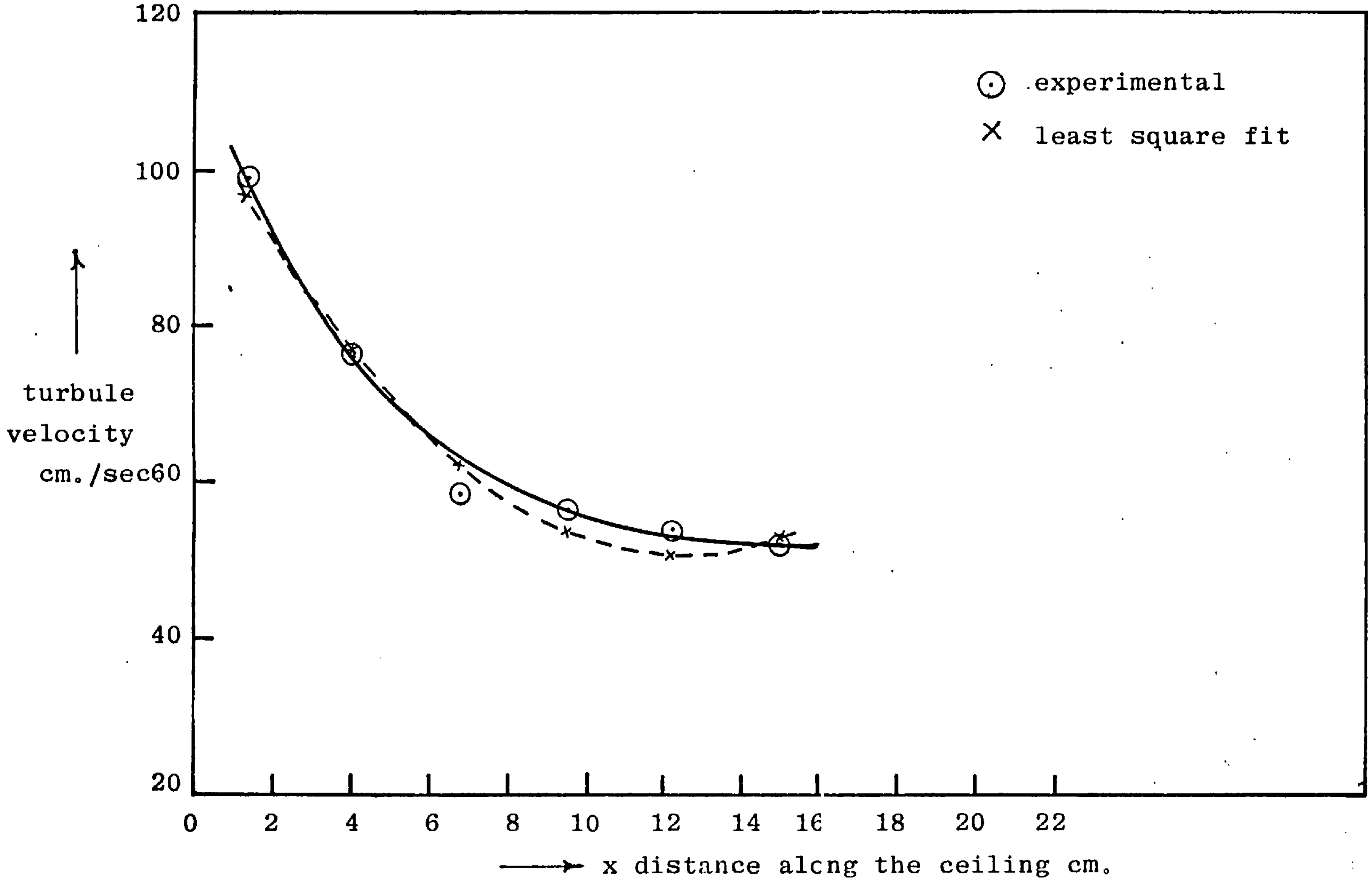

Figure 5.26 Averge resultant velocity distribution horizontally along the ceiling ; the dotted line was obtained from a least square fit

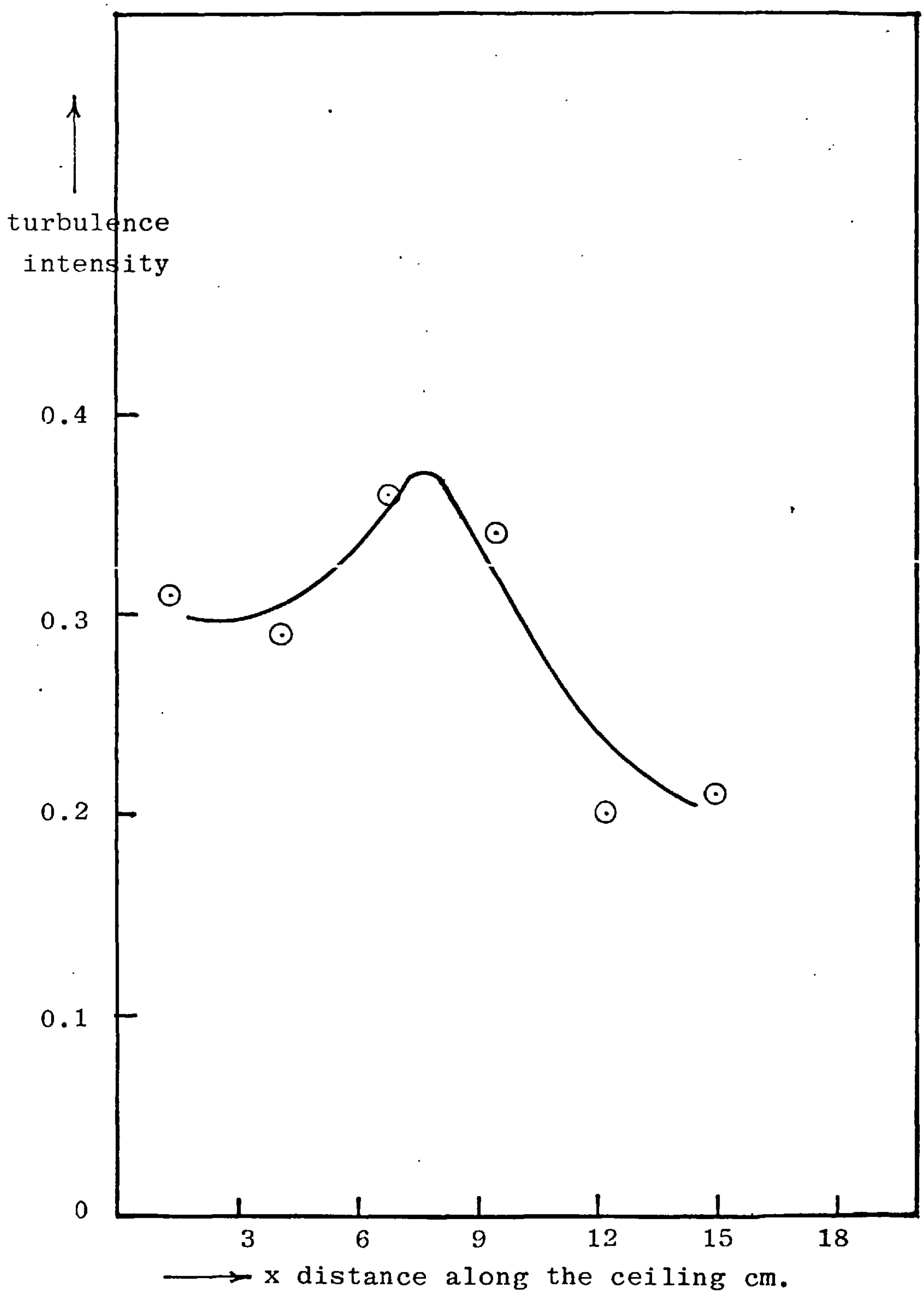

Figure 5.27 Turbulence intensity distribution along a ceiling

distribution along the ceiling can be obtained.
Referring to Figure 5.25b, utilizing the continuity equation, we may write :

$$\pi r_2\sqrt{(r_2^2 + h_2^2)} \times v_1 \times \rho_1 = 2\pi r_i \, v_i \rho_i \qquad 5.5.2$$

where in this case i ranges from 2 to 6

or

$$\rho_i = \{2h_2/\sqrt{(r_2^2 + h_2^2)}\} \, (v_2/v_1) \, \rho_2$$

$$5.5.3$$

$$\rho_i = \{3/(2i-1)\} \, (h_2 v_2/h_i v_i) \, \rho_2$$

where i goes from 3 to 6.

Strictly, one should consider individual stream tube; however, using large blocks and assuming the mixing of two perfect gases each under initially isothermal conditions and constant composition, the use of equations 5.5.2 and 5.5.3 is sufficient to indicate the trend of temperature variation along the ceiling. That is, under these assumptions, we have:

$$\text{Temperature} \propto \frac{1}{\rho} \qquad 5.5.4$$

Therefore,

$$\rho_{i+1}/\rho_i = T_i/T_{i+1} \qquad 5.5.5$$

The temperature distribution so obtained is shown in Figure 5.28 and the line of best fit using the least square method is :

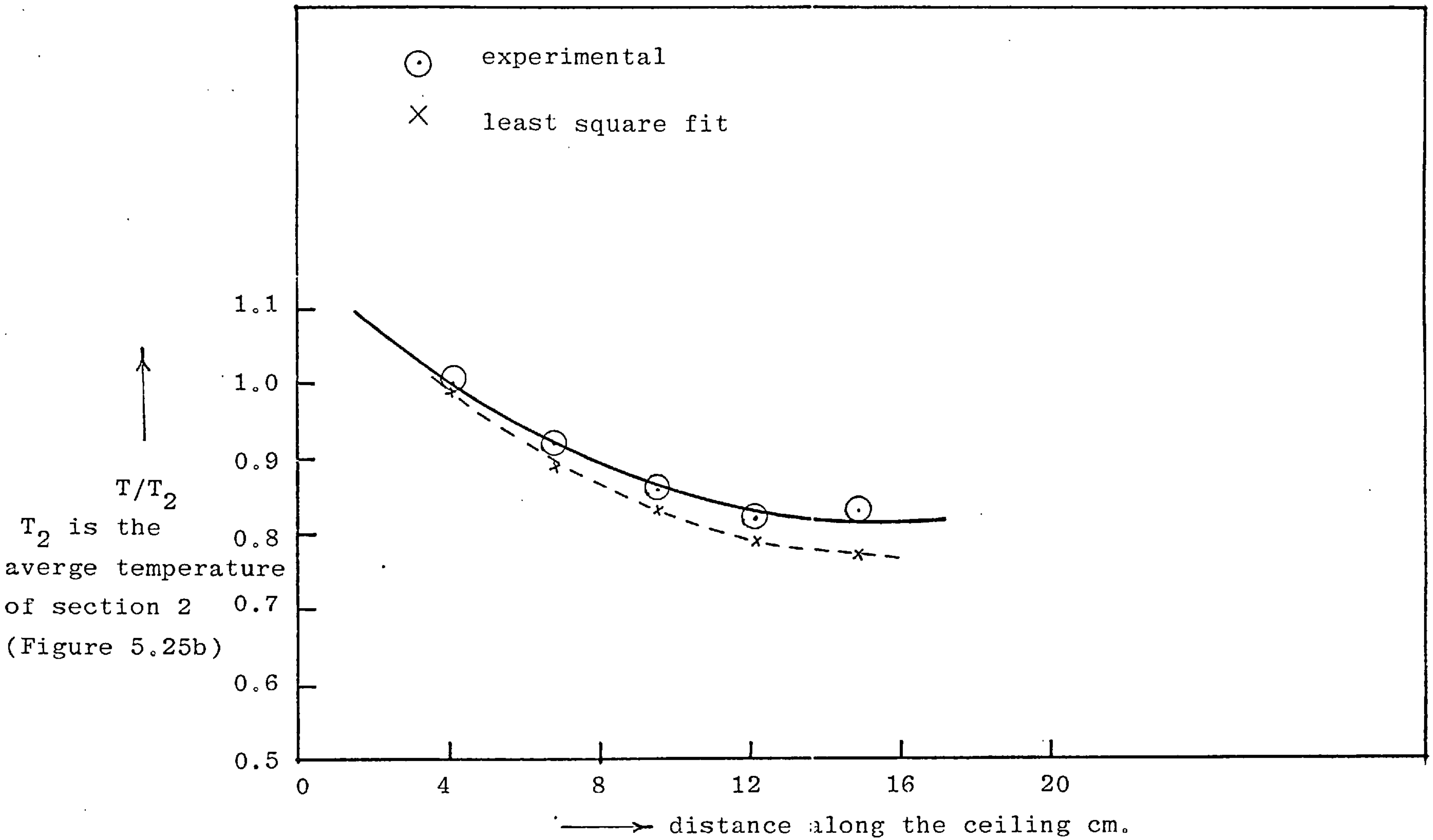

Figure 5.28 Deduced temperature distribution along the ceiling;the dotted line was obtained from a least square fit

$$T/T_2 = 1.16 - 0.05x + 0.0016x^2 \qquad 5.5.6$$

It is evident from the velocity vectors, that the velocity component in the x direction relative to the z component increases with distance along the ceiling. To investigate this matter further, a graph of v_x/v_z against x is plotted in Figure 5.29. The 'error bars' here denote the standard deviations of the fluctuations in v_x/v_z values. The equation of the dashed line is given by:

$$v_x/v_z = 0.11x + 0.97 \qquad 5.5.7$$

5.6 Conclusions

A technique which enables the measurements of plume width and visible flame height by averaging over several hundred readings was developed and results presented. The rate of increase of plume width with height was shown to be greater as the pool diameter becomes larger. Statistical distributions of flame heights for liquid pool burners were established and mean visible flame heights were ascribed for any particular pool burner.

Complete turbule velocity distributions for plumes resulting from pool fires of various sizes were presented. For weakly buoyant regions of the plumes, the experimental results as expressed in equation 5.4a.1 agree with equation 5.2a.24 formulated theoretically and verified experimentally using different techniques. Therefore, in addition to that already discussed in section 4.7, it is

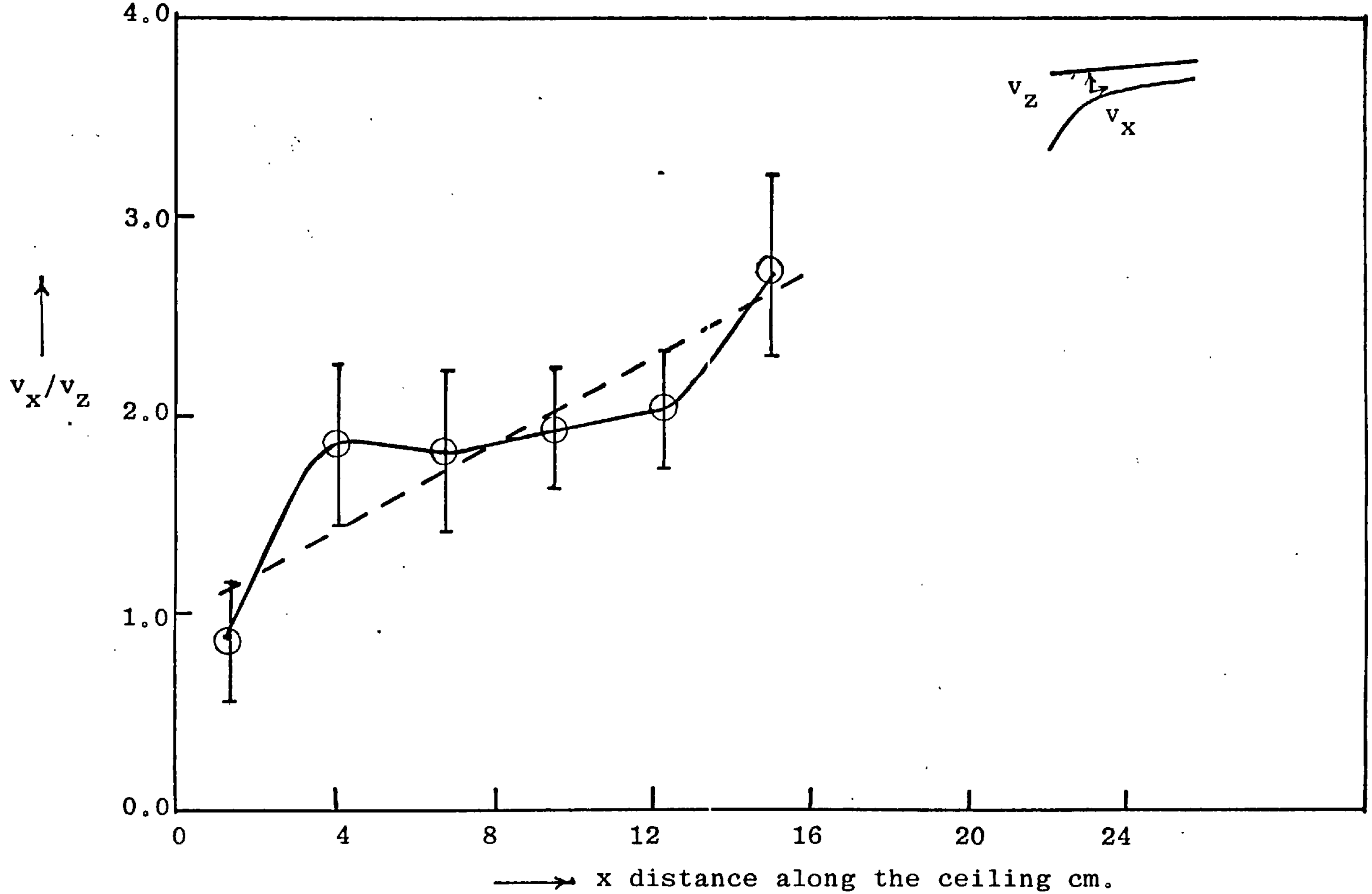

Figure 5.29 Plot of v_x/v_z versus distance along the ceiling

concluded that the present technique is a useful diagnostic tool for exploring the physical characteristics of fire plumes, including those of much larger dimension than could be accommodated in the laboratory.

Extrapolation to the study of non-fire generated plumes, even perhaps, the rising plumes from cooling towers at inland nuclear power generation stations (provided a large enough screen is available). This is important because its behaviour will effect both its effectiveness and acceptance by the local populance.

The original objective of measuring the characteristic frequencies of a laser fire detector is, of course just a 'by-product' of this investigation. It is further expected that this technique will be utilized in the next phase of the research to explore these phenomena in more detail and at greater heights.

From the distributions of $\bar{\eta}$ and the calculated values of $\sigma_{\bar{\eta}}$. The optimum operating frequency range of laser fire detectors was found to be between 95 and 135 Hz..

A great deal of theoretical work still needs to be done before we can finially comprehend fully the complex behaviour of turbulent fire plumes. The conditions at the base of the convective column, the thermal radiation emitted by the column, the change in chemical species due to prolysis and for large open plumes even the atmospheric lapse rate (slope of the atmosphere temperature versus altitude curve), all have to be integrated into the complex fluid dynamic equations. The experimental results on turbulence intensities as presented above are obviously very intricate and their understanding awaits further theoretical research. However, in addition to the establishment of versatile techniques, it is hoped that these results will provide some guidance towards that goal.

APPENDIX

Figure A1 shows the base of a buoyant flame with a differential element over which the mass, momentum and energy balances are written.

Conservation of mass :

Referring to Figure A2, the mass out flow from the differential element must be that of inflow plus that entrained from outside the plume.

Thus;

$$d/dz\ (\pi \rho b^2 u)\ dz = -\rho_\infty\ 2\pi b v\ dz \qquad \text{A.1}$$

or

$$d/dz\ (\rho u b^2) = 2\alpha \rho_\infty u b \qquad \text{A.2}$$

Momentum conservation :

From Figure A3, we may write :

$$d/dz\ (\pi b^2 \rho u^2) = g(\rho_\infty - \rho)\pi\ b^2 \qquad \text{A.3}$$

or

$$d/dz\ (\rho b^2 u^2) = g(\rho_\infty - \rho)\ b^2 \qquad \text{A.4}$$

Energy conservation :

With reference to Figure A4, for energy conservation, we have :

$$d\dot{Q}_1/dz = \dot{Q} \qquad \text{A.5}$$

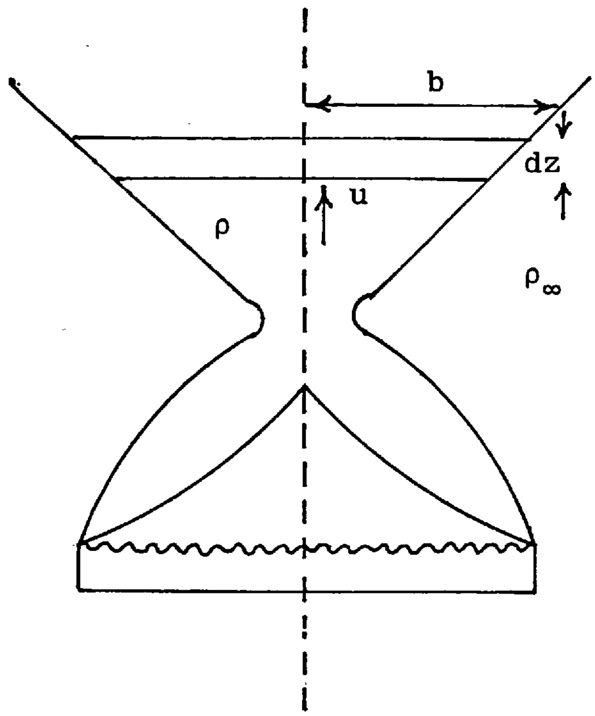

Figure A1 Defining variables in buoyant fire plume

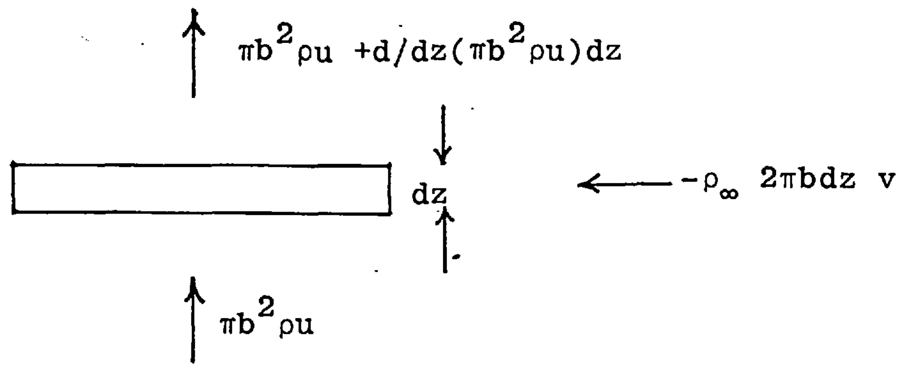

Figure A2

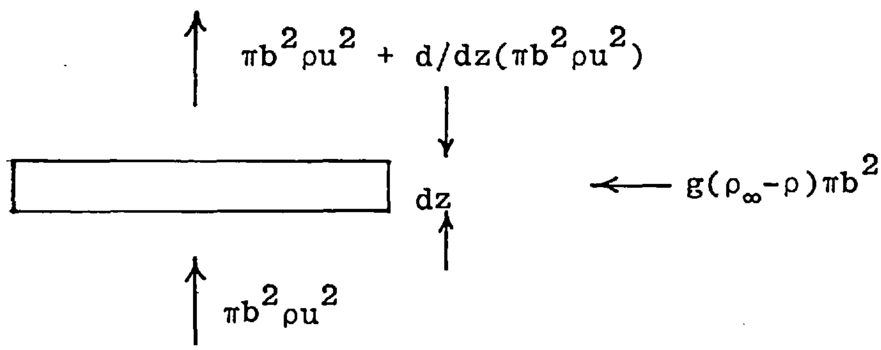

Figure A3

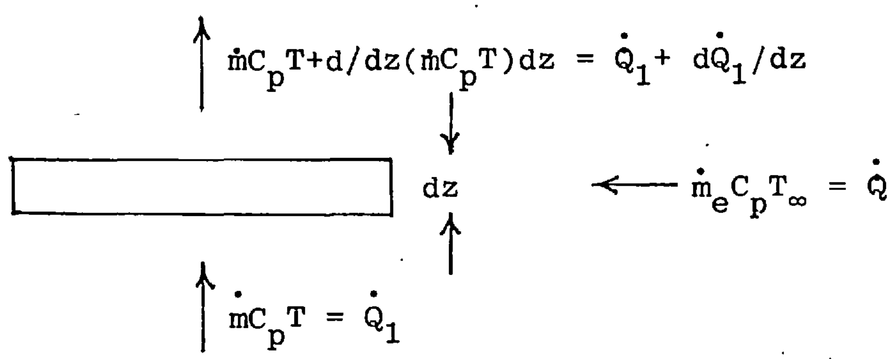

Figure A4

i.e.

$$d/dz\ (\rho u \pi b^2 C_p T)\ dz = -\rho_\infty v 2\pi b dz C_p T_\infty \qquad A.6$$

or .

$$d/dz\ (\rho u b^2 T) = 2\alpha \rho_\infty u b T_\infty \qquad A.7$$

but

$$\rho\ T = \rho_\infty\ T_\infty \qquad A.8$$

Therefore,

$$d/dz\ (ub^2) = 2\alpha ub \qquad A.9$$

It is noted that the Boussinesq approximation (section 5.2a) is not used in the derivation of these conservation equations. Differentiating equation A.2, we obtain:

$$\rho\ d/dz\ (ub^2) + ub^2\ \ d\rho/dz = 2\alpha\rho_\infty ub$$

$$-2\alpha\rho ub + ub^2\ \ d\rho/dz = 2\alpha\rho_\infty ub$$

$$ub^2\ \ d\rho/dz = 2\alpha(\rho_\infty - \rho)\ ub$$

Therefore :

$$d\rho\ /dz = \{\ 2\alpha(\rho_\infty - \rho)\}\ /\ b \qquad A.10$$

Integrating this equation between 0 and z, we have :

$$-\ \ln\ (\rho_\infty - \rho)\ \Big|_0^z = 2\alpha \int_0^z dz/b$$

or

$$(\rho_\infty - \rho_0)/(\rho_\infty - \rho) = 2\alpha \int_0^z dz/b \qquad A.11$$

But equation A.9 may be written :

$$d/dz\ (ub^2) = 2\alpha ub^2/b \qquad \text{A.12}$$

After integrating equation A.12 between the limit of 0 and z, we get

$$\ln ub^2 \Big|_0^z = 2\alpha \int_0^z dz/b$$

or

$$ub^2/u_0b_0^2 = 2\alpha \int_0^z dz/b \qquad \text{A.13}$$

Combining equations A.11 and A.13, it is clear that :

$$\{ (\rho_\omega-\rho)/\rho_\omega \} ub^2 = \text{constant}$$

or

$$\tau' \ ub^2 = \text{constant} = K' \qquad \text{A.14}$$

where $\tau' = (\rho_\infty-\rho)/\rho_\infty$ A.15

For regions of the plume where $\tau' \simeq 1$ (i.e. $T_\infty << T$) then equation A.14 implies that :

$$u \propto 1/b^2 \qquad \text{A.16}$$

Substituting equation A.14 into equation A.4 yields :

$$(1/\rho_\infty)\ d/dz\ (\rho u^2 b^2) = g\tau' b^2$$

But since :

$$\rho\ /\rho_\infty = 1 - \tau'$$

we have :

$$d/dz\ \{\ u(ub^2 - K')\} = gK'/u \qquad \text{A.17}$$

Let $ub^2 = \gamma$, then we have from equation A.9 :

$$d\gamma\ /dz = 2\alpha\gamma\ /b = 2\alpha\sqrt{(\gamma u)} \qquad \text{A.18}$$

and from equation A.17 :

$$d/dz\{\ u(\gamma - K')\ \} = gK'/u \qquad \text{A.19}$$

Now we note that :

$$K' = \tau' ub^2 = (\rho_\infty - \rho)\ (ub^2)/\rho_\infty = \{\ (1 - \rho/\rho_\infty)\ \}\ \gamma$$

or

$$\gamma\ = K'/\{\ 1 - (\rho/\rho_\infty)\}$$

In practice, for strongly buoyant regions of the fire plume, $T_\infty \simeq 300$ K and $T \gtrsim 1000$ K (say).

Therefore : $\rho\ /\rho_\infty \lesssim\ 1/3$

Thus allow :

$$\gamma \simeq K'\{ 1 + (\rho / \rho_\infty)\}$$

(i.e. $1/(2/3) = 1\frac{1}{2} \simeq 1\frac{1}{3}$; error is (1.5-1.33)/1.5 = 0.17 /1.5 ≃ 10%)

Then let :

$$\gamma = K' + \gamma_1$$

where γ_1 is small, equations A.18 and A.19 become :

$$d \gamma_1/dz \simeq 2\alpha\sqrt{(K'u)} \qquad \text{A.20}$$

$$d/dz (u \gamma_1) \simeq gK'/u \qquad \text{A.21}$$

Now eliminate u :

$$(d \gamma_1/dz)^2 = 4\alpha^2K'u$$

therefore , $u = 1/(4\alpha^2K') \quad (d \gamma_1/dz)^2$ A.22

$$du/dz = 1/(4 \alpha^2K') \quad 2(d\gamma_1 /dz) \quad (d^2\gamma_1/dz^2)$$

Equation A.21 is :

$$\gamma_1 du/dz + u d\gamma_1/dz = gK'/u$$

or

$$\gamma_1 \; 2/(4\alpha^2K') \quad (d\gamma_1/dz) d^2\gamma_1/dz^2 + 1/(4\alpha^2K') \quad (d\gamma_1/dz)^3$$

$$= gK' \; 4\alpha^2K'/(d\gamma_1/dz)^2$$

or

$$2\gamma_1 \ (d\gamma_1/dz)^3 \ d^2\gamma_1/dz^2 + (d\gamma_1/dz)^5$$

$$= 16\alpha^4 K'^3 g \qquad \text{A.22}$$

write:

$$d\gamma_1/dz = P \ ; \ d^2\gamma_1/dz^2 = dP/dz = P \ (dP/d\gamma_1)$$

Then :

$$2\gamma_1 P^4 \ (dP/d\gamma_1) + P^5 = 16\alpha^4 K'^3 g$$

or

$$(2/5) \ \gamma_1 \ (dP^5/d\gamma_1) = - \ (P^5 - 16\alpha^4 K'^3 g)$$

and

$$dP^5/(P^5 - 16\alpha^4 K'^3 g) = -(5/2) \ (d\gamma_1/\gamma_1)$$

or on integration :

$$\ln \ (P^5 - 16\alpha^4 K'^3 g) = -(5/2) \ \ln\gamma_1 + \text{constant}$$

Therefore :

$$P^5 - 16\alpha^4 K'^3 g = \text{constant X} \ (1/\gamma_1)^{5/2}$$

But

$$P = d\gamma_1/dz = 2\alpha\surd \ (K'u)$$

$$P^5 = 32\alpha^5 \ (K'u)^{5/2}$$

Therefore :

$$32\alpha^5 \ (K'u)^{5/2} - 16\alpha^4 K'^3 g = \text{constant X} \ (1/\gamma_1)^{5/2}$$

or

$$32\alpha^5 (K'u)^{5/2} \ \{1 - (16\alpha^4 K'^3 g)/(32\alpha^5 (K'u)^{5/2})\}$$

$$= \text{constant X} \ (1/\gamma_1)^{5/2}$$

$$2\alpha\ (K'u)^{\frac{1}{2}}\ \{\ 1-(g/2\alpha)\surd\ (K'/u^5)\}^{\ 1/5} = \text{constant X}\ (1/\gamma_1)^{\frac{1}{2}}$$

$$4\alpha^2\ K'u\{\ 1-(g/2\alpha)\surd(K'/u^5)\}^{\ 2/5} = \text{constant}\ /\ \gamma_1$$

Therefore :

$$\gamma_1 = C_1\ /\ \{\ 4\alpha^2 K'u(1-(g/2\alpha)\ \surd\ (K'/u^5))^{2/5}\} \qquad A.23$$

and

$$\gamma = K' + C_1\ /\{4\alpha^2 K'u(1-(g/2\alpha)\ \surd(K'/u^5))^{2/5}\} \qquad A.24$$

So that :

$$u = 1/b^2\{\ K' + C_1/\ \{4\alpha^2 K'u(1-(g/2\alpha)\ \surd(K'/u^5))^{2/5}\ \}\} \qquad A.25$$

As a first approximation, one may replace u on the RHS of equation A.25 by $u = K'/b^2$ (c.f. equation A.16). Then:

$$u \simeq (K'/b^2) + C_1\ /\ \{\ 4\alpha^2 K'^2(1-(gb^5/2\alpha K'^2))^{2/5}\ \} \qquad A.26$$

In order to gain some insight into the magnitude of $gb^5/2\alpha K'$, put :

$g \simeq 10$ m. s^{-1}

$b \simeq 5 \times 10^{-2}$m.

$\alpha \simeq 0.12$

$u \simeq 5 \times 10^{-1}$ m.s^{-1}

Then:

$$K' = \tau' ub^2 \simeq (1-T_\infty\ /T)\ ub^2$$
$$\simeq 2/3\quad 5 \times 10^{-1} \times (5 \times 10^{-2})^2 \simeq 8.3 \times 10^{-4}$$

Therefore :

$$gb^5/2\alpha K'^2 \simeq 20$$

Thus :

$$gb^2/2\alpha K'^2 >> 1$$

Therefore :

$$u \simeq (K'/b^2) + C_1 \;/\; \{ 4\alpha^2 K'^2 (1+(gb^5/2\alpha K'^2))^{2/5} \}$$

$$= (K'/b^2) + C_1/ \; \{4\alpha^2 K'^2 (g/2\alpha K'^2)^{2/5} b^2 (1+(2\alpha K'^2/gb^5))^{\frac{2}{5}}$$

$$= (K'/b^2) + \frac{C_1(1-(4\alpha K'^2/5gb^5))}{4\alpha^2 K'^2 (g/2\alpha K'^2)^{2/5}\; b^2}$$

or

$$u = (C_2/b^2)-(C_3/b^7) \qquad \text{A.27}$$

Where :

$$C_2 = K' + \frac{C_1}{4\alpha^2 K'^2 (g/2\alpha K'^2)^{2/5}} \qquad \text{A.28}$$

and

$$C_3 = \frac{C_1 \; 4\alpha K'^2}{5g} \text{X} \; \frac{1}{4\alpha^2 K'^2 (g/2\alpha K'^2)^{2/5}}$$

$$= C_1 \;/\; \{ \; 5g\alpha (g/2\alpha K'^2)^{2/5} \; \} \qquad \text{A.29}$$

From equation A.27 :

$$d(ub^2)/dz = d/dz\ (C_2-(C_3/b^5))$$

$$= -\ C_3\ d/dz\ (1/b^5) \simeq 2\alpha C_2/b$$

$$d/dz(b^{-5}) = -5b^{-6}db/dz$$

$$(5C_3/b^6)\ db/dz = 2\alpha C_2/b$$

Therefore :

$$(5/b^5)\ db/dz = 2\alpha C_2/C_3 \qquad \text{A.30}$$

Integrating, we have :

$$5b^{-4}/-4 = 2\alpha C_2 z/C_3 + \text{constant}$$

$$1/b^4 = \text{constant} - (8\alpha C_2 z/5C_3)$$

$$1/b^4 = C_4 - C_5 z$$

$$b^4 = 1\ /\ (C_4 - C_5 z)$$

Therefore :

$$b \simeq \{1\ /\ (C_4-C_5 z)\}^{\frac{1}{4}}$$

where C_4 is the integration constant on integrating equation A.30 and $C_5 = 8\alpha C_2/5C_3$.

At z=0, b=b0, $bo \simeq (1/C_4)^{\frac{1}{4}}$

and $$b \simeq b0/\ \{\ 1-(C_5 z/C_4)\ \}^{\frac{1}{4}} = b0/(1-b_0^4 C_5 z)^{\frac{1}{4}} \qquad \text{A.31}$$

To calculate C_1, write equation A.26 as :

$$u_0 = (K'/b_0^2) + (C_1/f(b_0))$$

$$C_1 = f(b_0)\ \{ u_0-(K'/b_0^2)\}$$

$$u \simeq (K'/b^2) + \frac{f(b_0)\{ U_0-(K'/b_0^2)\}}{f(b)}$$

$$u = u_0\ f(b_0)/f(b) + (K'/b^2)\ \{ 1- (f(b_0)/f(b)) \}$$

Therefore :

$$C_1 \simeq 4\alpha^2K'^2\{ 1 + (gb_0^5/2\alpha K'^2)\}^{2/5} \{ u_0-(K'/b_0^2)\}$$

$$= 4\alpha^2K'^2\ (g/2\alpha K'^2)^{2/5}\ b_0^2\ \{ u_0-(K'/b_0^2)\} \qquad \text{A.32}$$

We have now obtained approximate solutions for strongly buoyant regions of fire plumes. For weakly buoyant regions, where the Boussinesq approximation is applicable, however, the matter is very much simpler. In this case, $\tau' \simeq \tau$ and τub^2 = constant as in equation 5.2a.16. Also equations A.2 and A.4 may then be written:

$$d/dz\ (ub^2) = 2\alpha ub$$

and $d/dz\ (u^2b^2) = g(\rho_\infty-\rho)b^2/\rho$

respectively. Thus, in this instance, the solutions as given in equations 5.2a.24 and 5.2a.25 are appropriate.

LIST OF SYMBOLES

Chapter 2

I	intensity
subscripts: o,sca,abs, ext,trans	represent incident, scattering, absorption, extinction and transmission respectively
(r,θ,ϕ)	spherical coordinates
$F(\theta,\phi)$	dimensionless scattering function
P	power
C	cross-section
x	particle size parameter
a	particle radius
λ	wave length
A	cross-sectional area
Q	efficiency factor
E	extinction
K	coefficient
L	path length
α_λ	monochromatic absorptivity
ε_λ	monochromatic emissivity
N	particle density
V	volume
m	refractive index
$Im(X)$	imaginary part of X
e	eccentricity
$P(X)$	normalized distribution function of X
$f(X)$	function of X
$\bar{X}$	mean value of X
$\underline{X}$	vector X
a_x and a_y	amplitudes in the x and y directions respectively
k	$2\pi/\lambda$
δ	phase angle

I,M,C,S	Stokes' parameters corresponding to the incident beam
I',M',C',S'	Stokes' parameters corresponding to the emergent beam
subscripts:h,v	represent incident light linearly polarized in horizontal and vertical directions respectively
(x,y,z)	Cartesian coordinates
subscripts: corr., rec, ref	represent correct recorded and reference respectively
P=0	represent original state of polarization
P=90	represent state of polarization when the half wave plate is rotated through $\pi/2$ from P=0
r	polarization ratio

Chapter 3

ξ	distance between phase object and screen
n	refractive index
$\Delta\phi$	phase difference
$(\phi_m-\phi_r)$	represents the phase difference due to passage of the beams through regions of differing refractive index
subscripts:p,r	represent that of phase object and reference medium respectively
subcripts:s,g	represent shear and glass respectively
s	shear at beam splitter
s_t	shear at test space
q	fringe spacing
η	distance between the principal point reflection and the screen
f	inter-fringe spacing between two successive Moire fringes
δ	n-1
T	temperature
subscript:0	represents value at N.T.P.

Chapter 4

v	velocity
$\underline{v}$	vector v
c	velocity of light
$\hat{\underline{k}}$	unit vector
subsctipts:i,0	represent incident and observation respectively
λ	wave length
ν	frequency
subscript:a	represents apparent
ν_b	beat frequency
$< v >$	mean value of v
v'	instantaneous deviation of v from <v>
d	slit separation
A	amplitude
ϕ	phase angle
t	time
subscript:f	represents fringe
(r,θ)	polar coordinates
M	magnification
$\underline{r}$	position vector
$P(\underline{r})$	point at the position vector specified by $\underline{r}$
I	intensity
$V(\underline{r},\underline{t})$	complex disturbance at position $\underline{r}$ and time t
K	propagator
$\Gamma_{12}(\tau)$	mutual coherence function
superscript:r	represents real
$\gamma_{12}(\tau)$	complex degree of coherence
$\bar{\nu}$	mean frequency
$\mathcal{V}$	visibility
p	order of interference

θ	angle of deflection
f	focal length
d	distance between selective aperture in schlieren blind
s	linera dimension of selective aperture
n	number of diffraction orders
N	number of observed beats in Doppler beat frequency signal
ω_m	minimum beam width
P	pressure
q	fringe spacing
V	velocity of front
a	diameter of detector aperture
J_1	Bessel function of the first kind of order one
I_N	noise level of photomultiplier
a_o, a_{+1}, a_{-1}	amplitudes of diffraction orders o,+1 and -1 respectively
$\delta_o, \delta_{+1}, \delta_{-1}$	phase angles of diffraction orders o,+1 and -1 respectively
t_e	exposure interval
ω	angular velocity
r	radius of the sectored disc
V_t	turbule velocity
d	distance between turbules

Chapter 5

v	entrainment velocity
α	air entrainment coefficient
u	vertical plume velocity
b	plume width
H	enthalpy of mixture
C_p	specific heat at constant pressure
T	temperature

$\langle u \rangle$	time-mean velocity
ρ	density of gas in plume
ρ_∞	density of air outside plume
Q_r	radiation loss per unit volume
g	gravitational constant
σ	Boltzmann's constant
ε	emissivity of plume
d	pool diameter
h	visible flame height
v_z and AV_z	average vertical component of turbule velocity
v_x and AV_x	average horizontal component of turbule velocity
TIVX	turbulence intensity as calculated from experimental values of AV_x
TIVZ	turbulence intensity as calculated from experimental values of AV_z
$\bar{L}$	average distance between turbule shadows on record
$\bar{l}$	mean characteristic scale of turbules
$\bar{\eta}$	mean laser flicker frequency
$\sigma_{\bar{\eta}}$	standard deviation of $\bar{\eta}$
AV_R	average resultant turbule velocity
m	mass
Q	heat
b_o	plume width at $z=o$

REFERENCES

1. Lawson D.I. 1971 JFRO Reports No.673 and 824
2. Report of the directors 1971 Fire Research P.62
3. Burry P.E. 1974 Fire Surveyor Vol.3 No.5 P.43
4. Fry J.F. and Eveleigh C. 1970 JFRO Research Note 810
5. Weinberg F.J. Progress in Combustion and Technology (Ducarme J.et.al.,Ed.) 1960,1,P.113
6. Lewis B. and Von Elbe G. Combustion Flames and Explosion of Gases 1961,(Academic Press) Chapter 10
7. Fristrom R.M. and Westenberg A.A. Flame Structure, 1965 (McGraw-Hill) Chapter 11
8. Dalzell W.H. Williams G.C. and Hottel H.C. Combust.Flame 1970,14, P.161
9. Jones A.R. Combustion Institute European Sympsium (F.J.Weinberg,Ed.), Academic Press London 1973,P.376
10. Cerf R. and Scheraga H.A., Chem. Rev. 1952,51,P.185
11. Kerker M. The Scattering of Light 1969,Academic Press New York, Chap.10
12. Jones A.R. and Schwar M.J.R. High Temperature-High Pressure, 1969, Vol.1, P.373
13. Mie G. Ann.d.Physik, 1908 (4),25,P.377
14. Medalia A.I. and Heckman F.A.,Carbon,1969,7,P.567
15. Born M. and Wolf E.,Principles of Optics, Pergrmon Press, 1970,Chapter 10
16. Lord Rayleigh, Theory of Sound, Vol.1,1877,P.93
17. Krishnan R.S. Proc.Ind.Acad.Sci.,(A),1938,P.21
18. Krishnan R.S. Proc.Ind.Acad.Sci.,(A),1938,P.91
19. Creeden J.E.,Fristrom R.M., Grunfelder C.and Weinberg F.J. J.Phys.D:Appl.Phys.,1972,Vol.5,P.1063

20. Jones A.R. Schwar M.J.R. and Weinberg F.J. Proc.Roy.Soc.Lond.,1971, A,322,P.119

21. Weinberg F.J., Optics of Flames,1963(London: Butterworth)

22. Schwar M.J.R. and Weinberg F.J.,Nature,London, 1971,221,P.357

23. Schwar M.J.R. and Weinberg F.J., 1969,Proc.Roy.Soc. Lond.,A,311,P.469

24. Schwar M.J.R. and Weinberg F.J., 1969,Combustion and Flame,13,P.335

25. Linnett J.W.,Fourth Symposium (International) on Combustion,1953,P.20

26. Gaydon A.G. and Wolfhard H.G.,Flames: Their Structure Radiation and Temperature,1970(London:Chapman and Hall)

27. Andrews G.E. and Bradley D.,Combustion and Flames, 1972,18,P.133

28. Dopper C.J.,1842,Böhm Cesell Abh.,2,P.465

29. Fizeau H.C.,1949,Comptes Rendus,Paris,29,P.40

30. Ramsden S.A. and Davies W.E.R., 1964,Phys.Rev.Lett., 13,P.227

31. Tolansky S.,High Resolution Spectroscopy,1947(Methuen London)

32. Schwar M.J.R. and Weinberg F.J.,Combustion and Flame 1969,Vol.13,No.4

33. Yeh Y. and Cummins H.Z.,Appl.Phys. Lett.,1964,4,P.176

34. Foreman F.W.,George E.W. and Lewis R.D., Appl.Phys. Lett.,1965,7,P.77

35. Rudd M.J.,J.Phys.E.,1968,1,P.723

36. Rudd M.J.,J.Phys.E.,1969,2,P.55

37. Goldstein R.J.,Hagen W.F.,Phys.Fluids,1967,10,P.1349

38. Pike E.R.,Jackson D.A.,Bourke P.J. and Page D.I.,J. Phys.E,1968,1,P.727

39. Foreman J.W.,et.al.,I.E.E.E.,J.Quantum Electronics, 1966,QE-8,P.260

40. Bien F. and Penner S.S.,Phys.Fluids,1970,13,P.1665

41. Michelson A.A.,Phil. Mag.,1890,30,P.1

42. Françon M.,Optical Interferometry,1966,Academic Press.

43. Harris M.E.,Grum J.G.,VonElbe G. and Lewis B.,Third Symposium (International) on Combustion,1949,P.80

44. Lee S.L.,J.Appl.Mech.,1966,38,P.656

45. Lee S.L. and Ling C.H.,Eleventh Symposium (International) on Combustion,P.501

46. Yih C.S.,Proc.1st Nat.Congr.Appl.Mech.,P.941

47. Schwar M.J.R.,Pamdyn T.P. and Weinberg F.J.,Nature, Lond.,1967,215,P.239

48. Jagoda I.J.,PhD. Thesis,Imperial College,Lond.,to be submitted in 1976

49. Schmidt W.and Angew A.,Math.Mech.,1941,21,265

50. Rouse H.,Yih C.S. and Humphries H.W.,Tellus,1952, 4,P.201

51. Priestly C.H.B. and Ball F.K.,Quart.J.Roy. Met.Soc., 1955,81,P.144

52. Morton B.R.,Taylor G.I. and Turner J.S.,Proc.Roy.Soc., A,1956,236,P.1

53. Morton B.R.,J.Fluid Mech.,1957,2,P.127

54. Morton B.R.,J.Fluid Mech.,1959,5,P.151

55. Lee S.L. and Emmons H.W.,J.Fluid Mech.,1961,11,P.353

56. Mungai M.P.,J.Fluid Mech.,1962,12,P.441

57. Nielsen H.J. and Tao L.N.,Tenth Symposium (International) on Combustion,P.965

58. Morton B.R.,Tenth Symposium (International) on Combustion,P.973

59. Steward I.R.,Combustion Science & Technology,1970,2,P.263

P82Eq.4.3a.1	change r_2 to: $\underline{r}_2$
P83Fig.4.8	add P on the screen Σ' to denote point of interference
P85L2	change 4.4a.4 to: 4.3a.4
P88L20	change apectures to: apertures
P88L23	change 4.3b.4 to: 4.2b.4
P91L4	change slected to: selected
P96Eq.4.4a.4	change - to: =
P99L17	add after is: ,
P107L5	replace velocities. by: velocities,
P107L6	change Therefore to: therefore
P128L26	change ioside to: inside
P134L8	change diminsions to: dimensions
P134L24	change calculute to: calculate
P139L1	add after Appendix): .
P139L1	change it to: It
P141L21	change is to: are
P143L1	change 4.3b.5 to: 4.2b.5
P143Eq.5.2a.2	change $\frac{1}{r}\frac{\partial}{\partial z}$ to: $\frac{1}{r}\frac{\partial}{\partial r}$
P148Eq.5.2b.1	change $\frac{1}{r}\frac{\partial}{\partial z}$ to: $\frac{1}{r}\frac{\partial}{\partial r}$
P151L8	change centmetres to: centimetres
P153L13	change appear to: appears
P174L11	change trubules to: turbules
P174L19	change intergrates to: integrates
P183Fig.5.24	change exporsure to: exposure
P192L7	add after stations: is perhaps possible
P207Chap.3	add symbol x to denote ray direction
P208L5	change subsctipts to: subscripts
P208Chap.4	add A* to denote the complex conjugate of A
P211Ref.15	change Pergrmon to: Pergamon
P213Ref.45	insert after Combustion,: 1967,
P213Ref.46	insert after Mech.,: 1951,
P213Ref.57	insert after Combustion,: 1965,
P213Ref.58	insert after Combustion,: 1965,
P214Ref.63	change Rasash to: Rasbash
P214Ref.66	change Ricou & Spalding to: Ricou F.P. and Spalding D.B.
P214Ref.67	insert after Combustion,: 1963,
P214Ref.68	insert after Combustion,: 1965,
P214Ref.71	insert after Combustion,: 1953,
P214Ref.72	insert after Combustion,: 1965,
P214Ref.76	change Figteenth to: Fifteenth
P214Ref.76	insert after Combustion,: 1975,

Abbreviations

P	Page
L	Line
ABS.	ABSTRACT
ACK.	ACKNOWLEDGEMENTS
Eq.	Equation
Fig.	Figure
Chap.	Chapter
Ref.	Reference

60. Fay J.A.,Annual Review of Fluid Mech.,1973,P.5

61. Byam G.M. and Nelson J.R.,Fire Technology,1974,10,P.68

62. Escudier M.P., Combustion Science & Technology,1975, 10,P.163

63. Rasash D.J.,Rogowske,Z.W. and Stark G.W.V.,Fuel, 1956,35,P.94

64. Boussinesq J.,Thèorie Analytique de la Chaleur,1903, 2,P.9

65. Mungai M.P. and Emmons H.W., J.Fluid Mech.,1960,12,P.441

66. Ricou & Spalding,J.Fluid Mech.,1961,28,P.311

67. Thomas P.H., Ninth Symposium (International) on Combustion,P.844

68. Baldwin R. and Heselder A.J.M.,Tenth Symposium (International) on Combustion,P.983

69. Burgogne J.H. and Katan L.L., J.Inst.Petrol,1947,33,P.158

70. Khydyakov G.N.,Bull.Acad.Sci.U.S.S.R.,1945,No.10-11, P.1115

71. Spalding D.B., Fourth Symposium (International) on Combustion,P.847

72. Akita K.and Yumoto T.,Tenth Symposium (International) on Combustion,P.943

73. Corlett R.,Heat Transfer in Fire,Blackshear P.C.,Ed., 1974,(John Wiley & Sons)

74. Atallah S.,Combustion and Flame,1965,9,P.203

75. Torrance K.E. and Rocket J.A.,J Fluid Mech.,1969,36,P.33

76. Adams J.S.,Williams D.W. and Williams J.T.,Figteenth Symposium (International) on Combustion,P.1045

CORRIGENDA to thesis AN OPTICAL STUDY OF TURBULENCE WITHIN FIRE PLUMES by W. W. Y. Wong, 1976

ABS.L8	change ib to: in
ACK.L11	Change maniscript to: manuscript
P3L20	change stationery to: stationary
P9Eq.2.2a.5	change Pinc to: P_o
P9Eq.2.2a.6	change Pinc to: P_o
P9L18	change 2.2.a7 to: 2.2a.7
P9Eq.2.2a.7	change Ke to Kext
P10L8	change spherial to: spherical
P10L14	change corss to: cross
P12L9	change ln(R-1) to: $\ln(\bar{R}-1)$
P12L9	change lnE to: $\ln E'$
P12L10	change E to: E'
P12L11	change E to: E'
P12L12	change R-1 to: $\bar{R}-1$
P13Fig.2.1	change ln(R-1) to: $\ln(\bar{R}-1)$
P13Fig.2.1	change lnE to: $\ln E'$
P15L13	delete after beam: .
P15L13	add after beam: are affected.
P16Eq.2.3a.5	insert after the first column matrix: =
P19L4	insert after hence: there is
P19Eq.2.3d.1	change Pinc to: P_o
P24L12	insert after minimum: intensity
P33L3	change bence to: hence
P34L15	replace Increase by: An increase in
P34L18	change anlargement to: enlargement
P35L7	delete after object): .
P35L7	add after object): or by using a double exposure/single grating technique.
P36L10	change Considere to: Consider
P38L16	delete after shear: is
P41L9	change discribed to: described
P41L17	change determines to: determined
P42Fig.3.3	change front to: fronts
P43L20	change ooptical to: optical
P43L24	change an to: a
P45L1	change intergration to: integration
P50L7	change obtined to: obtained
P50L26	change leight to: light
P65L20	change velicities to: velocities
P65L21	change . to: ,
P65L22	change A to: a
P70L18	change systerm to: system
P71Fig.4.3	change Goldostein to: Goldstein
P73Fig.4.3	replace PRSA by: Proc. Roy. Soc. Lond.,A,311,
P75L11	change , to: .
P75L12	change however to: However
P77L12	change apectures to: apertures
P77Eq.4.2c.3	add after $(\varnothing_1 - \varnothing_2)$: $\}$
P77L17	replace , however by: . However
P80Eq.4.2c.11	delete: =0
P82L19	change schleren to: schlieren